

W-doped indium oxide synthesized via hydrothermal route for low temperature ozone sensing

Original

W-doped indium oxide synthesized via hydrothermal route for low temperature ozone sensing / Ziegler, Daniele; Palmero, Paola; Tulliani, JEAN MARC CHRISTIAN. - In: SOLID STATE IONICS. - ISSN 0167-2738. - ELETTRONICO. - 347:115271(2020). [10.1016/j.ssi.2020.115271]

Availability:

This version is available at: 11583/2839732 since: 2020-07-13T22:55:54Z

Publisher:

Elsevier

Published

DOI:10.1016/j.ssi.2020.115271

Terms of use:

This article is made available under terms and conditions as specified in the corresponding bibliographic description in the repository

Publisher copyright

Elsevier postprint/Author's Accepted Manuscript

© 2020. This manuscript version is made available under the CC-BY-NC-ND 4.0 license
<http://creativecommons.org/licenses/by-nc-nd/4.0/>. The final authenticated version is available online at:
<http://dx.doi.org/10.1016/j.ssi.2020.115271>

(Article begins on next page)

W-doped indium oxide synthesized via hydrothermal route for low-temperature ozone sensing

Daniele Ziegler¹, Paola Palmero¹, Jean-Marc Tulliani^{1*}

¹Politecnico di Torino, Department of Applied Science and Technology, INSTM R.U
PoliTO-LINCE Laboratory, Corso Duca degli Abruzzi, 24, 10129 Torino, Italy

*Corresponding author: Tel: +39-011-0904700; E-mail address: jeanmarc.tulliani@polito.it

Abstract

Nano-crystalline indium oxide and tungsten-doped indium oxide were prepared by hydrothermal route and adopted as ozone sensitive material at low temperature, comparing their performances with a commercial indium oxide. After hydrothermal synthesis, powders were calcined at 400°C for 30 minutes and characterized by laser granulometry, thermal analysis, X-ray diffraction, N₂ adsorption, X-ray Photoelectron Spectroscopy, field emission scanning electron microscopy, and transmission electron microscopy. Sensors were developed by screen-printing the sensing material onto α -alumina substrates with platinum interdigitated electrodes. After drying overnight, sensors were fired at 600°C for 1 h in air.

The sensor response was measured in the range 25°C – 200°C carrying on all measurements in a flow chamber at a constant flow rate of 1 L/min of dry air in the range 200 – 500 ppb O₃. Response time and recovery time (e.g., the times taken for the sensor to attain 90% of total impedance change from its initial impedance value) were detected, together with cross-sensitivity tests towards NH₃, CH₄, humidity, CO, NO₂, CO₂ and N₂O.

Sensor's response (R) was defined as the ratio between impedance of the film under gas exposure at the equilibrium and the impedance under dry air. Best results were obtained at 100°C, with R equal to 464 under 500 ppb O₃. These results are extremely encouraging and support the exploitation of tungsten-doped indium oxide as low-temperature ozone sensors.

Highlights

- Nanocrystalline In₂O₃ and W-doped In₂O₃ powders were prepared by hydrothermal route
- WO₃ slightly modifies the lattice parameter a of the cubic In₂O₃ structure
- Ozone sensing properties of sensors were studied in the range 200 - 500 ppb O₃
- Best results were obtained at an operating temperature as low as 100°C
- Sensor response/recovery time are quite short in the studied O₃ concentration range

Keywords: indium oxide; tungsten-doped indium oxide; hydrothermal synthesis; impregnation; ozone detection.

1. Introduction

O₃ is one of the most reactive form of oxygen, and it is generated in the troposphere after a chain of photo-chemical reactions between sunlight, hydrocarbon and nitrogen oxides gases. Recently, ozone concentration in the lowest level of atmosphere has enhanced as a consequence of the interaction between sunlight and a wide range of chemicals emitted in the troposphere by anthropogenic activities, like vehicles and industries. In addition, tropospheric ozone is a byproduct of industrial and urban pollution [1].

Nowadays ecologically clean ozone technologies are spreading their interest: it is well known that O₃ can be widely used in medicine, as well as in different technological processes [2–4]. Despite its

use in processes as water depuration and purification of gases, ozone is hazardous to the human health, especially for the respiratory system. In fact, ozone may worsen chronic respiratory diseases such as asthma, compromising the ability of the body to fight against respiratory infections [5].

As a result, ozone intoxications cause inflammation and congestion of the respiratory apparatus [6–7]. For this reason, monitoring ozone concentration at ground level appears of the highest importance. In 2015, EPA (United States Environmental Protection Agency) revised the National Ambient Air Quality Standards (NAAQS) for ground-level ozone not to exceed 70 ppb, with the goal to improve public health protection [8].

In this frame, the analytical techniques developed to monitor ozone concentration should work in a quite wide range of concentration (0.01-10 ppm) [1]. Ozone sensor with detection limit (LOD) in the sub-ppm level should be applied in environmental monitoring, while in industrial and commercial applications the expected concentrations are commonly in the order of some ppm.

Nowadays, a wide range of sensing technologies have been developed for measuring ozone concentration at ground level, such as optical detection [9], ultraviolet (UV) light absorption [10] chemiluminescence analyzers [11], fluorescence measurements [12], potassium iodide [13], direct amperometry determination [14], and gas-sensitive semiconductors [15-16].

Among all these techniques, the latter evidences a great potential, compared with traditional ozone measurements methods, because of semiconductors' low cost, ease of operation, high long-term reliability and stability together with a relatively moderate power dissipation [1].

Traditionally, the conduction mechanism of semiconducting metal oxide (SMO) is explained by gas-related modulation of Schottky barriers resulting in space-charge layers at grain boundaries of n-type semiconducting oxides [17-19]. This is true for the most investigated materials: SnO₂, ZnO, WO₃ and In₂O₃ [19-23]. Nonetheless, the temperature of maximum sensor response depends mainly on the grain size and film thickness [24, 25].

Responses in the range 10²-10³ in the ppm range of ozone concentration appear to be the optimal for ozone sensors market [1]. Indium oxide nanostructures with various morphology have been

extensively used to detect ozone [26-29]. However, only few papers report a maximum response to ozone in a temperature range below 100°C [30-31], without a UV illumination. In order to improve the sensing features towards ozone of indium oxide films, many studies have assessed the efficiency of doping with metal oxides such as Ga₂O₃, Fe₂O₃, CeO₂, ZrO₂, NiO, ZnO and SnO₂ [32]. WO₃, a n-type ozone sensitive oxide [33], improves sensitivity of the metal oxide film, creating adsorption centers with an enhanced affinity for oxygen species, since unusual valence states (W⁶⁺) are produced [34]. Many experiments have assessed that bulk-doping of semiconductor metal oxides is an efficient method to increase sensor response, modifying the surface reactivity and the bulk electrophysical features, defect chemistry and porosity of the matrix.

In this research, a commercial indium oxide nano-powder supplied by Sigma-Aldrich (SA-In₂O₃) was selected as reference sensing material for ozone detection in sub-ppm concentration range, and its sensing properties were compared with 1, 2.5 and 5 wt% of WO₃-doped In₂O₃ sensors realized via impregnation method. In₂O₃ was additionally synthesized via hydrothermal route for decreasing the crystallite size as well as, improving the sensitivity and the response and recovery times towards O₃. Finally, sensors prepared at the optimal WO₃ concentration, were tested at the optimum operating temperature and their performances were compared to those of the commercial and the synthesized In₂O₃ sensors.

2. Experimental

2.1. Powder synthesis

In₂O₃ powder was synthesized by hydrothermal route and referred to as HT-In₂O₃. To perform the synthesis, analytical grade reagents were used without further purification: indium (III) nitrate pentahydrate (In(NO₃)₃·5H₂O, 99.99%, metal basis, Alfa Aesar), hexadecyltrimethylammonium bromide (CTAB, ≥ 99.8%, Sigma Aldrich) used as a capping agent and sodium hydroxide (ACS > 98% pellets, Sigma Aldrich) used as a mineralizer. Following previous literature [35], the In(NO₃)₃·5H₂O: CTAB: NaOH molar ratio of 1:1.96:3 was used. The role of CTAB to confer stability to nanoparticles during

crystal growth and control of their morphologies, size and shape has been already demonstrated in literature [35]. Sodium hydroxide has been chosen as mineralizer, as it induces a smaller crystallite size of the wet-synthesized product as compared to other agents, like urea [35].

After dissolution in distilled water of all the reagents, the solution was stirred at room temperature for 30 min. It was then transferred into a Teflon-autoclave and kept at 70°C for 24 h and then at 120°C for 12 h, providing a white powder.

The precipitate was washed several times with distilled water and twice in absolute ethanol in order to eliminate the synthesis by-products, and finally dried at 70°C overnight. The powder was finally calcined at 400°C for 30 min, to induce the crystallization of In_2O_3 [36]. After the annealing procedure, the color of the product varied from white to pale yellow, denoting the formation of the In_2O_3 phase from $\text{In}(\text{OH})_3$ [36].

A commercial In_2O_3 powder, supplied by Sigma-Aldrich (SA- In_2O_3), was also used as reference material. According to the supplier [37], this powder is characterized by 99.9% purity and particle size < 100 nm, as determined by TEM analysis.

Both SA- In_2O_3 and HT- In_2O_3 powders were doped with WO_3 by impregnation method [38]. WCl_6 (\geq 99.9% trace metals basis, Sigma Aldrich) was dispersed in dichloromethane (ACS, \geq 99.8%, ChemLab) before addition of the powders. The suspensions were stirred for 3 h at room temperature and dried at 40°C. To eliminate the chloride by-product, the powders were washed twice by centrifugation in water. In the case of SA- In_2O_3 , impregnation was carried out by using three different amounts of WCl_6 to obtain 1, 2.5 and 5 wt% of WO_3 -doped In_2O_3 powders. HT- In_2O_3 powder was doped at the optimal WO_3 concentration (2.5 wt%) determined for the commercial powder [38]. Thus, from now, when tungsten trioxide content is not mentioned, doped samples contain 2.5 wt% of WO_3 .

After drying at 80°C overnight, the powders were annealed at 400°C for 3 hours with a heating rate of 2°C/min, resulting in tungsten trioxide-doped indium oxide (SA-W- In_2O_3 and HT-W- In_2O_3) products.

2.2. Powder and film characterization

The particle size distribution of doped and undoped powders were determined by laser granulometry (Mastersizer 3000, Malvern, Worcestershire, UK) on alcoholic suspension dispersed under sonication for 5 minutes.

Differential Thermal Analysis-Termogravimetry (DTA-TG, STA 409, Netzsch, Selb, Germany) was performed on HT-In₂O₃ precursor up to 400°C (heating rate of 10°C/min) under static air.

X-Ray diffraction (XRD) was carried out on SA and HT doped and undoped powders. In addition, the same analysis was carried out after the addition of quartz as an internal standard, to evaluate possible shifts in the diffraction pattern after doping. Spectra were recorded on a Pan'Analytical X'Pert Pro instrument (Pan'Analytical, Almelo, The Netherlands) with Cu K radiation (0.154056 nm) in the range between 5 and 70° 2θ, working with a step size of 0.0065° of 2θ and an acquisition time per step equal to 23 s. Diffraction patterns were indexed by means of the Powder Data File database (P.D.F. 2000, International Centre of Diffraction Data, Newtown Square, PA, USA).

The average crystallite size was estimated according to the Scherrer equation, for a qualitative comparison with the available data in literature (1):

$$D = k\lambda / \beta \cos\theta \quad (1)$$

where k is a constant assumed to be equal to 0.9, λ is the Cu K α wavelength (0.154056 nm), θ is the half of Bragg (radians) and β is the full width at half maximum of the X-ray diffraction peaks, that are commonly associated with the crystallite size, presence of defects, and peak broadening caused by the instrument [39].

Cell parameters for cubic In₂O₃ phase were calculated for the three principal planes (222) (400) and (440), using the following equation based on XRD data (2):

$$d_{hkl} = \frac{a}{\sqrt{h^2 + k^2 + l^2}} \quad (2)$$

where d_{hkl} is the lattice spacing of the (hkl) plane and a is the lattice spacing.

Nitrogen adsorption and desorption isotherms were determined with an ASAP2020, Micromeritics ASAP 2020 Plus Physisorption (Norcross, GA, USA), at the temperature of -196°C. Before nitrogen adsorption–desorption investigations, each sample was degassed at 150°C for 8 h. Moreover, Brunauer–Emmett–Teller (BET) model was applied to determine the specific surface areas of the samples.

X-ray Photoelectron Spectroscopy (XPS) was carried out with a PHI 5000 Versaprobe (Physical Electronics, Chanhassen, MN, USA) (monochromatic Al K α X-ray source with 1486.6 eV energy, 15 kV voltage, and 1 mA anode current) to investigate the surface chemical composition of the semiconductor together with possible In and O shifts after doping.

Moreover, morphologies of powders and films were examined by means of a FESEM (Zeiss Supra-40, Oberkochen, Germany), also in cross-section to evaluate the film thickness. FESEM was equipped with an Oxford Energy Dispersive X-ray detector. Observations were performed on Cr coated specimens. Finally, observations and chemical analysis of the samples were carried out by HR-TEM coupled with energy dispersive X-ray spectroscopy (TEM-EDS). Investigations were performed with a JEOL 3010-UHR (Peabody, MA, USA) instrument, working with an acceleration potential of 300 kV and equipped with an Oxford Inca Energy TEM 200 EDS X-rays analyzer. Quantitative compositional studies were carried out using the Oxford INCA Microanalysis Suite software, and the mean elemental composition resulted from the average of 5 measurements performed in different regions.

2.3 Fabrication and measurement of gas sensors

Sensors were realized by screen-printing technique onto α -alumina substrates (Coors Tek, Golden, CO, USA, ADS-96, 96% alumina, 0.85 cm x 1.7 cm) with platinum interdigitated electrodes (5545-LS, ESL, King of Prussia, PA, USA) over the ceramic substrate. These electrodes were fired at 980°C (2°C/min heating and cooling ramps) for 18 minutes resulting in a high-grade adhesion and optimizing their electrical conductivity at the same time, according to the manufacturer's

recommendations. FESEM observations showed that electrodes have 400 μm in width and are spaced 450 μm each other. Their thickness is about 6 μm .

Inks for screen printing were realized by mixing the materials with an organic vehicle (ethylene glycol monobutyl ether, Emflow, Emca Remex, USA), to achieve the proper rheological characteristics with the right viscosity, and polyvinyl butyral (PVB, Sigma Aldrich) that acts as temporary binder for the powder before thermal treatment. The ink was sonicated for 5 min in an ultrasonic bath to disperse the sensing material and to dissolve the PVB in the solvent.

After screen-printing deposition with a 325-mesh steel mask, sensors were dried at 80°C overnight and fired at 400°, 500° and 600°C in air for 1 h (2°C/min heating and cooling ramps). This process is required to remove all the organic residues from the solvent and to ensure the adhesion with the substrate at the same time.

Once fabricated, sensors were tested in a home-made system, where O_3 was generated by a UV lamp (SOG-01, UVP-LLC Cambridge, UK) from a constant air flow of 1000 SCCM (standard cubic centimeters) of compressed air. The modulation of O_3 concentration was realized by varying the length of lamp exposed and was determined by means of the calibration curves given by the manufacturer.

Ozone losses due to adsorption and reactions in pipelines and measuring chamber was prevented by using suitable materials as polytetrafluoroethylene (PTFE) and polyvinylidene fluoride (PVDF) tubes.

First, sensors $\text{SA-In}_2\text{O}_3$, $\text{SA-W-In}_2\text{O}_3$, $\text{HT-In}_2\text{O}_3$ and $\text{HT-W-In}_2\text{O}_3$ were tested towards O_3 500 ppb at different temperatures (from room temperature to 200°C, in steps of 25 degrees) to evaluate the optimum working temperature for each sensing material. Different O_3 concentrations were then investigated at the optimum temperature, between 200 and 500 ppb in steps of 100 ppb, and the results were compared with literature. Cross-sensitivity tests were also carried out adopting the same operating conditions described above. Target gas was diluted with dry air by means of flow meters (Teledyne Hastings Instruments HFM 300 controller and flow meters HFC 302, Teledyne Hastings, Hampton, VA, USA). All the sensors were heated by a Ni-Cr wire, located underneath the sensor,

alimented with a DC power supply (Peak Tech, Nanjing, Jiangsu, China). A PT1000 resistance temperature detector (RS Pro, London, UK) was used for temperature determination of sensors. Cross-sensitivity measurements were carried out towards both oxidizing and reducing gases. Specifically, the sensitivity towards NH₃ (50 ppm in air), CH₄ (50 ppm in air), CO₂ (500 ppm in air), humidity (30, 50, 70% of relative humidity (RH) at room temperature), NO₂ (250 ppb in air), CO 10 ppm and N₂O (15 ppm in air) was investigated under the same flow of 1000 SCCM.

During tests under constant gas flow, film impedance was measured by means of a LCR meter (Hioki 3533-01, Nagano, Japan). Impedance's measurements were carried out by means of a constant AC tension of 1 V at 1 kHz, and sensors were put into a chamber of 0.1 L volume.

The response of the sensor (R) was calculated according to equation (3) for oxidizing gases and to equation (4) for reducing analytes:

$$R: Z_g/Z_0 \quad (3)$$

$$R: Z_0/Z_g \quad (4)$$

Where Z_g and Z_0 are respectively the impedances under target gas and the starting (under dry air flow) of the oxide layer at the equilibrium.

The response times (the time needed by a sensor to achieve 90% of the total impedance change in the case of gas adsorption) together with the recovery times (the time necessary to reach 90% of the total impedance variation in the case of gas desorption) were also determined in the present work.

3. Results and discussion

3.1 Powder and film characterization

In Fig. 1, the DTA-TG curves related to HT-In₂O₃ precursor, just dried at 120°C, are depicted. The DTA curve shows a small exothermic peak at 207°C, that can be attributed to the decomposition of the residual surfactant in the sample [40]. Then, a broad endothermic peak is detected at 317°C,

which can be related to the transformation of indium hydroxide into indium oxide. Moreover, TG analysis displays a total weight loss of 14.8% between 270°C and 350°C, with a maximum slope at 305°C. It should be mentioned that the weight loss corresponding to the complete conversion of the indium hydroxide into indium oxide is equal to 16.3% [40], suggesting a not complete crystallization of the oxide phase in the present analysis. On the ground of this result, all powders were annealed at 400°C for 3 h, to achieve a complete conversion.

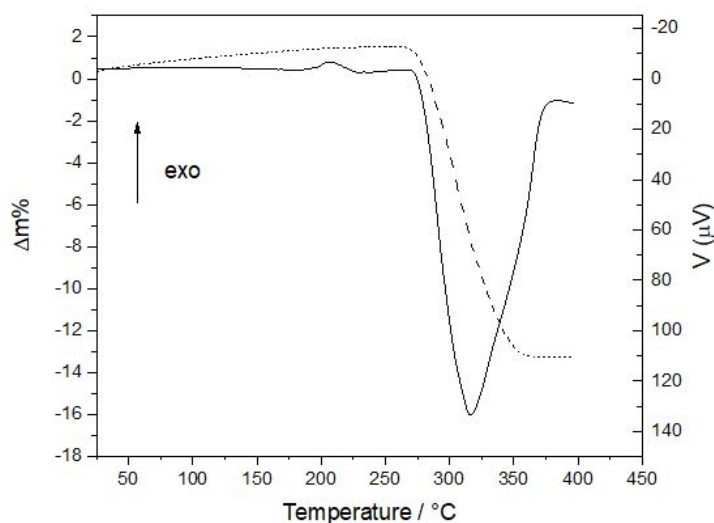


Fig 1. TG-DTA curve of HT-In₂O₃ precursor TG: dashed line; DTA: straight line.

XRD analyses, carried out on powders calcined at 400°C/3h, confirmed the presence of pure cubic indium oxide in the bixbyte type (JCPDF card n°06-0416), as shown in Fig. 2 for doped and undoped SA-In₂O₃ (a) and HT-In₂O₃ (b) powders. Here, no traces of In(OH)₃ phase were detected.

The XRD pattern of HT-powder is characterized by broader peaks as compared to SA-samples, suggesting a smaller crystallite size and a lower degree of crystallization. In fact, by applying the Scherrer equation on the following peaks: (211), (222), (400), (440), (541), a crystallite size equal to 48 ± 3.5 nm was determined for both SA-In₂O₃ and SA-W-In₂O₃. An almost halved value (26 ± 2.8 nm) was found for HT-In₂O₃ and HT-W-In₂O₃ powders. These results are in accordance with a previous work of Bagheri-Mohagheghi [41], showing crystallite size in the range 3-25 nanometers

for hydrothermal synthesized indium oxide powders, and an almost doubled value (10-45 nm) for a sol-gel synthesized powder.

SA-In₂O₃ and SA-W-In₂O₃ powders showed almost superimposable XRD patterns (Fig. 2a) and this is true also for the HT-In₂O₃ and HT-W-In₂O₃ powders (Fig. 2b). Only a small and broad peak at about 24.07° of 2θ was observed in both W-doped powders, and it is associated to the crystallization of the WO₃ phase. Precisely, the band was attributed to the sum of the three main peaks of WO₃ in monoclinic phase (reference n° 43-1035), corresponding to the (002), (020) and (200) crystallographic planes respectively located at 23.12°, 23.59° and 24.38° 2θ. No traces of any other phases besides cubic In₂O₃ and monoclinic WO₃ were detected. It should be specified that the crystallization of WO₃ occurs at temperatures lower than 400°C, as confirmed by XRD analysis carried out on the WCl₆ precursor thermally treated at 400°C for 3 h (XRD pattern in Fig. 2c) resulting in the formation of monoclinic WO₃.

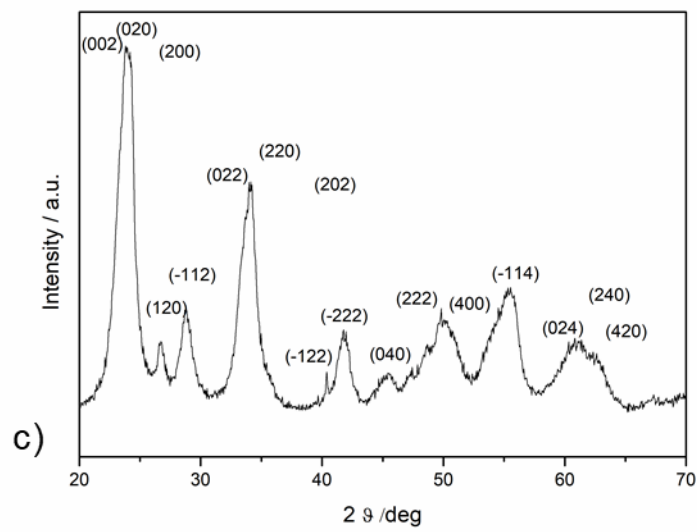
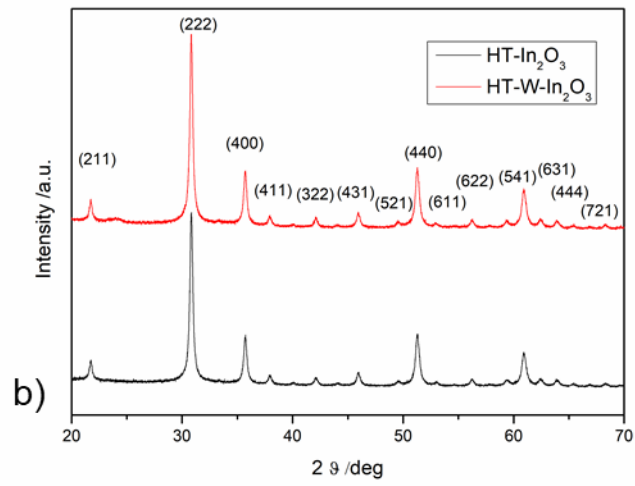
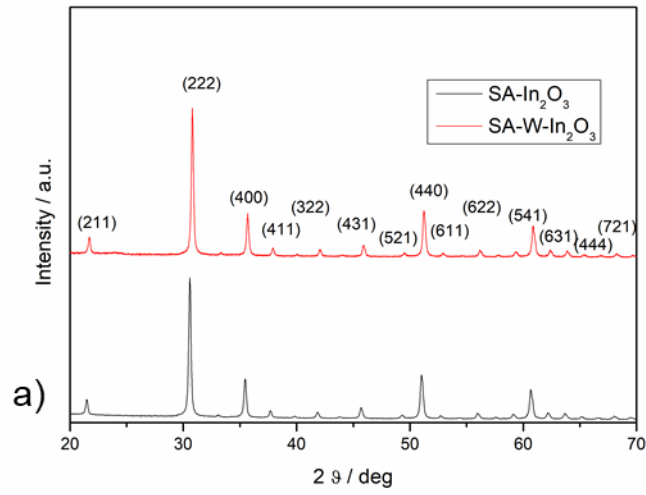


Fig. 2. XRD pattern of: a) SA-In₂O₃ (black line) and SA-W-In₂O₃ (red line) calcined at 400°C/3h; b) HT-In₂O₃ (black line) and HT-W-In₂O₃ (red line) calcined at 400°C/3h; c) WO₃ powder, obtained by calcination at 400°C for 3h of WCl₆ precursor.

In order to evaluate a possible shift of the diffraction peaks, XRD analysis were repeated by using quartz as an internal standard. Considering the six main peaks related to (211), (222), (400), (431), (440) and (622) planes, a certain shift to lower 2θ values (0.03° of 2θ) was determined for the doped powders as compared to the un-doped ones. Thus, lattice parameter a was slightly increased in SA-W-In₂O₃ and HT-W-In₂O₃ samples as compared to the un-doped respective materials, as reported in Table 1. This change in the lattice constant can be due to the substitution by W dopants in the In₂O₃ cell, in spite of a much smaller ionic radius for the octahedral W(VI) (74 pm), compared to octahedral and trigonal prismatic In(III) (94 pm) [42]. A decrease in cation occupancy is then necessary to maintain the electrical neutrality of the lattice cell when replacing In³⁺ by W⁶⁺ ions. This decrease in cation occupancy may be responsible for cell's distortion and for the increase of bond length [43], resulting in the observed slight increase of the lattice constant.

Table 1. Lattice parameters and crystallite size calculated by Scherrer equation for the four powders obtained.

Material	Crystallite size (nm)	Lattice parameter (a, nm)
SA-In ₂ O ₃	48	1.0078
SA-W-In ₂ O ₃	48	1.0089
HT-In ₂ O ₃	26	1.0083
HT-W-In ₂ O ₃	26	1.0092

In both cases, doping with WO_3 causes an increase of 0.1% in lattice parameter a . Indium oxide crystallizes in a cubic bixbyte-type structure consisting in a body centered cubic unit cell (BCC) belonging to the space group Ia3 number 206, where In atoms lay in the centers of the cube and oxygens stay on the vertices with an oxygen vacancy per each base of the cube. The overall structure consists of two types of In atoms surrounded by oxygen in the octahedral and trigonal prismatic coordination, alternatively. Both coordination groups may be described as distorted octahedra: probably, after doping and thermal treatment, WO_3 partially enters in the crystal lattice of In_2O_3 , distorting the BCC cell.

As a summary of the XRD analyses, we can postulate a twofold role of W-doping within the In_2O_3 matrix: a partial crystallization of WO_3 on the In_2O_3 surface (as indicated by the new broad XRD signal identified in the doped-powders), and a partial WO_3 solubilization inside the In_2O_3 matrix (as indicated by the lattice parameters change after doping).

In Fig. 3, the particle size distribution of doped and un-doped SA and HT powders are depicted.

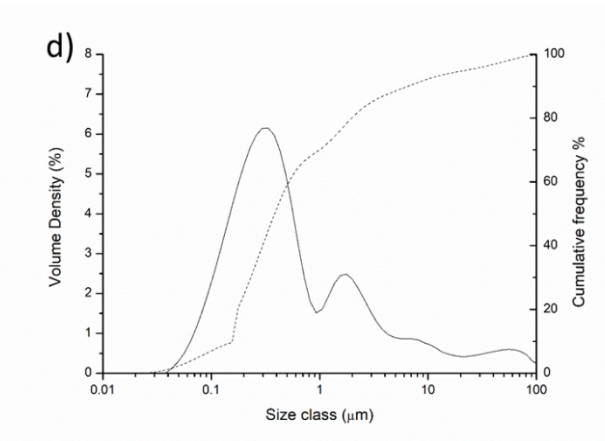
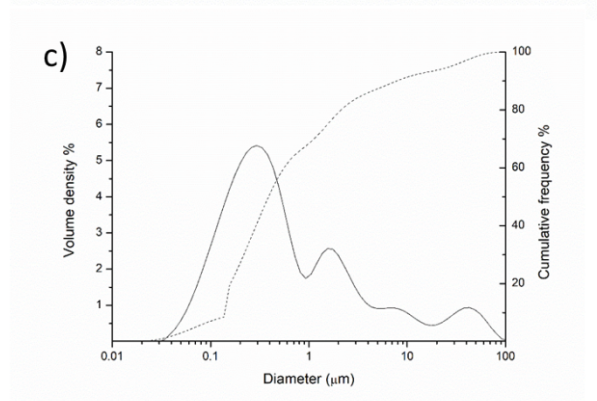
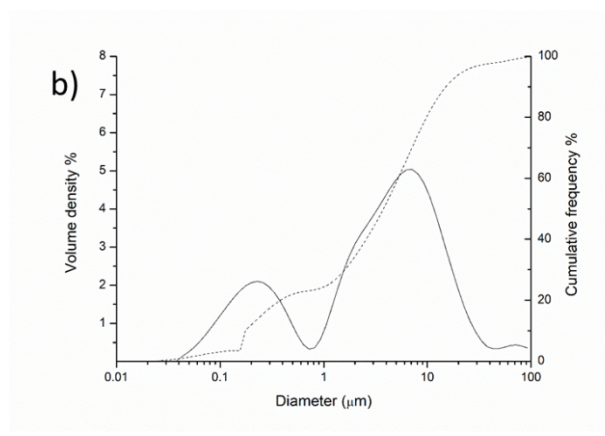
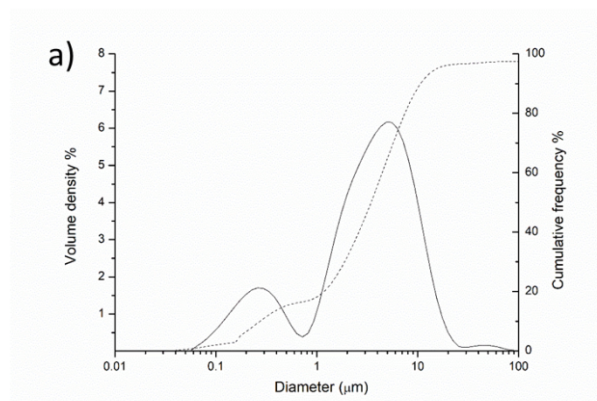


Fig. 3. Particle size distribution of SA-In₂O₃ (a); SA-W-In₂O₃ (b); HT-In₂O₃ (c); HT-W-In₂O₃ (d) powders, in volume density % (straight line) and as cumulative frequency % (dashed line).

Laser granulometry represented in Figure 3 of doped and undoped indium oxide powders evidenced that both SA-In₂O₃ and SA-W-In₂O₃ powders exhibit a multimodal distribution: the maxima of the most evident peaks are located at 0.25, 2.5, 5,6 and 45 μm for SA-In₂O₃ and at 0.22, 2.1, 7.5 and 68 μm for SA-W-In₂O₃. In the case of the synthesized powders, HT-In₂O₃ distribution shows maxima at about 0.23, 1.8, 7 and 40 μm and HT-W-In₂O₃ at 0.32, 1.8, 12 and 58 μm. The particle size distribution of HT-W-In₂O₃ exhibits a slightly lower d₉₀ value compared to the HT-In₂O₃, that was the smallest among the oxides investigated, in agreement with FESEM observations.

Table 2 collects the values corresponding to the 10, 50 and 90% of the cumulative distribution of all four powders, showing lower values for the HT-powders compared to the SA-ones. In addition, HT-W-In₂O₃ showed the smallest d₉₀ values among all the investigated powders.

Table 2. Particle size corresponding to 10, 50 and 90% of the cumulative distribution for the SA and HT doped and un-doped powders.

Cumulative (%)	SA-In₂O₃ (μm)	SA-W-In₂O₃ (μm)	HT-In₂O₃ (μm)	HT-W-In₂O₃ (μm)
10	0.29	0.18	0.11	0.10
50	3.67	4.02	0.41	1.36
90	11.40	16.00	8.34	4.55

A comparison between the morphology and the structure of the doped SA and HT powders is depicted in Fig. 4, showing the TEM (a, b) and HRTEM (c-f) micrographs of SA-W-In₂O₃ and HT-W-In₂O₃ powders. From the TEM bright-field images, the powders appear slightly agglomerated, with primary particles ranging between 20 and 60 nm in both cases. By HRTEM, lattice fringes of 0.253

nm were measured (see the yellow lines in figures c and e) and associated to the In_2O_3 (400) crystallographic plane. In addition, still by HRTEM micrographs, we can observe the presence of WO_3 nanoparticles on the In_2O_3 surface for both SA-W- In_2O_3 and HT-W- In_2O_3 powders. This was confirmed by chemical analysis performed by EDX nanoprobe, thus strengthening the hypothesis that WO_3 is present not only in the In_2O_3 lattice as evidenced by XRD analysis, but it is also situated on the surface of In_2O_3 as nanoparticles. Finally, no evidence of the lattice spacing corresponding to the principal planes of WO_3 , such as (200), (020) and (002) was found in such micrographs, probably due to the very small size of WO_3 grains and their poor crystalline grade, making difficult its clear detection.

Inks were prepared from both SA and HT powders, and used to develop gas sensing films, as described in the Experimental section. In Fig. 5, FESEM micrographs of all developed films, after calcination at 600°C for 1h, are depicted. SA- In_2O_3 (Fig. 5a) and SA-W- In_2O_3 (Fig. 5b) films show a very homogeneous microstructure, with primary particles ranging between 50-70 nm ($61.12 \pm 8.94 \mu\text{m}$) and characterized by almost spherical shape. The agglomerates diameters are in the range of few microns, and no significant modification in size and shape of primary particles was detected after doping.

HT- In_2O_3 (Fig. 5c) and HT-W- In_2O_3 (Fig. 5d) films show a slightly less homogeneous and more porous microstructure, but still characterized by very fine grains. In fact, the primary particles, characterized by cubic or even sharp edge morphologies, with size between 30 and 40 nm ($34.97 \pm .6.77 \mu\text{m}$), are clearly evident. Particles present a slight agglomeration, with agglomerates in the range 1-3 μm . The HT-W- In_2O_3 material shows approximately the same morphology of the un-doped HT- In_2O_3 .

Sensor thickness was measured by FESEM in cross-section (Fig. 5e) and a value of $20.1 \pm 1.2 \mu\text{m}$ was obtained as an average of 10 measurements.

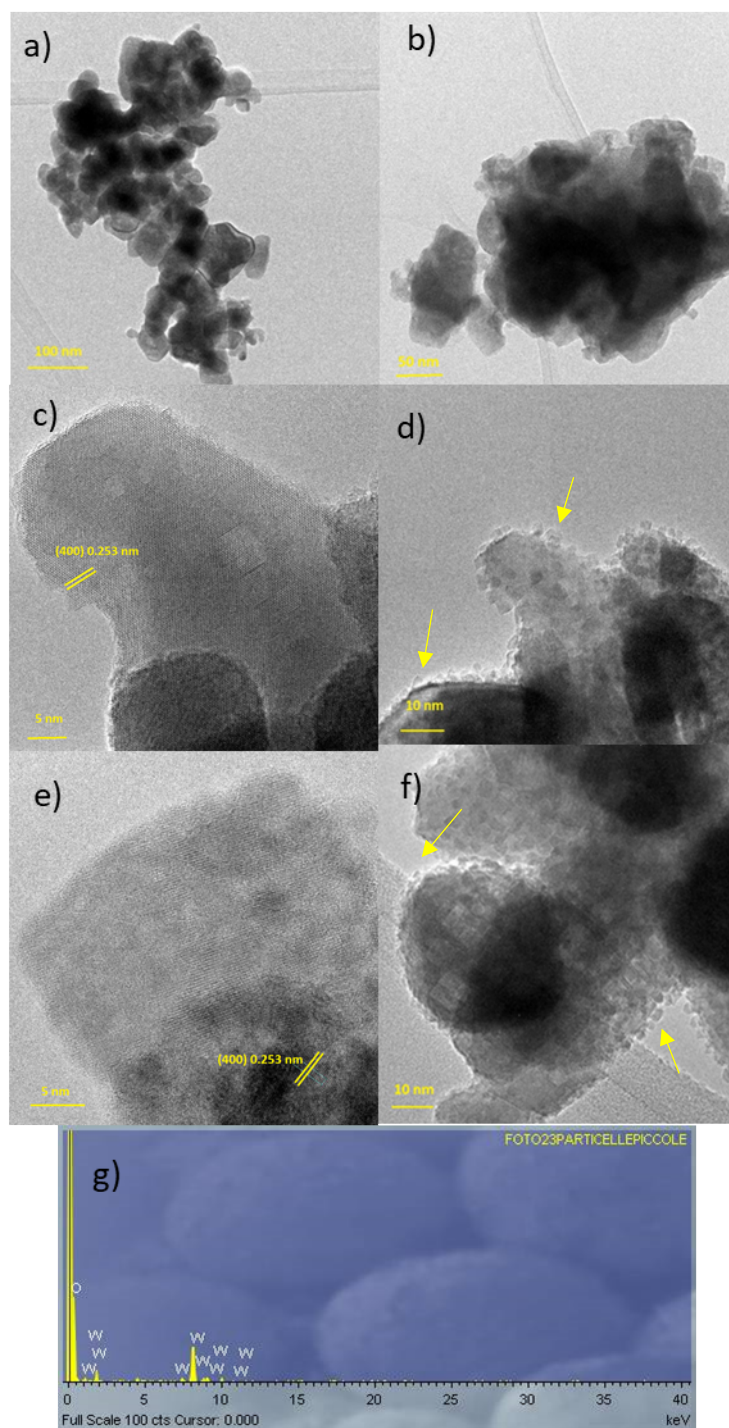


Fig. 4. TEM micrographs (a, b) of SA-W-In₂O₃ and HT-W-In₂O₃, respectively. HRTEM images of SA-W-In₂O₃ (c, d) and of HT-W-In₂O₃ (e, f). All powders were thermal treated at the same temperature (600°C/1h). The yellow arrows show the WO₃ nanoparticles identified by EDX analysis (g).

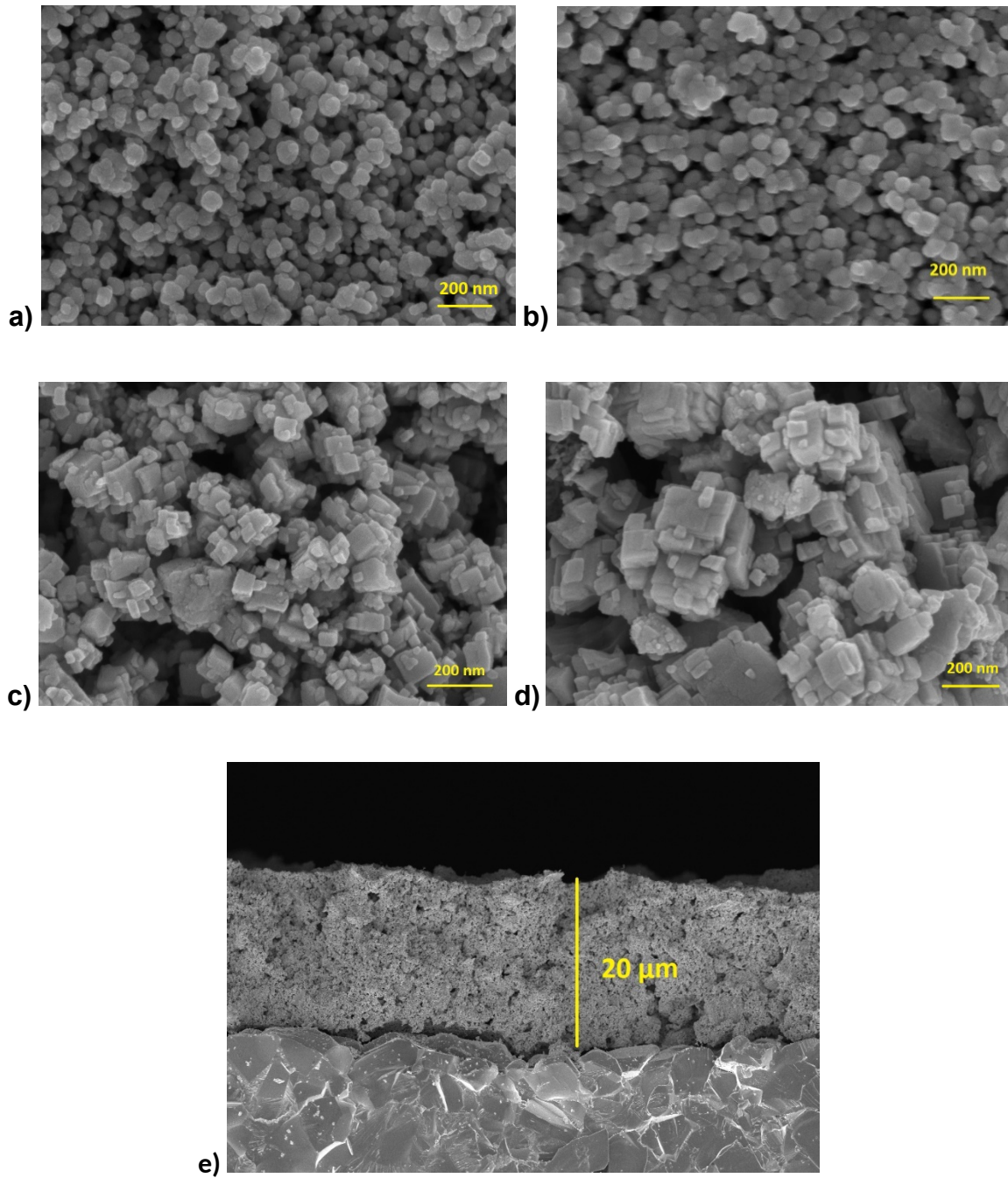


Fig. 5. FESEM micrographs of sensors (150 kx): SA- In_2O_3 (a), SA-W- In_2O_3 (b), HT- In_2O_3 (c), HT-W- In_2O_3 (d) and an image in cross-section of the sensitive layer (e).

Annealing at 600°C leads to a certain increase of the crystallite size as compared to the 400°C -calcined powders. In fact, for the HT powders, the crystallite size increased from 26 nm to 39 nm after calcination at 600°C . However, such size was still smaller than the respective 600°C -calcined SA powders, whose crystallite size was about 54 nm.

In addition, FESEM observations performed perpendicularly to screen-printed sensors (not shown here) allowed to estimate the film thickness: values of $20.6 \pm 2.7 \mu\text{m}$ and $21.4 \pm 1.9 \mu\text{m}$ were respectively determined for SA-In₂O₃ and HT-In₂O₃ films.

The N₂ adsorption isotherms for all four materials after the same firing temperature (600°C) were performed. First, the hydrothermal synthesis leads to a higher SSA compared to the commercial powder: it was in fact 13.3 m²/g for SA-In₂O₃ and more than double (27.7 m²/g) for HT-In₂O₃. In addition, the doping procedure, followed by thermal treatment, leads to a further moderate increase in SSA for both powders, being 15.2 m²/g for SA-W-In₂O₃ and 38.0 m²/g for HT-W-In₂O₃. Thus, a significant higher value was still determined for the synthesized material.

The chemical states of In, O and W atoms in all materials were investigated by XPS, and survey spectra are reported in Fig. 6. From these surveys, it is possible to appreciate the presence of W in the doped samples, SA-W-In₂O₃ (b) and HT-W-In₂O₃ (d).

Moreover, the deconvolution of In, O and W peaks in high resolution was performed. Fig. 7 shows the spin-orbit split for indium 3d_{5/2} and In 3d_{3/2} of trivalent indium for the commercial powders. The 3d characteristic peaks were measured respectively at 443.89 eV and 451.45 eV, descriptors of the binding energy of In³⁺ ion in the SA-In₂O₃ [44]. Those peaks were measured at 444.25 eV and 451.80 eV in the case of SA-W-In₂O₃, with a moderate shift at higher binding energy. The same trend was measured for HT-In₂O₃ and HT-W-In₂O₃ (not shown), where the In 3d_{5/2} and 3d_{3/2} peaks were determined at 444.16 eV and 451.60 eV for the un-doped powders, and shifted to 444.39 eV and 451.83 eV in the doped samples. This shift could be due to the different charge density of W⁶⁺ compared to In³⁺, with a smaller ionic radius for W respect to In, as described above. Electrons are provided into the indium matrix from WO₃. Consequently, characteristic peaks of indium are present at higher binding energy due to screening effect, for an electronic interaction between In₂O₃ and WO₃ [45]. A doping element with high Lewis acid strength like W decreases the scattering of charge carriers, thereby increasing the mobility of carriers. This results in screening of the dopant's effective charge. This screening effect weakens the interaction between dopant and charge carriers.

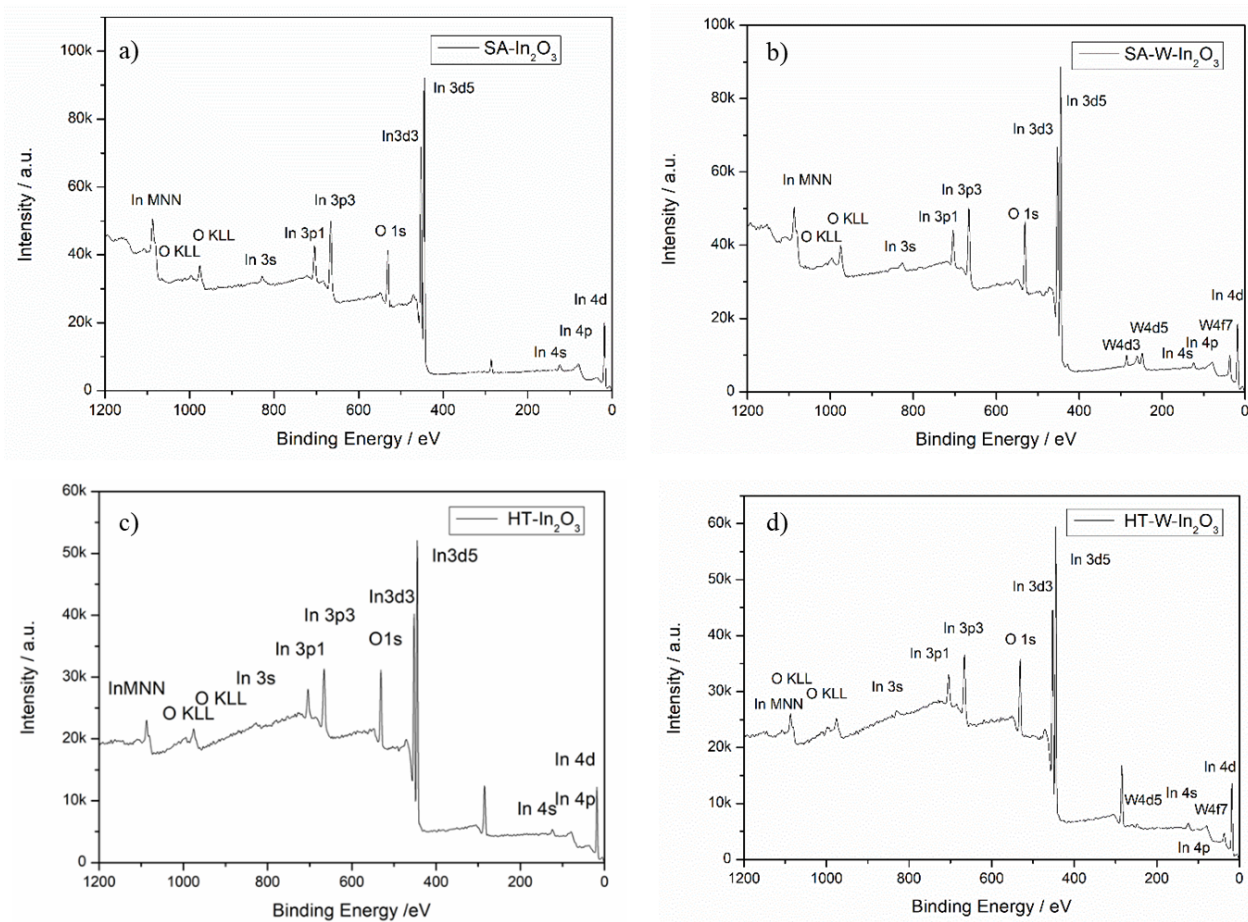


Fig. 6. Survey XPS spectra of: SA-In₂O₃ (a); SA-W-In₂O₃ (b); HT-In₂O₃ (c); HT-W-In₂O₃ (d).

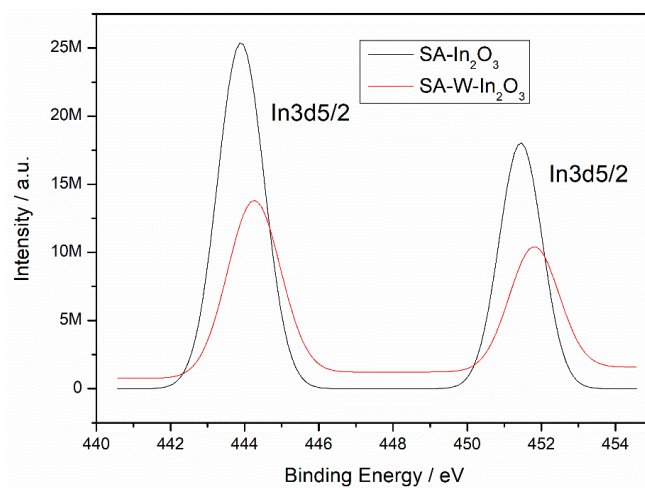


Fig. 7. High resolution XPS spectra of In 3d in: SA-In₂O₃ (black line); SA-W-In₂O₃ (red line) showing a moderate shift towards higher binding energy for the doped powder.

High resolution analyses of O 1s in SA-In₂O₃ and SA-W-In₂O₃ are depicted in Fig. 8 and show that both spectra can be deconvoluted into three components: lattice oxygen (O_l), chemisorbed oxygen (O_c) and hydroxyl oxygen (O_{hy}) [46]. The same behavior was observed in HT-powders as well. The binding energy and relative intensities of these three oxygen peaks are summarized in Table 3.

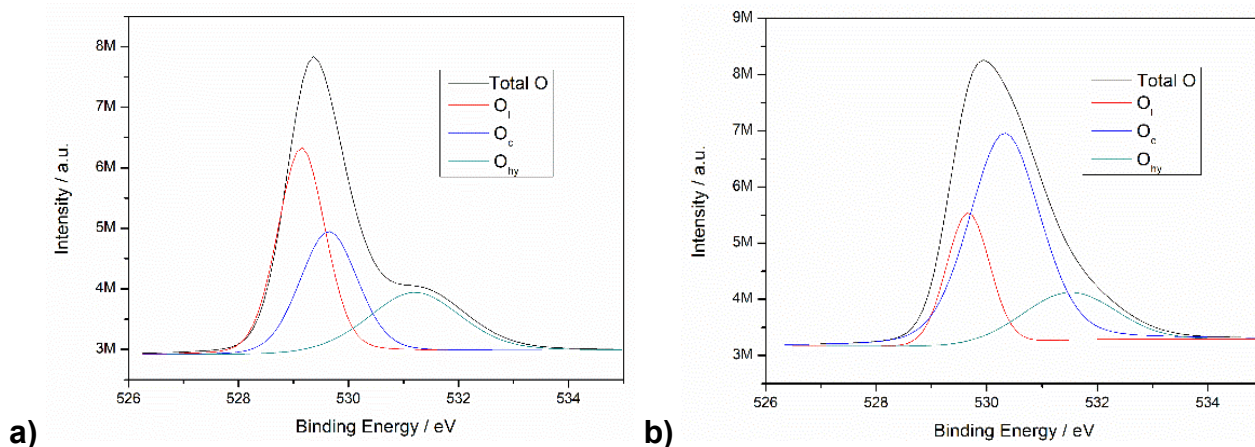


Fig. 8. High resolution XPS spectra of O 1s performed on SA-In₂O₃ (a) and SA-W-In₂O₃ (b). O_l: lattice oxygen; O_c: chemisorbed oxygen; O_{hy}: hydroxyl oxygen.

Table 3. Binding energy value and relative intensities of the oxygen peaks for the 4 powders.

Sample	Binding energy (eV)	Relative intensity (%)	Type of oxygen	Sample	Binding energy (eV)	Relative intensity (%)	Type of oxygen
SA-In ₂ O ₃	529.13	44.0	Lattice	SA-W-In ₂ O ₃	529.66	21.6	Lattice
	529.69	31.3	Chemisorbed		530.32	61.9	Chemisorbed
	531.29	24.7	Hydroxyl		531.51	16.5	Hydroxyl
HT-In ₂ O ₃	529.62	47.1	Lattice	HT-W-In ₂ O ₃	530.00	50.9	Lattice
	530.38	9.4	Chemisorbed		531.29	17.6	Chemisorbed
	531.48	43.5	Hydroxyl		532.11	31.5	Hydroxyl

From these data, we can observe that for both the SA and HT powders, the amount of the chemisorbed oxygen is much higher for the doped materials compared to the un-doped ones.

Specifically, in both SA-W-In₂O₃ and HT-W-In₂O₃, the O_c values were the double than those determined in the respective pure materials. Such behavior can be partially explained by the slight increase of the SSA determined in the doped materials, as previously described. A more important effect can be attributed to the role of the W-dopant, since the doped materials were able to adsorb more oxygen on the surface, because more vacancies could be filled. It is known that the sensing response is expected to occur mainly via electron transfer together with changes in the amount of chemisorbed oxygen species on the sensor surface, so the sensor performances generally improve with the increase of chemisorbed oxygen. In addition, the presence of intrinsic defects from W influence the properties of the semiconductor [46]. Moreover, WO₃ on the surface of In₂O₃ can improve the O₃ sensitivity via spillover-effect (i.e improving the dissociation of O₃). It is well known that spillover-effect is explained by an increased dissociation of oxygen molecules into oxygen ions. In this mechanism, a weak bond is formed between an oxygen molecule and a W atom forming a complex component. This can be easily broken into oxygen ions by trapping free electrons that can diffuse to the surface vacancies of the In₂O₃ NPs. Therefore, more trapped electrons are created, leading to an increase in sensor response.

Besides the increase of the chemisorbed oxygen, the contribution of hydroxyl oxygen is reduced for W-doped materials (from 24.69% to 16.53% for SA- In₂O₃ and SA-W- In₂O₃ and from 43.51% to 31.46% for HT- In₂O₃ and HT-W- In₂O₃), thus more sites are available for ozone adsorption.

In addition, the W 4f high resolution spectrum of SA-W-In₂O₃ is depicted in Fig. 9. We can observe a doublet with binding energies of 35.6 eV for W 4f_{7/2} and 37.7 eV for W 4f_{5/2}, corresponding to the W⁶⁺ oxidation state [47]. Usually, W⁶⁺ signal of WO₃ is observed at binding energies of 36.1 eV (W4f_{7/2} in WO₃) and the W4f region has well separated spin-orbit components with symmetric W4f peaks ($\Delta=2.17$ eV) [47]. The same behavior was observed in HT-W-In₂O₃ sample (not shown).

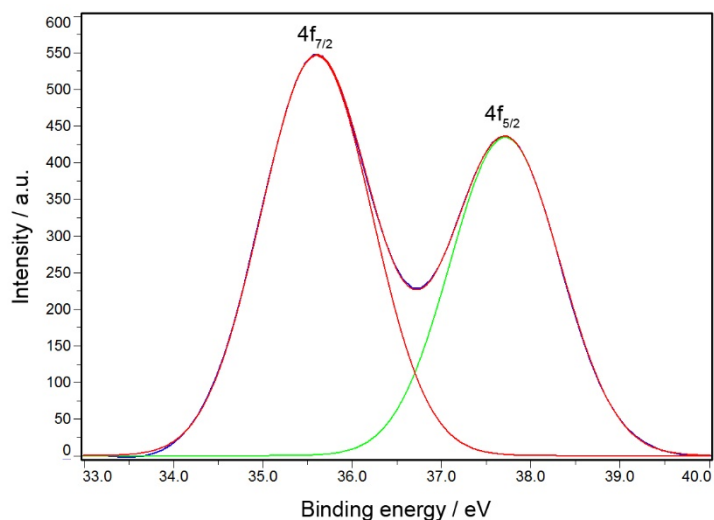


Fig. 9. High resolution XPS spectra of W4f performed on SA-W-In₂O₃.

3.2 Gas sensing properties

For each type of sensor, three different devices were fabricated in order to study the reproducibility of the measurements. A maximum standard deviation of 7% was then calculated respect to the average response of each composition. Firstly, the optimization of the firing temperature (in the range 400-600°C) and of the WO₃ amount (in the range 1.25-5 wt%) was performed on SA sensors. Results are summarized in Fig. 10.

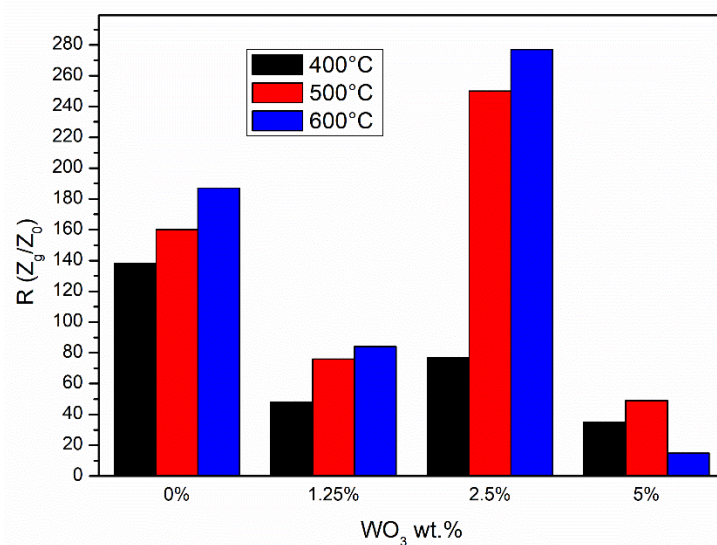


Fig. 10. Sensor film responses prepared with SA-In₂O₃, doped with different concentrations of WO₃: 1.25, 2.5 and 5 wt% and fired at 400°C, 500°C and 600°C for 1 hour under 500 ppb of O₃ in dry air and at 115°C.

First, we can observe that – with the only exception of 5 wt%-W-doped In₂O₃, the sensor response increased by increasing the firing temperature. In fact, calcination at 600°C improved at the same time the adhesion of the thick film upon the ceramic substrate and the ohmic contacts between the film and the interdigitated electrodes. Then, we can observe a significantly improved response at 2.5 wt% WO₃ as compared to the other concentrations. It was supposed that lower amounts were not sufficient to achieve the synergic effects of lattice and surface doping of tungsten oxide into indium oxide. In fact, from XRD analysis, both 1.25 and 2.5 wt% WO₃-SA samples showed the same shift as compared to the undoped powder, suggesting that in the case of 1.25 wt% WO₃, the dopant was predominantly located in the In₂O₃ lattice. At 5 wt%, probably bigger clusters of WO₃ are formed on the In₂O₃ surface decreasing the efficiency of spillover-effect between the two metal oxides.

As a result of the characterization carried out on SA-materials, all sensors were prepared by firing at 600°C for 1 hour, and the doped SA and HT sensors contained 2.5 wt% WO₃. Fig. 11 displays the sensor response for SA-In₂O₃, SA-W-In₂O₃, HT-In₂O₃ and HT-W-In₂O₃. Generally, their impedance increased from hundreds Ohm under dry air up to several tens of kOhm when exposed to O₃ 500 ppb. The optimum working temperature was equal to 115°C for SA- In₂O₃ and SA-W-In₂O₃, and 75°C for HT- In₂O₃ and HT-W- In₂O₃, as depicted in Fig. 11.

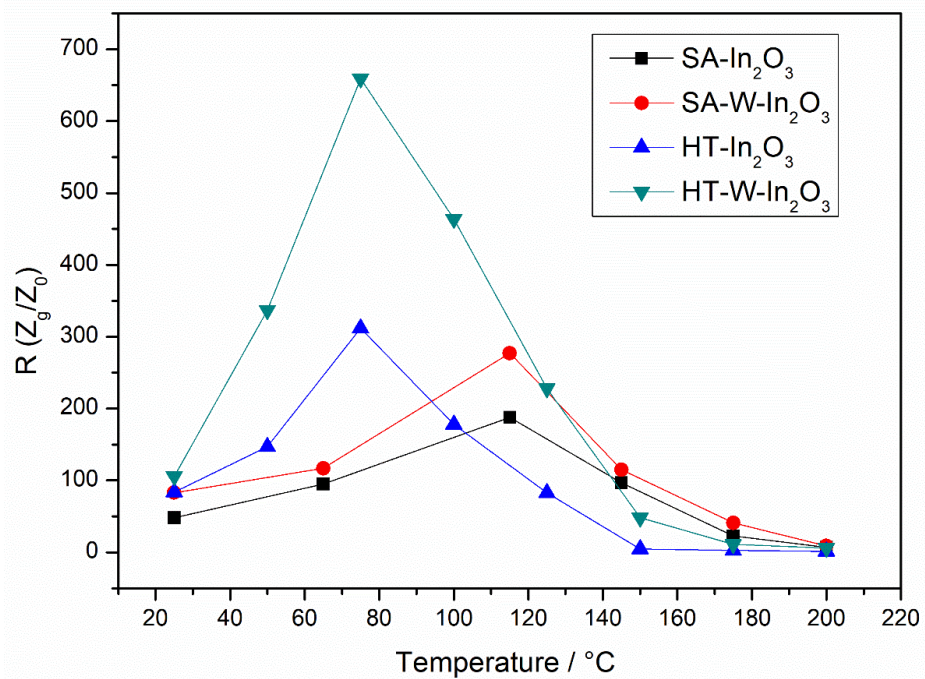
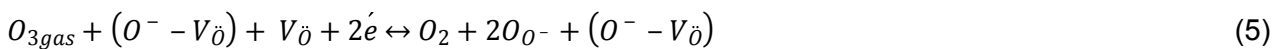


Fig. 11. Sensor film response at different operating temperatures (25-200°C) under 500 ppb O₃:

SA-In₂O₃, SA-W-In₂O₃, HT-In₂O₃ and HT-W-In₂O₃.

Generally, by doping with WO₃, both SA and HT In₂O₃ sensors showed an improvement of performances, because in the doped indium oxides more chemisorbed oxygen ions are present and available in the O₃ adsorption mechanism involving the filling of oxygen vacancies following the equation 5:



In accordance with Kröger-Vink Notation, O_o represent lattice oxygen, whereas V_̄ is an oxygen vacancy. From this reaction, O₃ has a great affinity for the reaction with oxygen vacancies (V_̄) rather than with adsorbed oxygen species, O⁻ - V_̄. Following this route, electrons of the conduction band of the material are consumed. After ozone interaction, the thickness of the depletion layer increases and the concentration of the charge carrier is dropped down, thus the impedance value of the sensor increases. In the case of W-doped indium oxide, O₃ is dissociated quickly by spillover effect in O⁻. This process is promoted by the presence of tungsten trioxide.

The sensor response is increased by 48% after doping for commercial indium oxide at 115°C with no effect on the optimum operating temperature and by 111% for synthesized indium oxide sensors at 75°C. In addition, in the case of HT-powders, optimum operating temperature was significantly decreased (i.e. equal to 75°C), which is consistently lower than the temperature determined for SA ones, which is around 115°C. By synthesizing via hydrothermal route indium oxide nanoparticles, it was possible to increase significantly the sensor response and to decrease at the same time the optimum operating temperature, due to the lower crystallite and agglomeration size together with a higher specific surface area obtained for the HT-In₂O₃. Nevertheless, the response and recovery time at 75°C were quite longer for practical application (around 10-12 minutes), and for this reason the optimum operating temperature was chosen equal to 100°C. In this case, sensor response and recovery times were in the order of 2 minutes after exposure to 500 ppb of O₃ (Table 4).

Impedance variation of HT-W-In₂O₃ sensor (doped with 2.5 wt% WO₃ and fired at 600°C) at the selected optimized temperature, 100°C under different ozone concentrations in the range 200-500 ppb, is displayed in Fig. 12.

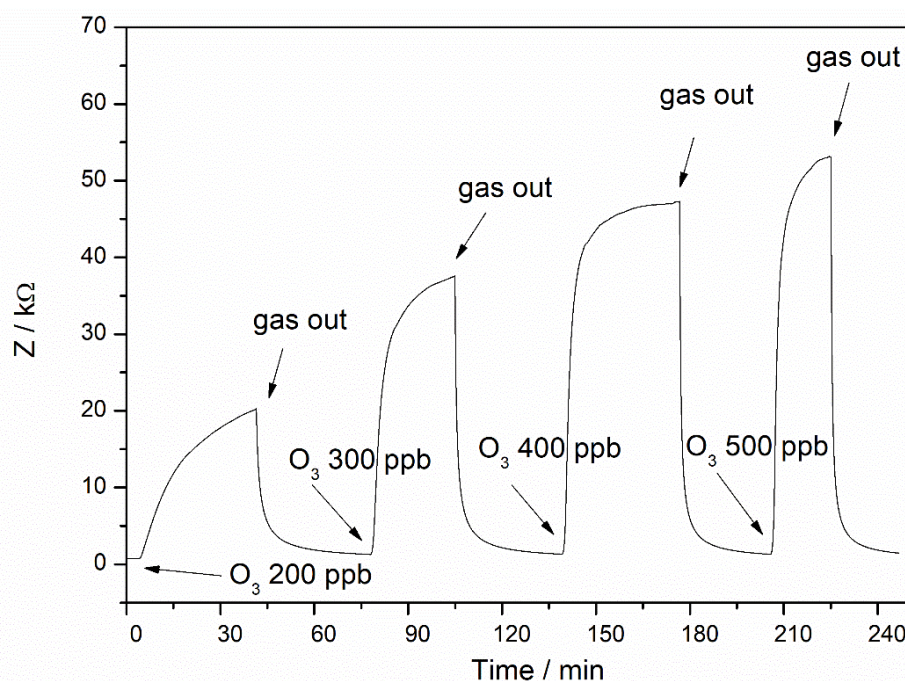


Fig. 12. Impedance variation of HT-W-In₂O₃ film (doped with 2.5 wt% WO₃ and fired at 600°C) towards different concentration of O₃ at 100°C in the range 200-500 ppb.

It appears evident that sensor response and recovery times are both relatively short, in the order of few minutes for the diverse investigated O₃ concentrations, as tabulated in Table 4, and are faster for higher concentration of ozone [48]. Moreover, impedance's variation of two orders of magnitude were measured in the sub-ppm level of O₃ concentration.

Table 4. HT-W-In₂O₃ sensor response and recovery times (respectively the time needed for the sensor to reach 90% of the impedance variation under adsorption and desorption of ozone) at different ozone exposure in the range 200-500 ppb at 100°C.

Ozone concentration (ppb)	Response time (s)	Recovery time (s)
200	992	298
300	567	241
400	387	129
500	267	199

In Fig. 13 the calibration curve of HT-W-In₂O₃ sensor towards O₃ 200-500 ppb at 100°C is depicted, with a linear trend in the concentration range investigated, and a sensitivity equal to 0.879 ppb⁻¹, in accordance with IUPAC's definition.

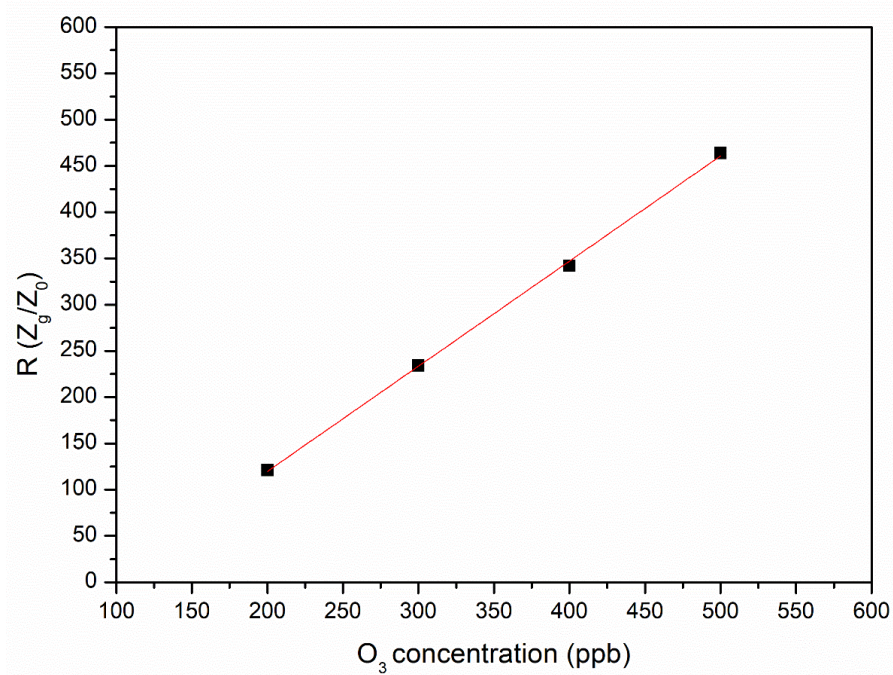


Fig. 13. Calibration curve of HT-W-In₂O₃ film (doped with 2.5 wt% WO₃ and fired at 600°C) towards different concentration of ozone at 100°C.

Long-term stability of HT-In₂O₃ and HT-W-In₂O₃ sensors were evaluated after 3, 6 and 12 months. Sensor responses at 100 °C under 500 ppb of O₃ are depicted in Fig 14. After 1 year of aging, sensor response is still equal to 95% of the fresh sensor response.

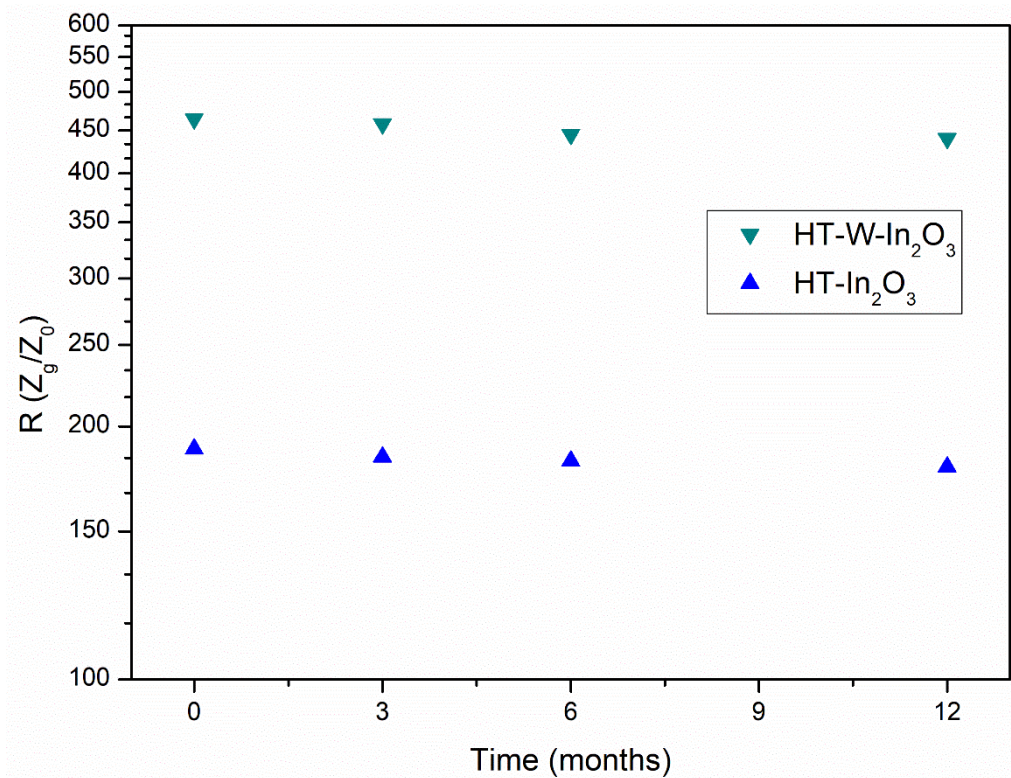


Fig 14. Long-term stability of HT-In₂O₃ and HT-W-In₂O₃ sensors: fresh, after 3, 6 and 12 months under 500 ppb of O₃ at 100°C.

Results of cross-sensitivity tests for all the investigated sensors are depicted in Fig. 15 towards NH₃ (50 ppm), CH₄ (50 ppm), humidity (50 RH%), CO₂ (500 ppm), N₂O (15 ppm), CO (10 ppm) and NO₂ (250 ppb).

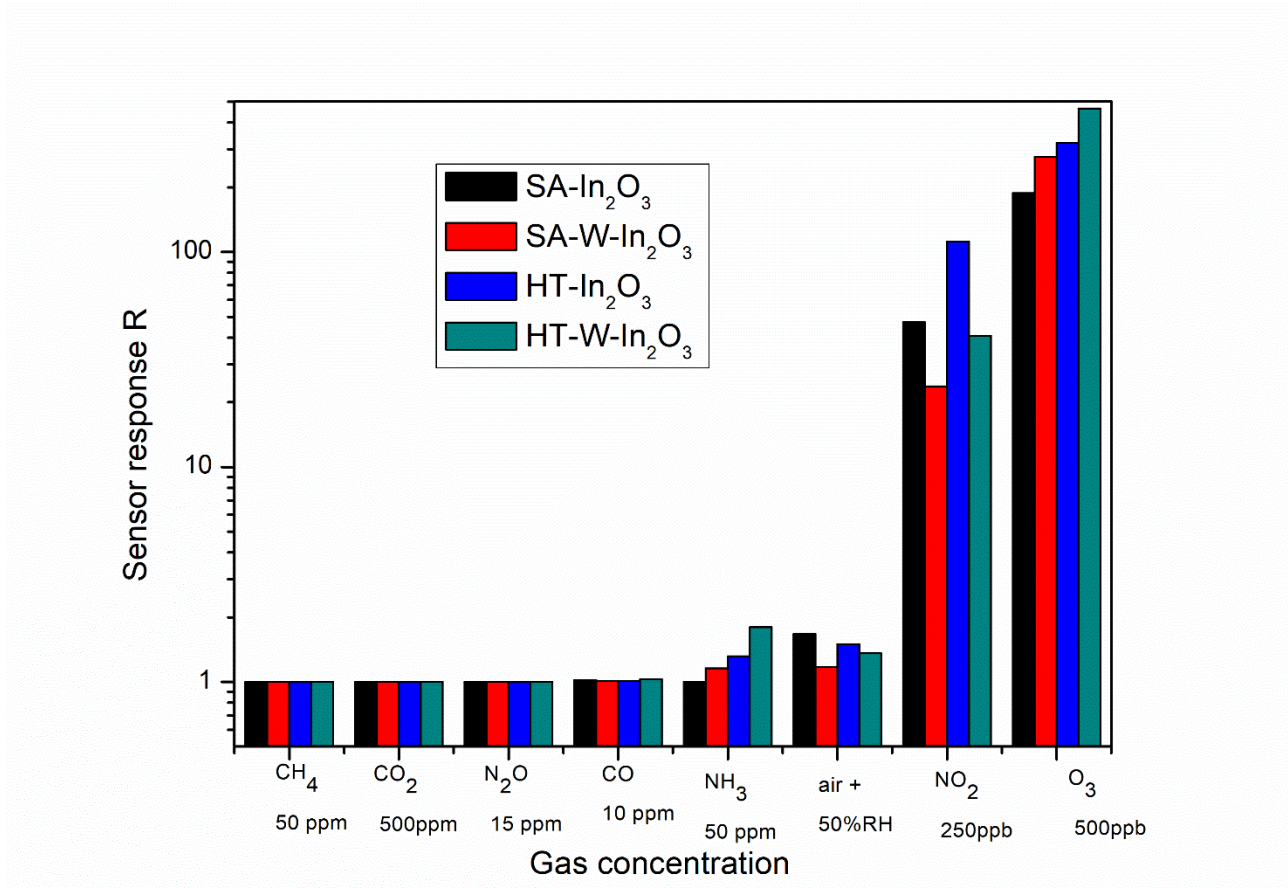


Fig. 15. Cross-sensitivity measurements for SA-In₂O₃, SA-W-In₂O₃, HT-In₂O₃ and HT-W-In₂O₃ sensor at 100°C.

A slight interference with humidity was observed for all the sensors, as well known from the literature [32] even if, in the case of W-In₂O₃ films, the response was decreased under exposure of water vapor respect to undoped materials. The effect of water molecules was also evaluated for all types of sensors by exposing them towards different values of RH (30%, 50% and 70%), and results are depicted in Fig. 16. The W-doped sensors exhibit a moderate response to humidity respect to the base line impedance of the undoped materials, both for commercial and synthesized indium oxide. Specifically, for HT-W-In₂O₃, no effect of humidity up to 30% was measured respect to a linear correlation between sensor response and humidity amount for the other types of sensors (Fig. 16). In accordance with XPS analysis where the presence of OH groups is decreased for W-doped materials.

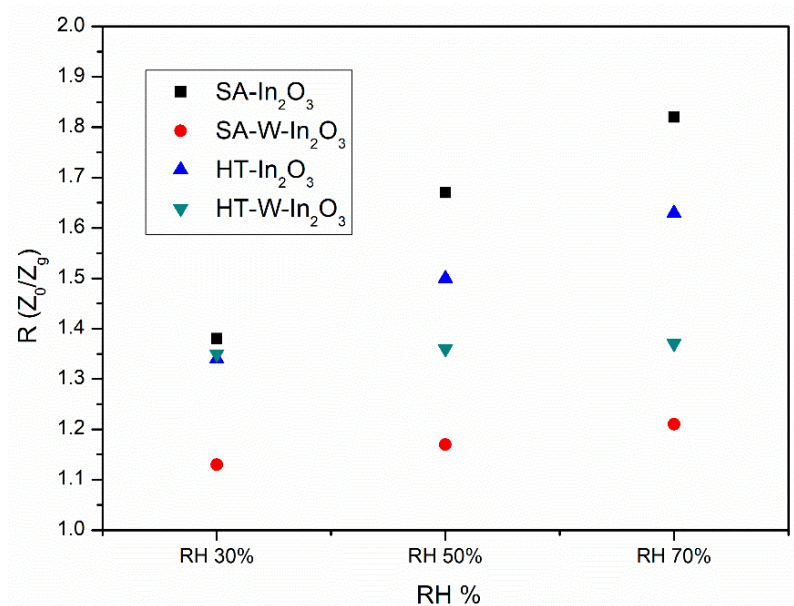


Fig. 16. Humidity effect at 30-50-70% of RH for SA-In₂O₃, SA-W-In₂O₃, HT-In₂O₃ and HT-W-In₂O₃ film at 100°C.

HT-based indium oxide sensors also exhibited a limited response towards ammonia 50 ppm.

Considering oxidizing gases, no cross-sensitivity with carbon dioxide was detected and an expected cross-sensitivity for NO₂ -since the interaction mechanism is comparable with respect to O₃ was evidenced. This interference is decreasing in the case of the doped indium oxide, both SA and HT. In fact, when WO₃ is added to In₂O₃, the selectivity for O₃ appears to be enhanced in terms of humidity and nitrogen dioxide and decreased in terms of ammonia detection. Generally, In₂O₃ sensors are much more sensitive towards oxidant gases respect to reducing ones, in accordance with the literature [31,34]. The difference between results towards O₃ and NO₂ can be described by the different oxidant power of the two gases. Probably, WO₃ can exploit an efficient spillover-effect under ozone exposure (i.e. dissociating it easily) but is not as effective under NO₂ exposure.

Finally, in Table 5, results of the present work are compared with the state of art concerning indium oxide-based sensor for O₃ detection.

Table 5. Some features of In₂O₃ thick film heated ozone sensors. Elaboration from ref. [1].

Technological route	Film thickness	Crystallite size	Max sensor response R: (R_g/R_o)	Conditions of measurements	References
Thick film, drop coating	2 μm	12 nm	300	85°C, 250 ppb, dry	[49]
Thick film, drop coating	/	8 nm	1500	200°C, 100 ppb, dry	[50]
Thick film, screen printing	/	8 nm	100	235°C, 1 ppm	[51]
Thick film, screen printing	20 μm	20 nm	120	270°C, 1ppm	[52]
Thick film, screen printing	/	/	180	330°C, 100 ppb	[53]
Thick film, screen printing	21.4 μm	25.6 nm	464	100°C, 500 ppb, dry	This work

Comparing our results with those of other studies based on indium oxide thick-films, maximum response is ordinarily achieved in the 200°-350°C temperature range. Only Starke et al. [49] obtained the maximum response at 85°C, a comparable working temperature of this work (100°C). Although, the deposition technique was different (drop coating) together with film thickness (2 instead of 20 microns).

Grain size and film thickness are beyond the shadow of any doubt the main parameters responsible for sensor's performance. According to Gardon et al. [25], at lower temperature the gas penetration profile is higher for thick devices, allowing a sharply availability to inner grains for gas molecules. So, activation energy is lower for thick film-based metal oxide sensors because of heating of gas

molecules upon diffusion through the metal oxide. For this reason, thick film-based gas sensors often exhibit an increased response at lower temperature in comparison with thin film technology.

The gas-sensing mechanism of In_2O_3 -based sensors belongs mainly to the surface-controlled type at temperature lower than 100°C [54], and from [55] is known that in the temperature range 100 - 200°C , the sensing mechanism is governed both for surface and bulk effects.

When indium oxide-based sensors are exposed to the ozone, the gas reacts with the oxygen vacancies, that are more concentrated in the $\text{W-In}_2\text{O}_3$ materials compared to the reference indium oxide, as clarified in XPS investigation. Electrons are captured from the conductance band resulting in an increase in the film impedance and resistance. When the metal oxide is exposed to air again, sensors recover quickly to the initial electronic structure despite of the low operating temperature and the thickness of the film in the range of $20\ \mu\text{m}$.

The chemisorbed oxygen ions of the metal oxide enhance the ozone decomposition reaction on the sensor surface resulting in a higher sensor response towards ozone.

O_3 reacts with oxygen vacancies in accordance with equation 5, increasing the impedance of the In_2O_3 and $\text{W-In}_2\text{O}_3$ sensors, and continues up to a certain optimum temperature, beyond which the exothermic gas adsorption becomes more difficult and the gas molecules start to desorb in large amounts, leading to an important drop in the sensor response after 150°C (Figure 11). The enhancement of O_3 -sensing performance of the doped indium oxide sensors can be attributed to the synergistic effect of the WO_3 and In_2O_3 nanoparticles. In addition, the configuration of WO_3 largely situated on the surface of In_2O_3 prevents the agglomeration of the WO_3 improving efficient paths for diffusion and adsorption of the target gas molecules. As a result, the hetero-junctions at the interface of WO_3 and In_2O_3 generate a special electron donor–acceptor system. Upon exposure to oxidant O_3 gas, the impedance of $\text{W-In}_2\text{O}_3$ increases, and more electrons migrate to accelerate the formation of electron depletion regions improving the gas-sensing performance. At the end, the synergistic effect of the In_2O_3 and WO_3 species with different dimensions are essential factors to improve the low-temperature gas sensing performance of the WO_3 -based materials.

Experimental results obtained in the present work indicate that the sensing properties depend on the chemical composition of the sensor, on the specific surface area and on the crystallite size of the semiconductor. Different tungsten trioxide concentrations were investigated, and in accordance with [56] with a WO_3 -doping of 3 at%, a concentration close to 5 wt% WO_3 investigated in this work, a minimum of resistivity together with a maximum carrier mobility is reached among a wide range of WO_3 doping concentration onto indium oxide film.

By increasing the amount of oxygen vacancies in metal oxide, more electrons are available for the material, increasing the n-type characteristics. This would shift the Fermi level closer to the conduction band shifting also the valance band upward. Furthermore, the electron affinity of the material will also increase because more electrons are added to In_2O_3 from WO_3 resulting in a higher electron affinity after the creation of oxygen vacancies.

The mechanism of O_3 adsorption involves both the crystallite and the agglomerates, and in the case of HT- In_2O_3 based sensors a decrease of both parameters was achieved improving noticeably the sensor response for O_3 detection [57].

4. Conclusions

This work has confirmed the exploitation of 2.5 wt% WO_3 - In_2O_3 as sensitive material for ozone detection at sub-ppm level. W^{6+} ions create adsorption centers with higher affinity for oxygen adsorption, resulting in a higher sensitivity of indium oxide for a strong oxidant gas as ozone. Both response and recovery times of the sensor were reasonably fast (in the order of few minutes). The gas sensing behavior towards ozone of indium oxide nanoparticles synthesized by hydrothermal method with a capping agent (CTAB) with lower crystallite size and with a lower degree of agglomeration, together with an enhanced specific surface area, was improved respect to the commercial powder in terms of optimum operating temperature, sensor response and cross sensitivity. Moreover, impregnation of this as-prepared nano-powder with WO_3 at 2.5 wt% results in a partial solid solution formation with WO_3 laying also on the surface. Probably, WO_3 could promote

the formation of Schottky junctions at microstructural level with In_2O_3 . This would lead to an electron transfer from WO_3 to In_2O_3 , decreasing the energy required for oxygen vacancies creation in the lattice. An efficient dissociative chemisorption of oxygen is promoted by WO_3 on the surface, followed by a spillover effect that is an effective path for refilling the oxygen vacancies. This leads to indium oxide-based sensors with higher sensitivity and faster response [58]. The baseline resistance and impedance of W-doped sensors is lower than the undoped ones, confirming the presence of additional electrons, which have to be introduced into the oxide lattice by oxygen vacancies formation or interstitial metal atoms ionization in order to maintain the overall neutrality of the cubic In_2O_3 crystal.

Comparing the sensor response of commercial and synthesized indium oxide, the sensor response of In_2O_3 -based thick film (20 μm) towards a strong oxidant like O_3 seems to be influenced by both the crystallite size and size of agglomerates. According to numerous studies in gas sensors based on strongly agglomerated materials, not only the grain size, but also the size and the gas penetrability of agglomerates for detecting gas are fundamental parameters, controlling either the sensor response and its response kinetics [34, 59, 60]. Experiment proves that the film agglomeration, its thickness and gas penetrability often are essential parameters controlling operating characteristics of ozone sensors. Thus, a high degree of agglomeration favors the formation of “capsulated zones,” with closed porosity. As a result, properties of the sensing material in these zones do not depend on the surrounding gas concentration. Therefore, for agglomerated materials, in thick film type sensors, it is necessary to control primarily the size of agglomerates, and the results of laser granulometry confirm the improvement from SA- In_2O_3 to HT- In_2O_3 powders. XRD investigation assesses also that crystallite size is lower for HT- In_2O_3 compared to SA- In_2O_3 and that WO_3 slightly modifies the lattice parameter a of the cubic In_2O_3 structure.

Acknowledgements

The Authors are grateful to Mr. Mauro Raimondo for FESEM observations, Dr. Maria Carmen Valsania for TEM observations, Dr. Carlotta Pontremoli for N₂ adsorption measurements and Dr. Salvatore Guastella for XPS analysis.

Abbreviations

SA-In₂O₃	SA-W-In₂O₃	HT-In₂O₃	HT-W-In₂O₃
Indium oxide Sigma Aldrich	Indium oxide Sigma Aldrich doped with 2.5 wt.% of WO ₃	Indium oxide hydrothermally synthesized	Indium oxide hydrothermally synthesized doped with 2.5 wt.% of WO ₃

References

- [1] G. Korotcenkov, V. Brinzari, B. K. Cho, In₂O₃ - and SnO₂-based thin film ozone sensors: Fundamentals, Hindawi Publishing Corporation J. Sensors (2016) 1–31. <http://dx.doi.org/10.1155/2016/3816094>.
- [2] R. G. Rice, A. Netzer, Handbook of ozone technology and applications, Ann. Arbor. Science, Mich., USA, 1984.
- [3] P. Siesverda, A review of ozone applications in public aquaria, in Proceedings of the 9th Ozone World Congress (1989) 246–295, NY, USA.

- [4] V. Camel, A. Bermond, The use of ozone and associated oxidation processes in drinking water treatment, *Water Res.* 32 (1998) 3208–3222. [https://doi.org/10.1016/S0043-1354\(98\)00130-4](https://doi.org/10.1016/S0043-1354(98)00130-4).
- [5] <https://www.epa.gov/indoor-air-quality-iaq/ozone-generators-are-sold-air-cleaners>. Accessed 16 September 2019.
- [6] M. D. Rowe, K. M. Novak, P.D. Moskowitz, Health effects of oxidants, *Environ. Int.* 9 (1983) 515–528. [https://doi.org/10.1016/0160-4120\(83\)90008-9](https://doi.org/10.1016/0160-4120(83)90008-9).
- [7] J.A. Bernstein, N. Alexis, C. Barnes, I. L. Bernstein, A. Nel, D. Peden, D. Diaz-Sanchez, S. M. Tarlo, P. B. Williams, Health effects of air pollution, *J. Allergy Clin. Immun.* 114 (2004) 1116–1123. <https://doi.org/10.1016/j.jaci.2004.08.030>.
- [8] <https://www.epa.gov/ozone-pollution/2015-national-ambient-air-quality-standards-naaqs-ozone>. Accessed 16 September 2019.
- [9] M. Ando, C. Swart, E. Pringsheim, V. M. Mirsky, O. S. Wolfbeis, Optical ozone detection by use of polyaniline film, *Solid State Ionics.* 152 (2002) 819–822. [https://doi.org/10.1016/S0167-2738\(02\)00338-7](https://doi.org/10.1016/S0167-2738(02)00338-7).
- [10] R. A. Potyrailo, S. E. Hobbs, G. M. Hieftje, A simple, highly stable scintillator light source for ultraviolet absorption-based sensors, *Anal. Chim. Acta.* 367 (1998) 153–157. [https://doi.org/10.1016/S0003-2670\(98\)00148-2](https://doi.org/10.1016/S0003-2670(98)00148-2).
- [11] C. Eipel, P. Jeroschewski, I. Steinke, Determination of ozone in ambient air with a chemiluminescence reagent film detector, *Anal. Chim. Acta.* 491 (2003) 145–153. [https://doi.org/10.1016/S0003-2670\(03\)00797-9](https://doi.org/10.1016/S0003-2670(03)00797-9).
- [12] T. Takayanagi, P. K. Dasgupta, A chemiluminescence-based continuous flow aqueous ozone analyzer using photoactivated chromotropic acid, *Talanta* 66 (2005) 823–830. <https://doi.org/10.1016/j.talanta.2004.11.036>.

- [13] T. Doll, J. Lechner, I. Eisele, K.-D. Schierbaum, W. Göpel, Ozone detection in the ppb range with work function sensors operating at room temperature, *Sens. Actuators B. Chem.* 34 (1996) 506–510. [https://doi.org/10.1016/S0925-4005\(96\)01941-7](https://doi.org/10.1016/S0925-4005(96)01941-7).
- [14] D. V. Stergiou, T. Stergiopoulos, P. Falaras, M. I. Prodromidis, Solid redox polymer electrolyte-based amperometric sensors for the direct monitoring of ozone in gas phase, *Electrochem. Commun.* 11 (2009) 2113–2116. <https://doi.org/10.1016/j.elecom.2009.09.007>.
- [15] A. Bejaoui, J. Guerin, J.A. Zapien, K. Aguir, Theoretical and experimental study of the response of CuO gas sensor under ozone, *Sens. Actuators B. Chem.* 190 (2014) 8–15. <https://doi.org/10.1016/j.snb.2013.06.084>.
- [16] V. R. Mastelaro, S. C. Zilio, L. F. da Silva, P. I. Pelissari, M. I. B. Bernardi, J. Guerin, K. Aguir, Ozone gas sensor based on nanocrystalline SrTi_{1-x}FexO₃ thin films, *Sens. Actuators B. Chem.* 181 (2013) 919–924. <https://doi.org/10.1016/j.snb.2013.02.068>.
- [17] C. Wang, L. Yin, L. Zhang, D. Xiang, R. Gao, Metal oxide gas sensors- sensitivity and influencing factors, *Sensors.* 10 (2010) 2088-2106. <https://doi.org/10.3390/s100302088>.
- [18] N. Barsan, U. Weimar, Conduction model of metal oxide gas sensors, *J. Electroceram.* 7 (2001) 143–167. <https://doi.org/10.1023/A:1014405811371>.
- [19] G. F. Fine, L.M. Cavanagh, A. Afonja, R. Binions, Metal oxide semi-conductor gas sensors in environmental monitoring, *Sensors.* 10 (2010) 5469–5502. <https://doi.org/10.3390/s100605469>.
- [20] A. Berna, Metal oxide sensors for electronic noses and their application to food analysis, *Sensors.* 10 (2010) 3882–3910. <https://doi.org/10.3390/s100403882>.
- [21] K. Wetchakun, T. Samerjai, N. Tamaekong, C. Liewhiran, C. Siriwong, V. Kruefu, A. Wisitsoraat, A. Tuantranont, S. Phanichphant, Semiconducting metal oxides as sensors for environmentally hazardous gases, *Sens. Actuators B. Chem.* 160 (2011) 580–591. <https://doi.org/10.1016/j.snb.2011.08.032>.

- [22] G. Korotcenkov, Gas response control through structural and chemical modification of metal oxide films: state of the art and approaches, *Sens. Actuators B. Chem.* 107 (2005) 209–232. <https://doi.org/10.1016/j.snb.2004.10.006>.
- [23] G. Eranna, B. C. Joshi, D. P. Runthala, R. P. Gupta, Oxide materials for development of integrated gas sensors—a comprehensive review, *Crit. Rev. Solid State Mater. Sci.* 29 (2004) 111–188. <https://doi.org/10.1080/10408430490888977>.
- [24] G. Korotcenkov, B. K. Cho, Thin film SnO₂-based gas sensors: film thickness influence, *Sens. Actuators B. Chem.* 142 (2009) 321–330. <https://doi.org/10.1016/j.snb.2009.08.006>.
- [25] M. Gardon, J. M. Guilemany, A review on fabrication, sensing mechanism and performance of metal oxide gas sensors, *J. Mater. Sci-Mater. El.* 24 (2013) 1410-1421. <https://doi.org/10.1007/s10854-012-0974-4>.
- [26] M. Z. Atashbar, B. Gong, H. T. Sun, W. Wlodarski, R. Lamb, Investigation on ozone-sensitive In₂O₃ thin films, *Thin Solid Films.* 354 (1999) 222–226. [https://doi.org/10.1016/S0040-6090\(99\)00405-8](https://doi.org/10.1016/S0040-6090(99)00405-8).
- [27] X. Xu, X. Mei, P. Zhao, P. Sun, Y. Sun, X. Hu, G. Lu, One-step synthesis and gas sensing characteristics of urchin-like In₂O₃, *Sens. Actuators B. Chem.* 186 (2013) 61–66. <https://doi.org/10.1016/j.snb.2013.05.029>.
- [28] T. Wagner, J. Hennemann, C.-D. Kohl, M. Tiemann, Photocatalytic ozone sensor based on mesoporous indium oxide: influence of the relative humidity on the sensing performance, *Thin Solid Films.* 520 (2011) 918–921. <https://doi.org/10.1016/j.tsf.2011.04.181>.
- [29] G. Sberveglieri, C. Baratto, E. Comini, G. Faglia, M. Ferroni, A. Ponzoni, A. Vomiero, Synthesis and characterization of semiconducting nanowires for gas sensing, *Sens. Actuators B. Chem.* 121 (2007) 208–213. <https://doi.org/10.1016/j.snb.2006.09.049>.
- [30] T. K. H. Starke, G. S. V. Coles, High sensitivity ozone sensors for environmental monitoring produced using laser ablated nanocrystalline metal oxides, *IEEE Sens. J.* 2 (2002) 14–19. <https://doi.org/10.1109/7361.987056>.

- [31] M. Ivanovskaya, A. Gurlo, P. Bogdanov, Mechanism of O₃ and NO₂ detection and selectivity of In₂O₃ sensors, *Sens Actuators B. Chem.* 77 (2001) 264–267. [https://doi.org/10.1016/S0925-4005\(01\)00708-0](https://doi.org/10.1016/S0925-4005(01)00708-0).
- [32] G. Korotcenkov, Metal oxide composites in conductometric gas sensors: achievements and challenges, *Sens Actuators B. Chem.* 244 (2017) 182–210. <https://doi.org/10.1016/j.snb.2016.12.117>.
- [33] J. Ollitrault, N. Martin, J.Y. Rauch, J.B. Sanchez, F. Berger, Improvement of ozone detection with GLAD WO₃ films, *Mater. Lett.* 155 (2015) 1–3. <https://doi.org/10.1016/j.matlet.2015.04.099>.
- [34] G. Korotcenkov, V. Brinzari, B. K. Cho, In₂O₃ - and SnO₂- based ozone sensors: design and characterization, *Crit. Rev. Solid State Mater. Sci.* 43 (2018) 83–132. <https://doi.org/10.1080/10408436.2017.1287661>.
- [35] T. Yan, X. Wang, J. Long, P. Liu, X. Fu, G. Zhang, X. Fu, Urea-based hydrothermal growth, optical and photocatalytic properties of single-crystalline In(OH)₃ nanocubes, *J. Colloid Interface Sci.* 325 (2008) 425–431. <https://doi.org/10.1016/j.jcis.2008.05.065>.
- [36] D. V. Shinde, D. Y. Ahn, V. V. Jadhav, D. Y. Lee, N. K. Shrestha, J. K. Lee, Hwa Y. Lee, R. S. Maneb, S. H. Han, Coordination chemistry approach for shape-controlled synthesis of indium oxide nanostructures and their photoelectrochemical properties, *J. Mater. Chem A.* 2 (2014) 5490–5498. <https://doi.org/10.1039/C3TA15407F>.
- [37] https://www.sigmaaldrich.com/Graphics/COfAInfo/SigmaSAPQM/SPEC/63/632317/632317-BULK_____ALDRICH__.pdf. Accessed 16 September 2019.
- [38] D. Ziegler, A. Marchisio, P. Palmero, J.-M. Tulliani, WO₃-doped indium oxide thick films for ozone detection at low temperature, *Proceedings.* 1 (2017) 428. <https://doi.org/10.3390/proceedings1040428>.
- [39] W. H. Ho, S. K. Yen, Preparation and characterization of indium oxide film by electrochemical deposition, *Thin Solid Films.* 498 (2006) 80–84. <https://doi.org/10.1016/j.tsf.2005.07.072>.

- [40] J.-L. Cao, Z.-L. Yan, Y. Wang, G. Sun, X.-D. Wang, H. Bala, Z.-Y. Zhang, CTAB-assisted synthesis of mesoporous CoFe₂O₄ with high carbon monoxide oxidation activity, *Mater. Lett.* 106 (2013) 322–325. <https://doi.org/10.1016/j.matlet.2013.05.054>.
- [41] M. M. Bagheri-Mohagheghi, N. Shahtahmasebi, E. Mozafari, M. Shokooh-Saremi, Effect of the synthesis route on the structural properties and shape of the indium oxide (In₂O₃) nano-particles, *Physica E Low Dimens. Syst. Nanostruct.* 41 (2009) 1757–1762. <https://doi.org/10.1016/j.physe.2009.06.009>.
- [42] <http://abulafia.mt.ic.ac.uk/shannon/radius>. Accessed 16 September 2019.
- [43] R.D. Shannon, Revised effective ionic radii and systematic studies of interatomic distances in halides and chalcogenides, *Acta Cryst.* A32 (1976) 751–767. <https://doi.org/10.1107/S0567739476001551>.
- [44] <https://xpssimplified.com/elements/indium.php>. Accessed 16 September 2019.
- [45] Y.D. Zhang, G.C. Jiang, K.W. Wong, Z. Zhen, Green synthesis of indium oxide hollow spheres with specific sensing activities for flammable organic vapors, *Sensor Letters.* 8 (2010) 355–361. <https://doi.org/10.1166/sl.2010.1277>.
- [46] T. Zhang, F. Gu, D. Han, Z. Wang, G. Guo, Synthesis, characterization and alcohol-sensing properties of rare earth doped In₂O₃ hollow spheres, *Sens. Actuators B. Chem.* 177 (2013) 1180–1188. <https://doi.org/10.1016/j.snb.2012.12.024>.
- [47] <https://xpssimplified.com/elements/tungsten.php>. Accessed 16 September 2019.
- [48] Ch. Y. Wang, V. Cimalla, C.-C. Roehlig, A new type of highly sensitive portable ozone sensor operating at room temperature, in *Proceedings of the 5th IEEE Conference on Sensors*, 81–84, EXCO, Daegu, South Korea, 2006.
- [49] T. K. H. Starke, G. S. V. Coles, High sensitivity ozone sensors for environmental monitoring produced using laser ablated nanocrystalline metal oxides, *IEEE Sensors Journal.* 2 (2002) 14–19. <https://doi.org/10.1109/7361.987056>.

- [50] M. Epifani, E. Comini, J. Arbiol, R. Díaz, N. Sergent, T. Pagnier, P. Siciliano, G. Faglia, J. R. Morante, Chemical synthesis of In₂O₃ nanocrystals and their application in highly performing ozone-sensing devices, *Sens. Actuators B. Chem.* 130 (2008) 483–487. <https://doi.org/10.1016/j.snb.2007.09.025>.
- [51] T. Sahm, A. Gurlo, N. Barsan, U. Weimar, Properties of indium oxide semiconducting sensors deposited by different techniques, *Particul. Sci. Technol.* 24 (2006) 441–452. <https://doi.org/10.1080/02726350600934739>
- [52] A. Oprea, A. Gurlo, N. Bârsan, U. Weimar, Transport and gas sensing properties of In₂O₃ nanocrystalline thick films: a Hall effect based approach, *Sens. Actuators B. Chem.* 139 (2009) 322–328. <https://doi.org/10.1016/j.snb.2009.03.002>.
- [53] S. R. Kim, H. K. Hong, C. H. Kwon, D. H. Yun, K. Lee, Y. K. Sung, Ozone sensing properties of In₂O₃-based semiconductor thick films, *Sens. Actuators B. Chem.* 66 (2000) 59–62. [https://doi.org/10.1016/S0925-4005\(99\)00468-2](https://doi.org/10.1016/S0925-4005(99)00468-2).
- [54] Y. D. Zhang, Z. Zheng, F.L. Yang, Highly sensitive and selective alcohol sensors based on Ag-doped In₂O₃ coating, *Ind. Eng. Chem. Res.* 49 (2010) 3539–3543. <https://doi.org/10.1021/ie100197b>.
- [55] G. Neri, A. Bonavita, G. Micali, G. Rizzo, N. Pinna, M. Niederberger, In₂O₃ and Pt-In₂O₃ nanopowders for low temperature oxygen sensors, *Sens. Actuators B. Chem.* 127 (2007) 455–462. <https://doi.org/10.1016/j.snb.2007.04.046>.
- [56] S. K. Vishwanath, T. An, W. Jin, J. Kang and J. Kim, The optoelectronic properties of tungsten-doped indium oxide thin films prepared by polymer-assisted solution processing for use in organic solar cells, *J. Mater. Chem. C.* 5 (2017) 10295–10301. <https://doi.org/10.1039/C7TC03662K>.
- [57] G. Korotcenkov, V. Brinzari, A. Cerneavski, The influence of film structure on In₂O₃ gas response, *Thin Solid Films.* 460 (2004) 315–323. <https://doi.org/10.1016/j.tsf.2004.02.018>.
- [58] N. Yamazoe, Toward innovations of gas sensor technology, *Sens. Actuators B. Chem.* 108 (2005) 2–14. <https://doi.org/10.1016/j.snb.2004.12.075>.

[59] G. Korotcenkov, The role of morphology and crystallographic structure of metal oxides in response of conductometric-type gas sensors, *Mater. Sci. Eng. R.* 61 (2008) 1–39. <https://doi.org/10.1016/j.mser.2008.02.001>.

[60] J. F. Mc Aleer, P. T. Moseley, J. O. Norris, and D. E. Williams, Tin dioxide gas sensors. Part 1.—Aspects of the surface chemistry revealed by electrical conductance variations, *J. Chem. Soc. Faraday Trans. I* 83 (1987) 1323–1346. <https://doi.org/10.1039/F19878301323>.

Declaration of interests

The authors declare that they have no known competing financial interests or personal relationships that could have appeared to influence the work reported in this paper.

The authors declare the following financial interests/personal relationships which may be considered as potential competing interests:

Authors statements:

J.M. Tulliani: Conceptualization. P. Palmero, J.M. Tulliani: Methodology. D. Ziegler: Investigation. P. Palmero, J.M. Tulliani: Resources. D. Ziegler: Writing- Original draft preparation. P. Palmero, J.M. Tulliani: Supervision. P. Palmero, J.M. Tulliani, D; Ziegler: Writing- Reviewing and Editing,

W-doped indium oxide synthesized via hydrothermal route for low-temperature ozone sensing

Daniele Ziegler¹, Paola Palmero¹, Jean-Marc Tulliani^{1*}

¹Politecnico di Torino, Department of Applied Science and Technology, INSTM R.U
PoliTO-LINCE Laboratory, Corso Duca degli Abruzzi, 24, 10129 Torino, Italy

*Corresponding author: Tel: +39-011-0904700; E-mail address: jeanmarc.tulliani@polito.it

Abstract

Nano-crystalline indium oxide and tungsten-doped indium oxide were prepared by hydrothermal route and adopted as ozone sensitive material at low temperature, comparing their performances with a commercial indium oxide. After hydrothermal synthesis, powders were calcined at 400°C for 30 minutes and characterized by laser granulometry, thermal analysis, X-ray diffraction, N₂ adsorption, X-ray Photoelectron Spectroscopy, field emission scanning electron microscopy, and transmission electron microscopy. Sensors were developed by screen-printing the sensing material onto α -alumina substrates with platinum interdigitated electrodes. After drying overnight, sensors were fired at 600°C for 1 h in air.

The sensor response was measured in the range 25°C – 200°C carrying on all measurements in a flow chamber at a constant flow rate of 1 L/min of dry air in the range 200 – 500 ppb O₃. Response time and recovery time (e.g., the times taken for the sensor to attain 90% of total impedance change from its initial impedance value) were detected, together with cross-sensitivity tests towards NH₃, CH₄, humidity, CO, NO₂, CO₂ and N₂O.

Sensor's response (R) was defined as the ratio between impedance of the film under gas exposure at the equilibrium and the impedance under dry air. Best results were obtained at 100°C, with R equal to 464 under 500 ppb O₃. These results are extremely encouraging and support the exploitation of tungsten-doped indium oxide as low-temperature ozone sensors.

Highlights

- Nanocrystalline In₂O₃ and W-doped In₂O₃ powders were prepared by hydrothermal route
- WO₃ slightly modifies the lattice parameter a of the cubic In₂O₃ structure
- Ozone sensing properties of sensors were studied in the range 200 - 500 ppb O₃
- Best results were obtained at an operating temperature as low as 100°C
- Sensor response/recovery time are quite short in the studied O₃ concentration range

Keywords: indium oxide; tungsten-doped indium oxide; hydrothermal synthesis; impregnation; ozone detection.

1. Introduction

O₃ is one of the most reactive form of oxygen, and it is generated in the troposphere after a chain of photo-chemical reactions between sunlight, hydrocarbon and nitrogen oxides gases. Recently, ozone concentration in the lowest level of atmosphere has enhanced as a consequence of the interaction between sunlight and a wide range of chemicals emitted in the troposphere by anthropogenic activities, like vehicles and industries. In addition, tropospheric ozone is a byproduct of industrial and urban pollution [1].

Nowadays ecologically clean ozone technologies are spreading their interest: it is well known that O₃ can be widely used in medicine, as well as in different technological processes [2–4]. Despite its

use in processes as water depuration and purification of gases, ozone is hazardous to the human health, especially for the respiratory system. In fact, ozone may worsen chronic respiratory diseases such as asthma, compromising the ability of the body to fight against respiratory infections [5].

As a result, ozone intoxications cause inflammation and congestion of the respiratory apparatus [6–7]. For this reason, monitoring ozone concentration at ground level appears of the highest importance. In 2015, EPA (United States Environmental Protection Agency) revised the National Ambient Air Quality Standards (NAAQS) for ground-level ozone not to exceed 70 ppb, with the goal to improve public health protection [8].

In this frame, the analytical techniques developed to monitor ozone concentration should work in a quite wide range of concentration (0.01-10 ppm) [1]. Ozone sensor with detection limit (LOD) in the sub-ppm level should be applied in environmental monitoring, while in industrial and commercial applications the expected concentrations are commonly in the order of some ppm.

Nowadays, a wide range of sensing technologies have been developed for measuring ozone concentration at ground level, such as optical detection [9], ultraviolet (UV) light absorption [10] chemiluminescence analyzers [11], fluorescence measurements [12], potassium iodide [13], direct amperometry determination [14], and gas-sensitive semiconductors [15-16].

Among all these techniques, the latter evidences a great potential, compared with traditional ozone measurements methods, because of semiconductors' low cost, ease of operation, high long-term reliability and stability together with a relatively moderate power dissipation [1].

Traditionally, the conduction mechanism of semiconducting metal oxide (SMO) is explained by gas-related modulation of Schottky barriers resulting in space-charge layers at grain boundaries of n-type semiconducting oxides [17-19]. This is true for the most investigated materials: SnO₂, ZnO, WO₃ and In₂O₃ [19-23]. Nonetheless, the temperature of maximum sensor response depends mainly on the grain size and film thickness [24, 25].

Responses in the range 10²-10³ in the ppm range of ozone concentration appear to be the optimal for ozone sensors market [1]. Indium oxide nanostructures with various morphology have been

extensively used to detect ozone [26-29]. However, only few papers report a maximum response to ozone in a temperature range below 100°C [30-31], without a UV illumination. In order to improve the sensing features towards ozone of indium oxide films, many studies have assessed the efficiency of doping with metal oxides such as Ga₂O₃, Fe₂O₃, CeO₂, ZrO₂, NiO, ZnO and SnO₂ [32]. WO₃, a n-type ozone sensitive oxide [33], improves sensitivity of the metal oxide film, creating adsorption centers with an enhanced affinity for oxygen species, since unusual valence states (W⁶⁺) are produced [34]. Many experiments have assessed that bulk-doping of semiconductor metal oxides is an efficient method to increase sensor response, modifying the surface reactivity and the bulk electrophysical features, defect chemistry and porosity of the matrix.

In this research, a commercial indium oxide nano-powder supplied by Sigma-Aldrich (SA-In₂O₃) was selected as reference sensing material for ozone detection in sub-ppm concentration range, and its sensing properties were compared with 1, 2.5 and 5 wt% of WO₃-doped In₂O₃ sensors realized via impregnation method. In₂O₃ was additionally synthesized via hydrothermal route for decreasing the crystallite size as well as, improving the sensitivity and the response and recovery times towards O₃. Finally, sensors prepared at the optimal WO₃ concentration, were tested at the optimum operating temperature and their performances were compared to those of the commercial and the synthesized In₂O₃ sensors.

2. Experimental

2.1. Powder synthesis

In₂O₃ powder was synthesized by hydrothermal route and referred to as HT-In₂O₃. To perform the synthesis, analytical grade reagents were used without further purification: indium (III) nitrate pentahydrate (In(NO₃)₃·5H₂O, 99.99%, metal basis, Alfa Aesar), hexadecyltrimethylammonium bromide (CTAB, ≥ 99.8%, Sigma Aldrich) used as a capping agent and sodium hydroxide (ACS > 98% pellets, Sigma Aldrich) used as a mineralizer. Following previous literature [35], the In(NO₃)₃·5H₂O: CTAB: NaOH molar ratio of 1:1.96:3 was used. The role of CTAB to confer stability to nanoparticles during crystal growth and control of their morphologies, size and shape has been already demonstrated in

literature [35]. Sodium hydroxide has been chosen as mineralizer, as it induces a smaller crystallite size of the wet-synthesized product as compared to other agents, like urea [35].

After dissolution in distilled water of all the reagents, the solution was stirred at room temperature for 30 min. It was then transferred into a Teflon-autoclave and kept at 70°C for 24 h and then at 120°C for 12 h, providing a white powder.

The precipitate was washed several times with distilled water and twice in absolute ethanol in order to eliminate the synthesis by-products, and finally dried at 70°C overnight. The powder was finally calcined at 400°C for 30 min, to induce the crystallization of In_2O_3 [36]. After the annealing procedure, the color of the product varied from white to pale yellow, denoting the formation of the In_2O_3 phase from $\text{In}(\text{OH})_3$ [36].

A commercial In_2O_3 powder, supplied by Sigma-Aldrich (SA- In_2O_3), was also used as reference material. According to the supplier [37], this powder is characterized by 99.9% purity and particle size < 100 nm, as determined by TEM analysis.

Both SA- In_2O_3 and HT- In_2O_3 powders were doped with WO_3 by impregnation method [38]. WCl_6 (\geq 99.9% trace metals basis, Sigma Aldrich) was dispersed in dichloromethane (ACS, \geq 99.8%, ChemLab) before addition of the powders. The suspensions were stirred for 3 h at room temperature and dried at 40°C. To eliminate the chloride by-product, the powders were washed twice by centrifugation in water. In the case of SA- In_2O_3 , impregnation was carried out by using three different amounts of WCl_6 to obtain 1, 2.5 and 5 wt% of WO_3 -doped In_2O_3 powders. HT- In_2O_3 powder was doped at the optimal WO_3 concentration (2.5 wt%) determined for the commercial powder [38]. Thus, from now, when tungsten trioxide content is not mentioned, doped samples contain 2.5 wt% of WO_3 .

After drying at 80°C overnight, the powders were annealed at 400°C for 3 hours with a heating rate of 2°C/min, resulting in tungsten trioxide-doped indium oxide (SA-W- In_2O_3 and HT-W- In_2O_3) products.

2.2. Powder and film characterization

The particle size distribution of doped and undoped powders were determined by laser granulometry (Mastersizer 3000, Malvern, Worcestershire, UK) on alcoholic suspension dispersed under sonication for 5 minutes.

Differential Thermal Analysis-Termogravimetry (DTA-TG, STA 409, Netzsch, Selb, Germany) was performed on HT-In₂O₃ precursor up to 400°C (heating rate of 10°C/min) under static air.

X-Ray diffraction (XRD) was carried out on SA and HT doped and undoped powders. In addition, the same analysis was carried out after the addition of quartz as an internal standard, to evaluate possible shifts in the diffraction pattern after doping. Spectra were recorded on a Pan'Analytical X'Pert Pro instrument (Pan'Analytical, Almelo, The Netherlands) with Cu K radiation (0.154056 nm) in the range between 5 and 70° 2θ, working with a step size of 0.0065° of 2θ and an acquisition time per step equal to 23 s. Diffraction patterns were indexed by means of the Powder Data File database (P.D.F. 2000, International Centre of Diffraction Data, Newtown Square, PA, USA).

The average crystallite size was estimated according to the Scherrer equation, for a qualitative comparison with the available data in literature (1):

$$D = k\lambda / \beta \cos\theta \quad (1)$$

where k is a constant assumed to be equal to 0.9, λ is the Cu K α wavelength (0.154056 nm), θ is the half of Bragg (radiants) and β is the full width at half maximum of the X-ray diffraction peaks, that are commonly associated with the crystallite size, presence of defects, and peak broadening caused by the instrument [39].

Cell parameters for cubic In₂O₃ phase were calculated for the three principal planes (222) (400) and (440), using the following equation based on XRD data (2):

$$d_{hkl} = \frac{a}{\sqrt{h^2 + k^2 + l^2}} \quad (2)$$

where d_{hkl} is the lattice spacing of the (hkl) plane and a is the lattice spacing.

Nitrogen adsorption and desorption isotherms were determined with an ASAP2020, Micromeritics ASAP 2020 Plus Physisorption (Norcross, GA, USA), at the temperature of -196°C. Before nitrogen adsorption–desorption investigations, each sample was degassed at 150°C for 8 h. Moreover, Brunauer–Emmett–Teller (BET) model was applied to determine the specific surface areas of the samples.

X-ray Photoelectron Spectroscopy (XPS) was carried out with a PHI 5000 Versaprobe (Physical Electronics, Chanhassen, MN, USA) (monochromatic Al K α X-ray source with 1486.6 eV energy, 15 kV voltage, and 1 mA anode current) to investigate the surface chemical composition of the semiconductor together with possible In and O shifts after doping.

Moreover, morphologies of powders and films were examined by means of a FESEM (Zeiss Supra-40, Oberkochen, Germany), [also in cross-section to evaluate the film thickness. FESEM was](#) equipped with an Oxford Energy Dispersive X-ray detector. Observations were performed on Cr coated specimens. Finally, observations and chemical analysis of the samples were carried out by HR-TEM coupled with energy dispersive X-ray spectroscopy (TEM-EDS). Investigations were performed with a JEOL 3010-UHR (Peabody, MA, USA) instrument, working with an acceleration potential of 300 kV and equipped with an Oxford Inca Energy TEM 200 EDS X-rays analyzer. Quantitative compositional studies were carried out using the Oxford INCA Microanalysis Suite software, and the mean elemental composition resulted from the average of 5 measurements performed in different regions.

2.3 Fabrication and measurement of gas sensors

Sensors were realized by screen-printing technique onto α -alumina substrates (Coors Tek, Golden, CO, USA, ADS-96, 96% alumina, 0.85 cm x 1.7 cm) with platinum interdigitated electrodes (5545-LS, ESL, King of Prussia, PA, USA) over the ceramic substrate. These electrodes were fired at 980°C (2°C/min heating and cooling ramps) for 18 minutes resulting in a high-grade adhesion and optimizing their electrical conductivity at the same time, according to the manufacturer's

recommendations. FESEM observations showed that electrodes have 400 μm in width and are spaced 450 μm each other. Their thickness is about 6 μm .

Inks for screen printing were realized by mixing the materials with an organic vehicle (ethylene glycol monobutyl ether, Emflow, Emca Remex, USA), to achieve the proper rheological characteristics with the right viscosity, and polyvinyl butyral (PVB, Sigma Aldrich) that acts as temporary binder for the powder before thermal treatment. The ink was sonicated for 5 min in an ultrasonic bath to disperse the sensing material and to dissolve the PVB in the solvent.

After screen-printing deposition with a 325-mesh steel mask, sensors were dried at 80°C overnight and fired at 400°, 500° and 600°C in air for 1 h (2°C/min heating and cooling ramps). This process is required to remove all the organic residues from the solvent and to ensure the adhesion with the substrate at the same time.

Once fabricated, sensors were tested in a home-made system, where O₃ was generated by a UV lamp (SOG-01, UVP-LLC Cambridge, UK) from a constant air flow of 1000 SCCM (standard cubic centimeters) of compressed air. The modulation of O₃ concentration was realized by varying the length of lamp exposed and was determined by means of the calibration curves given by the manufacturer.

Ozone losses due to adsorption and reactions in pipelines and measuring chamber was prevented by using suitable materials as polytetrafluoroethylene (PTFE) and polyvinylidene fluoride (PVDF) tubes.

First, sensors SA-In₂O₃, SA-W-In₂O₃, HT-In₂O₃ and HT-W-In₂O₃ were tested towards O₃ ~~0.5 ppm~~500 ppb at different temperatures (from room temperature to 200°C, in steps of 25 degrees) to evaluate the optimum working temperature for each sensing material. Different O₃ concentrations were then investigated at the optimum temperature, between 200 and 500 ppb in steps of 100 ppb, and the results were compared with literature. Cross-sensitivity tests were also carried out adopting the same operating conditions described above. Target gas was diluted with dry air by means of flow meters (Teledyne Hastings Instruments HFM 300 controller and flow meters HFC 302, Teledyne Hastings, Hampton, VA, USA). All the sensors were heated by a Ni-Cr wire, located underneath the sensor,

alimented with a DC power supply (Peak Tech, Nanjing, Jiangsu, China). A PT1000 resistance temperature detector (RS Pro, London, UK) was used for temperature determination of sensors.

~~Such~~ ~~e~~ ~~C~~ross-sensitivity measurements were carried out towards both oxidizing and reducing gases. ~~In particular way~~ ~~Specifically~~, the sensitivity towards NH₃ (50 ppm in air), CH₄ (50 ppm in air), CO₂ (500 ppm in air), humidity (30, 50, 70% of relative humidity (RH) at room temperature), NO₂ (250 ppb in air), CO 10 ppm and N₂O (15 ppm in air) was ~~tested~~ ~~investigated~~ under the same flow of 1000 SCCM.

During tests under constant gas flow, film impedance was measured by means of a LCR meter (Hioki 3533-01, Nagano, Japan). Impedance's measurements were carried out by means of a constant AC tension of 1 V at 1 kHz, and sensors were put into a chamber of 0.1 L volume.

The response of the sensor (R) was calculated according to equation (3) for oxidizing gases and to equation (4) for reducing analytes:

$$R: Z_g/Z_0 \quad (3)$$

$$R: Z_0/Z_g \quad (4)$$

Where Z_g and Z_0 are respectively the impedances under target gas and the starting (under dry air flow) of the oxide layer at the equilibrium.

The response times (the time needed by a sensor to achieve 90% of the total impedance change in the case of gas adsorption) together with the recovery times (the time necessary to reach 90% of the total impedance variation in the case of gas desorption) were also determined in the present work.

3. Results and discussion

3.1 Powder and film characterization

In Fig. 1, the DTA-TG curves related to HT-In₂O₃ precursor, just dried at 120°C, are depicted. The DTA curve shows a small exothermic peak at 207°C, that can be attributed to the decomposition of

the residual surfactant in the sample [40]. Then, a broad endothermic peak is detected at 317°C, which can be related to the transformation of indium hydroxide into indium oxide. Moreover, TG analysis displays a total weight loss of 14.8% between 270°C and 350°C, with a maximum slope at 305°C. It should be mentioned that the weight loss corresponding to the complete conversion of the indium hydroxide into indium oxide is equal to 16.3% [40], suggesting a not complete crystallization of the oxide phase in the present analysis. On the ground of this result, all powders were annealed at 400°C for 3 h, to achieve a complete conversion.

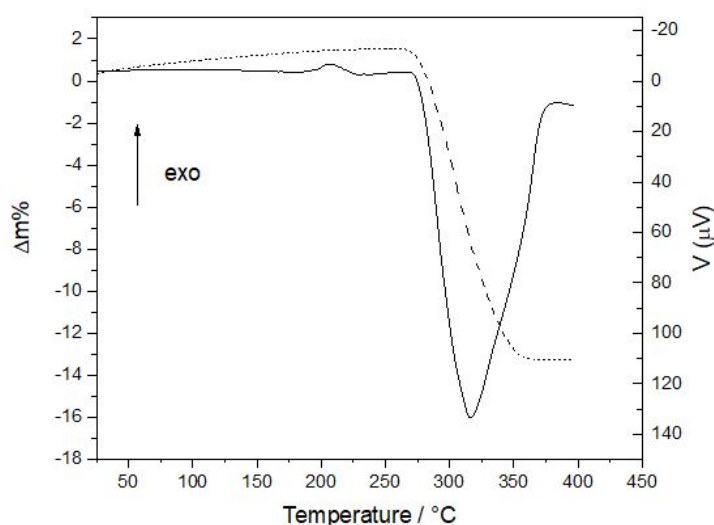


Fig 1. TG-DTA curve of HT-In₂O₃ precursor TG: dashed line; DTA: straight line.

XRD analyses, carried out on powders calcined at 400°C/3h, confirmed the presence of pure cubic indium oxide in the bixbyte type (JCPDF card n°06-0416), as shown in Fig. 2 for doped and undoped SA-In₂O₃ (a) and HT-In₂O₃ (b) powders. Here, no traces of In(OH)₃ phase were detected.

The XRD pattern of HT-powder is characterized by broader peaks as compared to SA-samples, suggesting a smaller crystallite size and a lower degree of crystallization. In fact, by applying the Scherrer equation on the following peaks: (211), (222), (400), (440), (541), a crystallite size equal to 48 ± 3.5 nm was determined for both SA-In₂O₃ and SA-W-In₂O₃. An almost halved value (26 ± 2.8 nm) was found for HT-In₂O₃ and HT-W-In₂O₃ powders. These results are in accordance with a previous work of Bagheri-Mohagheghi [41], showing crystallite size in the range 3-25 nanometers

for hydrothermal synthesized indium oxide powders, and an almost doubled value (10-45 nm) for a sol-gel synthesized powder.

SA-In₂O₃ and SA-W-In₂O₃ powders showed almost superimposable XRD patterns (Fig. 2a) and this is true also for the HT-In₂O₃ and HT-W- In₂O₃ powders (Fig. 2b). Only a small and broad peak at about 24.07° of 2θ was observed in both W-doped powders, and it is associated to the crystallization of the WO₃ phase. Precisely, the band was attributed to the sum of the three main peaks of WO₃ in monoclinic phase (reference n° 43-1035), corresponding to the (002), (020) and (200) crystallographic planes respectively located at 23.12°, 23.59° and 24.38° 2θ. No traces of any other phases besides cubic In₂O₃ and monoclinic WO₃ were detected. It should be specified that the crystallization of WO₃ occurs at temperatures lower than 400°C, as confirmed by XRD analysis carried out on the WCl₆ precursor thermally treated at 400°C for 3 h (XRD pattern in Fig. 2c) resulting in the formation of monoclinic WO₃.

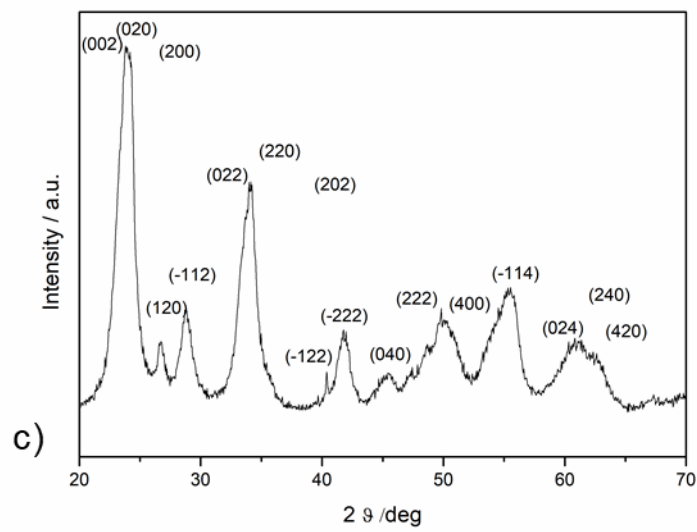
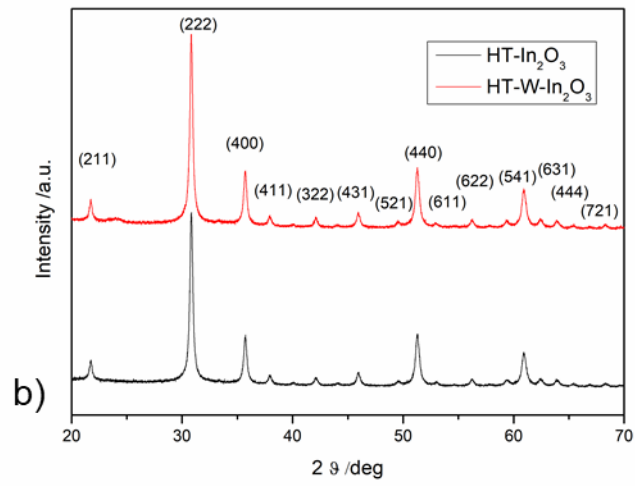
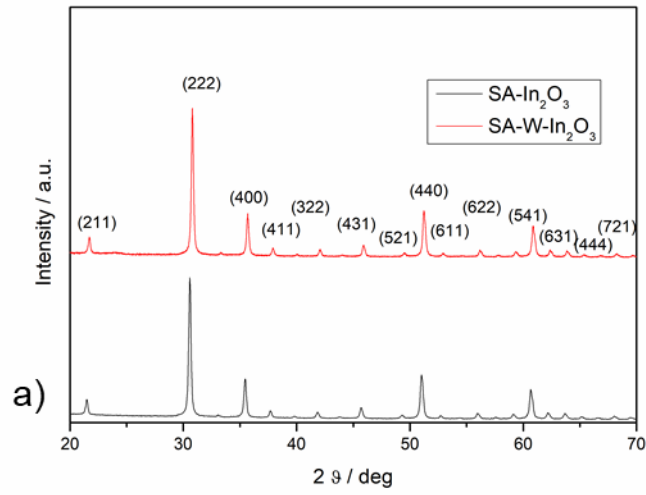


Fig. 2. XRD pattern of: a) SA-In₂O₃ (black line) and SA-W-In₂O₃ (red line) calcined at 400°C/3h; b) HT-In₂O₃ (black line) and HT-W-In₂O₃ (red line) calcined at 400°C/3h; c) WO₃ powder, obtained by calcination at 400°C for 3h of WCl₆ precursor.

In order to evaluate a possible shift of the diffraction peaks, XRD analysis were repeated by using quartz as an internal standard. Considering the six main peaks related to (211), (222), (400), (431), (440) and (622) planes, a certain shift to lower 2θ values (0.03° of 2θ) was determined for the doped powders as compared to the un-doped ones. Thus, lattice parameter a was slightly increased in SA-W-In₂O₃ and HT-W-In₂O₃ samples as compared to the un-doped respective materials, as reported in Table 1. This change in the lattice constant can be due to the substitution by W dopants in the In₂O₃ cell, in spite of a much smaller ionic radius for the octahedral W(VI) (74 pm), compared to octahedral and trigonal prismatic In(III) (94 pm) [42]. A decrease in cation occupancy is then necessary to maintain the electrical neutrality of the lattice cell when replacing In³⁺ by W⁶⁺ ions. This decrease in cation occupancy may be responsible for cell's distortion and for the increase of bond length [43]. resulting in. Thus, the observed slight increase of the lattice constant.

Table 1. Lattice parameters and crystallite size calculated by Scherrer equation for the four powders obtained.

Material	Crystallite size (nm)	Lattice parameter (a, nm)
SA-In ₂ O ₃	48	1.0078
SA-W-In ₂ O ₃	48	1.0089
HT-In ₂ O ₃	26	1.0083
HT-W-In ₂ O ₃	26	1.0092

In both cases, doping with WO_3 causes an increase of 0.1% in lattice parameter a . Indium oxide crystallizes in a cubic bixbyte-type structure consisting in a body centered cubic unit cell (BCC) belonging to the space group Ia3 number 206, where In atoms lay in the centers of the cube and oxygens stay on the vertices with an oxygen vacancy per each base of the cube. The overall structure consists of two types of In atoms surrounded by oxygen in the octahedral and trigonal prismatic coordination, alternatively. Both coordination groups may be described as distorted octahedra: probably, after doping and thermal treatment, WO_3 partially enters in the crystal lattice of In_2O_3 , distorting the BCC cell.

As a summary of the XRD analyses, we can postulate a twofold role of W-doping within the In_2O_3 matrix: a partial crystallization of WO_3 on the In_2O_3 surface (as indicated by the new broad XRD signal identified in the doped-powders), and a partial WO_3 solubilization inside the In_2O_3 matrix (as indicated by the lattice parameters change after doping).

In Fig. 3, the particle size distribution of doped and un-doped SA and HT powders are depicted.

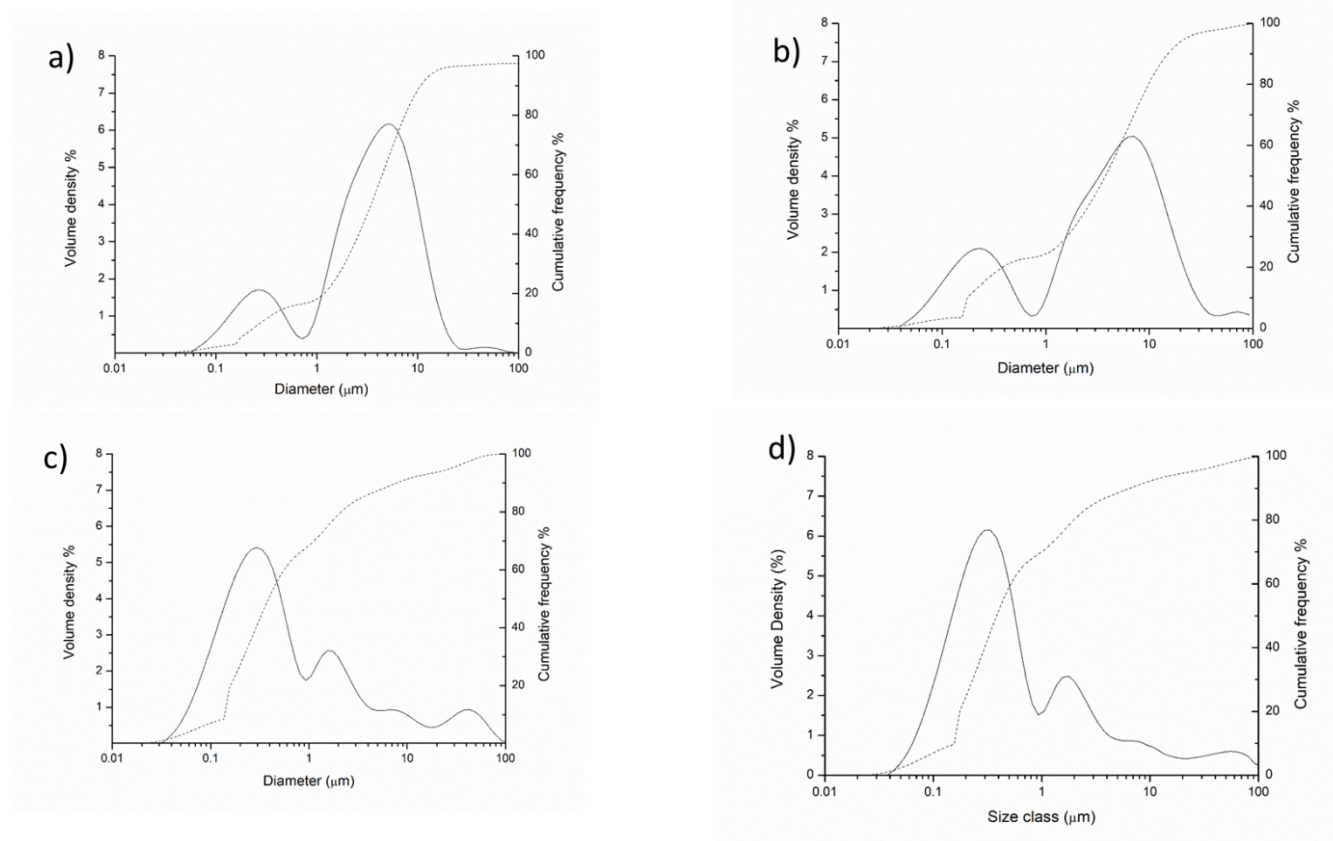


Fig. 3. Particle size distribution of SA-In₂O₃ (a); SA-W-In₂O₃ (b); HT-In₂O₃ (c); HT-W-In₂O₃ (d) powders, in volume density % (straight line) and as cumulative frequency % (dashed line).

Laser granulometry represented in Figure 3 of doped and undoped indium oxide powders evidenced that both SA-In₂O₃ and SA-W-In₂O₃ powders exhibit a multimodal distribution: the maxima of the most evident peaks are located at 0.25, 2.5, 5.642 and 45 μm for SA-In₂O₃ and at 0.22, 2.1, 7.5 and 68 μm for SA-W-In₂O₃. In the case of the synthesized powders, HT-In₂O₃ distribution shows maxima at about 0.23, 1.8, 7 and 40 μm and HT-W-In₂O₃ at 0.32, 1.8, 12 and 58 μm. The particle size distribution of HT-W-In₂O₃ exhibits a slightly lower d₉₀ value compared to the HT-In₂O₃, that was the smallest among the oxides investigated, in agreement with FESEM observations.

Table 2 collects the values corresponding to the 10, 50 and 90% of the cumulative distribution of all four powders, showing lower values for the HT-powders compared to the SA-ones. In addition, HT-W-In₂O₃ showed the smallest d₉₀ values among all the investigated powders.

Table 2. Particle size corresponding to 10, 50 and 90% of the cumulative distribution for the SA and HT doped and un-doped powders.

Cumulative (%)	SA-In ₂ O ₃ (μm)	SA-W-In ₂ O ₃ (μm)	HT-In ₂ O ₃ (μm)	HT-W-In ₂ O ₃ (μm)
10	0.29	0.18	0.11	0.10
50	3.67	4.02	0.41	1.36
90	11.40	16.00	8.34	4.55

A comparison between the morphology and the structure of the doped SA and HT powders is depicted in Fig. 4, showing the TEM (a, b) and HRTEM (c-f) micrographs of SA-W-In₂O₃ and HT-W-In₂O₃ powders. From the TEM bright-field images, the powders appear slightly agglomerated, with primary particles ranging between 20 and 60 nm in both cases. By HRTEM, lattice fringes of 0.253

nm were measured (see the yellow lines in figures c and e) and associated to the In_2O_3 (400) crystallographic plane. In addition, still by HRTEM micrographs, we can observe the presence of WO_3 nanoparticles on the In_2O_3 surface for both SA-W- In_2O_3 and HT-W- In_2O_3 powders. This was confirmed by chemical analysis performed by EDX nanoprobe, thus strengthening the hypothesis that WO_3 is present not only in the In_2O_3 lattice as evidenced by XRD analysis, but it is also situated on the surface of In_2O_3 as nanoparticles. Finally, no evidence of the lattice spacing corresponding to the principal planes of WO_3 , such as (200), (020) and (002) was found in such micrographs, probably due to the very small size of WO_3 grains and their poor crystalline grade, making difficult its clear detection.

Inks were prepared from both SA and HT powders, and used to develop gas sensing films, as described in the Experimental section. In Fig. 5, FESEM micrographs of all developed films, after calcination at 600°C for 1h, are depicted. SA- In_2O_3 (Fig. 5a) and SA-W- In_2O_3 (Fig. 5b) films show a very homogeneous microstructure, with primary particles ranging between 50-70 nm ($61.12 \pm 8.94 \mu\text{m}$) and characterized by almost spherical shape. The agglomerates diameters are in the range of few microns, and no significant modification in size and shape of primary particles was detected after doping.

HT- In_2O_3 (Fig. 5c) and HT-W- In_2O_3 (Fig. 5d) films show a slightly less homogeneous and more porous microstructure, but still characterized by very fine grains. In fact, the primary particles, characterized by cubic or even sharp edge morphologies, with size between 30 and 40 nm ($34.97 \pm .6.77 \mu\text{m}$), are clearly evident. Particles present a slight agglomeration, with agglomerates in the range 1-3 μm . The HT-W- In_2O_3 material shows approximately the same morphology of the un-doped HT- In_2O_3 .

Sensor thickness was measured by FESEM in cross-section (Fig. 5e) and a value of $20.1 \pm 1.2 \mu\text{m}$ was obtained as an average of 10 measurements.

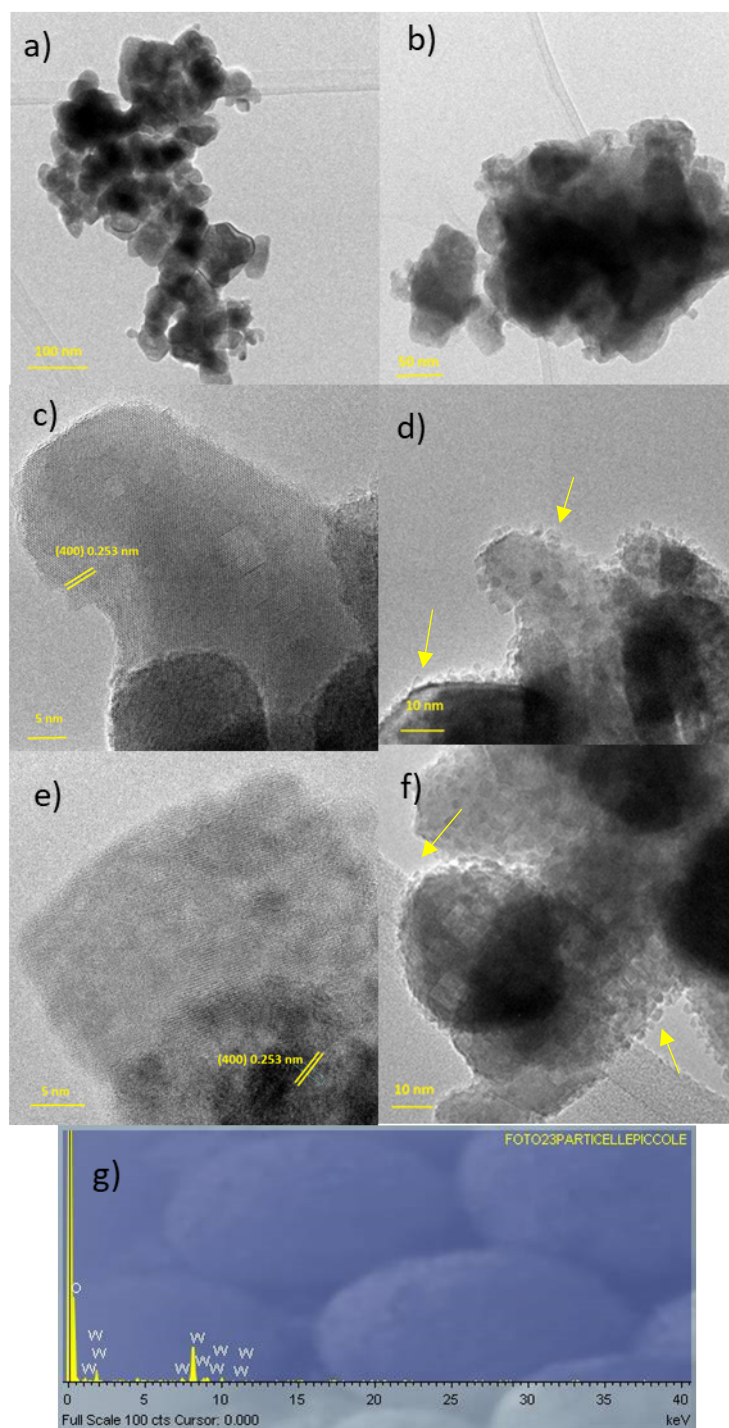


Fig. 4. TEM micrographs (a, b) of SA-W-In₂O₃ and HT-W-In₂O₃, respectively. HRTEM images of SA-W-In₂O₃ (c, d) and of HT-W-In₂O₃ (e, f). All powders were thermal treated at the same temperature (600°C/1h). The yellow arrows show the WO₃ nanoparticles identified by EDX analysis (g).

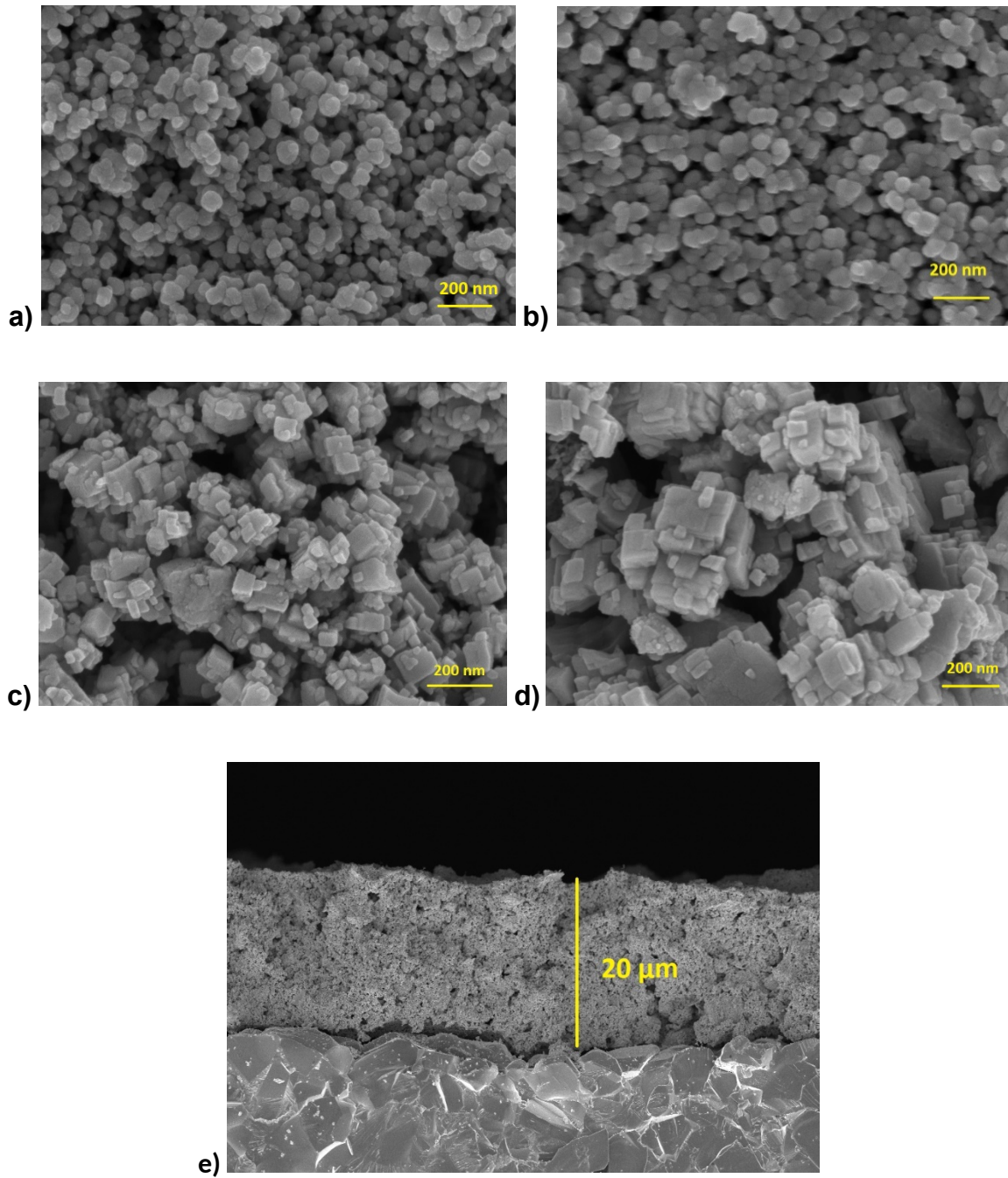


Fig. 5. FESEM micrographs of sensors (150 kx): SA- In₂O₃ (a), SA-W- In₂O₃ (b), HT-In₂O₃ (c), HT-W-In₂O₃ (d) [and an image in cross-section of the sensitive layer \(e\)](#).

Annealing at 600°C leads to a certain increase of the crystallite size as compared to the 400°C-calcined powders. In fact, for the HT powders, the crystallite size increased from 26 nm to 39 nm after calcination at 600°C. However, such size was still smaller than the respective 600°C-calcined SA powders, whose crystallite size was about 54 nm.

In addition, FESEM observations performed perpendicularly to screen-printed sensors (not shown here) allowed to estimate the film thickness: values of $20.6 \pm 2.7 \mu\text{m}$ and $21.4 \pm 1.9 \mu\text{m}$ were respectively determined for SA-In₂O₃ and HT-In₂O₃ films.

The N₂ adsorption isotherms for all four materials after the same firing temperature (600°C) were performed. First, the hydrothermal synthesis leads to a higher SSA compared to the commercial powder: it was in fact 13.3 m²/g for SA-In₂O₃ and more than double (27.7 m²/g) for HT-In₂O₃. In addition, the doping procedure, followed by thermal treatment, leads to a further moderate increase in SSA for both powders, being 15.2 m²/g for SA-W-In₂O₃ and 38.0 m²/g for HT-W-In₂O₃. Thus, a significant higher value was still determined for the synthesized material.

The chemical states of In, O and W atoms in all materials were investigated by XPS, and survey spectra are reported in Fig. 6. From these surveys, it is possible to appreciate the presence of W in the doped samples, SA-W-In₂O₃ (b) and HT-W-In₂O₃ (d).

Moreover, the deconvolution of In, O and W peaks in high resolution was performed. Fig. 7 shows the spin-orbit split for indium 3d_{5/2} and In 3d_{3/2} of trivalent indium for the commercial powders. The 3d characteristic peaks were measured respectively at 443.89 eV and 451.45 eV, descriptors of the binding energy of In³⁺ ion in the SA-In₂O₃ [44]. Those peaks were measured at 444.25 eV and 451.80 eV in the case of SA-W-In₂O₃, with a moderate shift at higher binding energy. The same trend was measured for HT-In₂O₃ and HT-W-In₂O₃ (not shown), where the In 3d_{5/2} and 3d_{3/2} peaks were determined at 444.16 eV and 451.60 eV for the un-doped powders, and shifted to 444.39 eV and 451.83 eV in the doped samples. This shift could be due to the different charge density of W⁶⁺ compared to In³⁺, with a smaller ionic radius for W respect to In, as described above. Electrons are provided into the indium matrix from WO₃. Consequently, characteristic peaks of indium are present at higher binding energy [due to](#) screening effect, [for](#) an electronic interaction between In₂O₃ and WO₃ [45]. A doping element with high Lewis acid strength like W decreases the scattering of charge carriers, thereby increasing the mobility of carriers. This results in screening of the dopant's effective charge. This screening effect weakens the interaction between dopant and charge carriers.

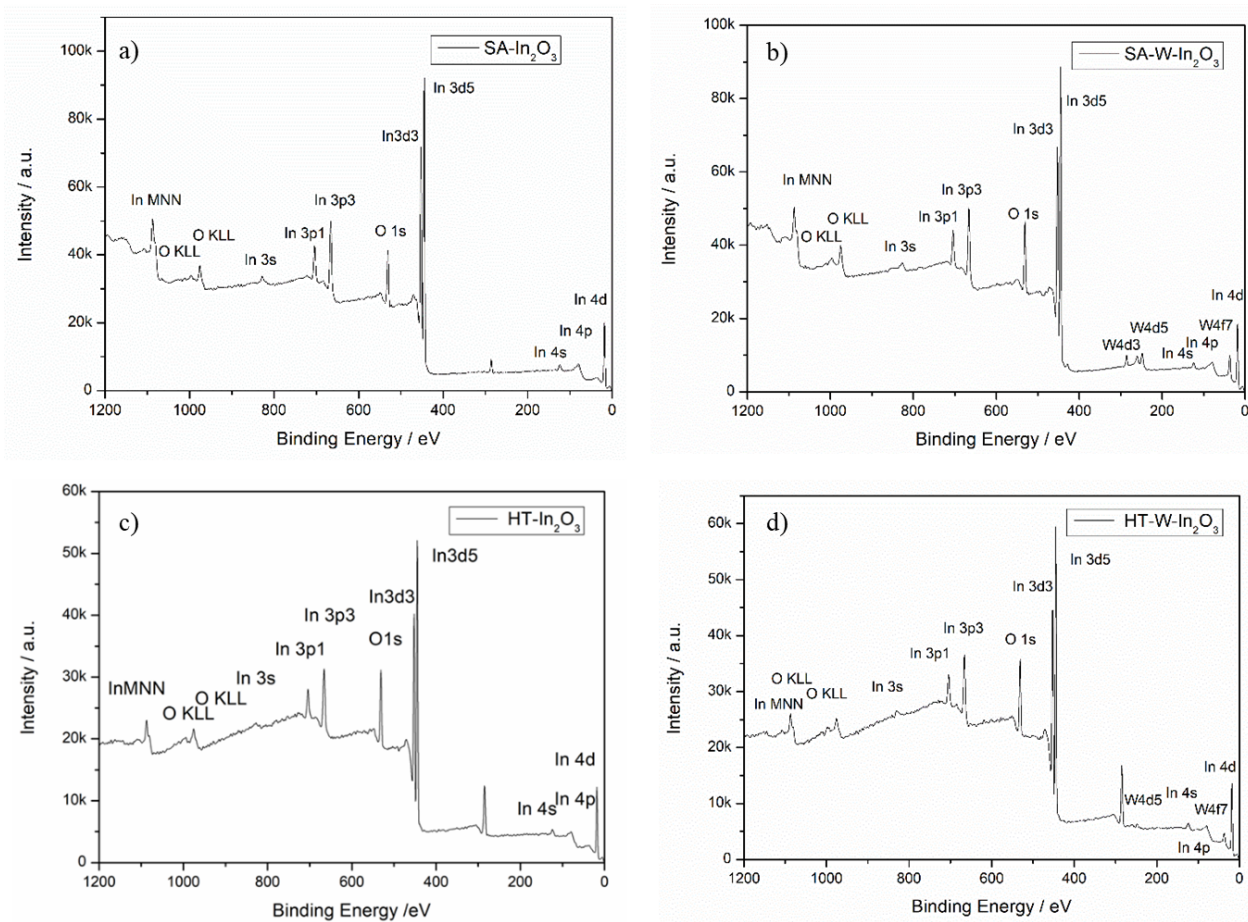


Fig. 6. Survey XPS spectra of: SA-In₂O₃ (a); SA-W-In₂O₃ (b); HT-In₂O₃ (c); HT-W-In₂O₃ (d).

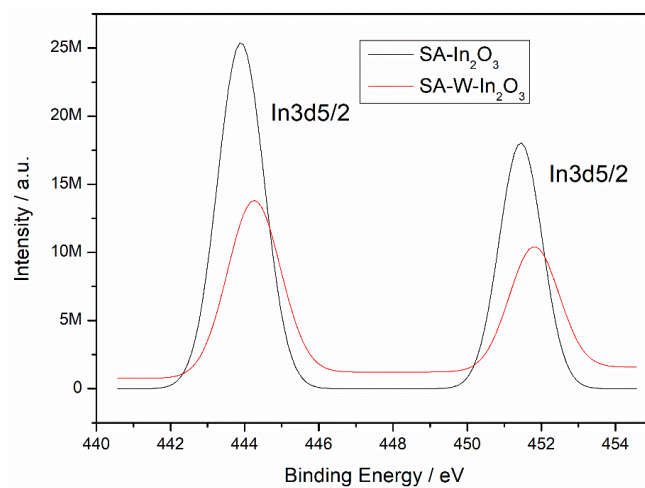


Fig. 7. High resolution XPS spectra of In 3d in: SA-In₂O₃ (black line); SA-W-In₂O₃ (red line) showing a moderate shift towards higher binding energy for the doped powder.

High resolution analyses of O 1s in SA-In₂O₃ and SA-W-In₂O₃ are depicted in Fig. 8 and show that both spectra can be deconvoluted into three components: lattice oxygen (O_l), chemisorbed oxygen (O_c) and hydroxyl oxygen (O_{hy}) [46]. The same behavior was observed in HT-powders as well. The binding energy and relative intensities of these three oxygen peaks are summarized in Table 3.

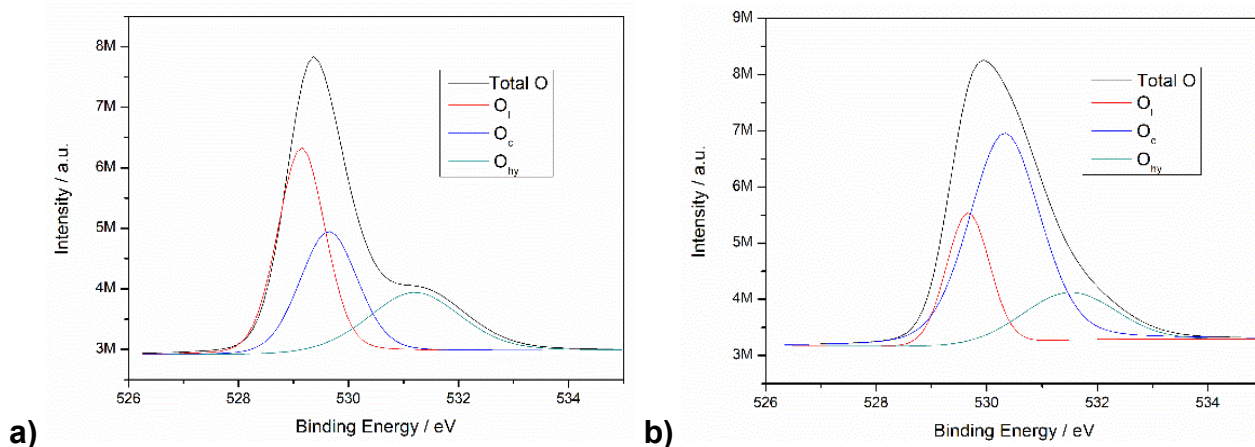


Fig. 8. High resolution XPS spectra of O 1s performed on SA-In₂O₃ (a) and SA-W-In₂O₃ (b). O_l: lattice oxygen; O_c: chemisorbed oxygen; O_{hy}: hydroxyl oxygen.

Table 3. Binding energy value and relative intensities of the oxygen peaks for the 4 powders.

Sample	Binding energy (eV)	Relative intensity (%)	Type of oxygen	Sample	Binding energy (eV)	Relative intensity (%)	Type of oxygen
SA-In ₂ O ₃	529.13	44.0	Lattice	SA-W-In ₂ O ₃	529.66	21.6	Lattice
	529.69	31.3	Chemisorbed		530.32	61.9	Chemisorbed
	531.29	24.7	Hydroxyl		531.51	16.5	Hydroxyl
HT-In ₂ O ₃	529.62	47.1	Lattice	HT-W-In ₂ O ₃	530.00	50.9	Lattice
	530.38	9.4	Chemisorbed		531.29	17.6	Chemisorbed
	531.48	43.5	Hydroxyl		532.11	31.5	Hydroxyl

From these data, we can observe that for both the SA and HT powders, the amount of the chemisorbed oxygen is much higher for the doped materials compared to the un-doped ones. In a

~~particular way~~Specifically, in both SA-W-In₂O₃ and HT-W-In₂O₃, the O_c values were the double than those determined in the respective pure materials. Such behavior can be partially explained by the slight increase of the SSA determined in the doped materials, as previously described. A more important effect can be attributed to the role of the W-dopant, since the doped materials were able to adsorb more oxygen on the surface, because more vacancies could be filled. It is known that the sensing response is expected to occur mainly via electron transfer together with changes in the amount of chemisorbed oxygen species on the sensor surface, so the sensor performances generally improve with the increase of chemisorbed oxygen. In addition, the presence of intrinsic defects from W influence the properties of the semiconductor [46]. Moreover, WO₃ on the surface of In₂O₃ can improve the O₃ sensitivity via spillover-effect (i.e improving the dissociation of O₃). It is well known that spillover-effect is explained by an increased dissociation of oxygen molecules into oxygen ions. In this mechanism, a weak bond is formed between an oxygen molecule and a W atom forming a complex component. This can be easily broken into oxygen ions by trapping free electrons that can diffuse to the surface vacancies of the In₂O₃ NPs. Therefore, more trapped electrons are created, leading to an increase in sensor response.

Besides the increase of the chemisorbed oxygen, the contribution of hydroxyl oxygen is reduced for W-doped materials (from 24.69% to 16.53% for SA- In₂O₃ and SA-W- In₂O₃ and from 43.51% to 31.46% for HT- In₂O₃ and HT-W- In₂O₃), thus more sites are available for ozone adsorption.

In addition, the W 4f high resolution spectrum of SA-W-In₂O₃ is depicted in Fig. 9. We can observe a doublet with binding energies of 35.6 eV for W 4f_{7/2} and 37.7 eV for W 4f_{5/2}, corresponding to the W⁶⁺ oxidation state [47]. Usually, W⁶⁺ signal of WO₃ is observed at binding energies of 36.1 eV (W4f_{7/2} in WO₃) and the W4f region has well separated spin-orbit components with symmetric W4f peaks ($\Delta=2.17$ eV) [47]. The same behavior was observed in HT-W-In₂O₃ sample (not shown).

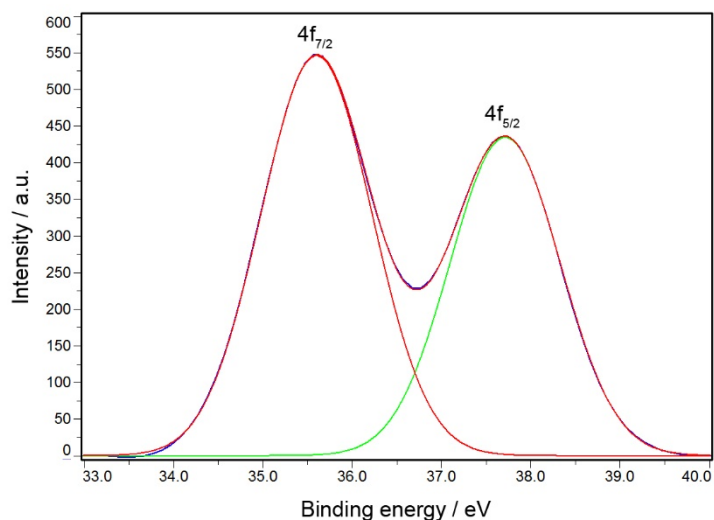


Fig. 9. High resolution XPS spectra of W4f performed on SA-W-In₂O₃.

3.2 Gas sensing properties

For each type of sensor, three different devices were fabricated in order to study the reproducibility of the measurements. A maximum standard deviation of 7% was then calculated respect to the average response of each composition. Firstly, the optimization of the firing temperature (in the range 400-600°C) and of the WO₃ amount (in the range 1.25-5 wt%) was performed on SA sensors. Results are summarized in Fig. 10.

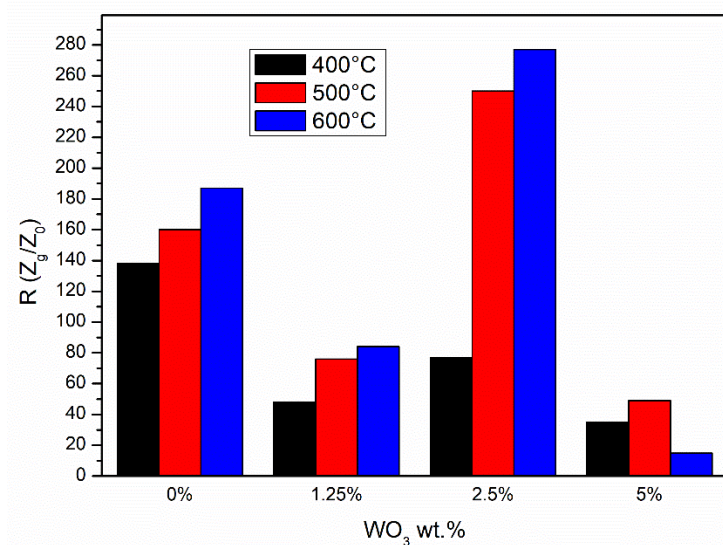


Fig. 10. Sensor film responses prepared with SA-In₂O₃, doped with different concentrations of WO₃: 1.25, 2.5 and 5 wt% and fired at 400°C, 500°C and 600°C for 1 hour under 500 ppb of O₃ in dry air and at 115°C.

First, we can observe that – with the only exception of 5 wt%-W-doped In₂O₃, the sensor response increased by increasing the firing temperature. In fact, calcination at 600°C improved at the same time the adhesion of the thick film upon the ceramic substrate and the ohmic contacts between the film and the interdigitated electrodes. Then, we can observe a significantly improved response at 2.5 wt% WO₃ as compared to the other concentrations. It was supposed that lower amounts were not sufficient to achieve the synergic effects of lattice and surface doping of tungsten oxide into indium oxide. In fact, from XRD analysis, both 1.25 and 2.5 wt% WO₃-SA samples showed the same shift as compared to the undoped powder, suggesting that in the case of 1.25 wt% WO₃, the dopant was predominantly located in the In₂O₃ lattice. At 5 wt%, probably bigger clusters of WO₃ are formed on the In₂O₃ surface decreasing the efficiency of spillover-effect between the two metal oxides.

As a result of the characterization carried out on SA-materials, all sensors were prepared by firing at 600°C for 1 hour, and the doped SA and HT sensors contained 2.5 wt% WO₃. Fig. 11 displays the sensor response for SA-In₂O₃, SA-W-In₂O₃, HT-In₂O₃ and HT-W-In₂O₃. Generally, their impedance increased from hundreds Ohm under dry air up to several tens of kOhm when exposed to O₃ 500 ppb. The optimum working temperature was equal to 115°C for SA- In₂O₃ and SA-W-In₂O₃, and 75°C for HT- In₂O₃ and HT-W- In₂O₃, as depicted in Fig. 11.

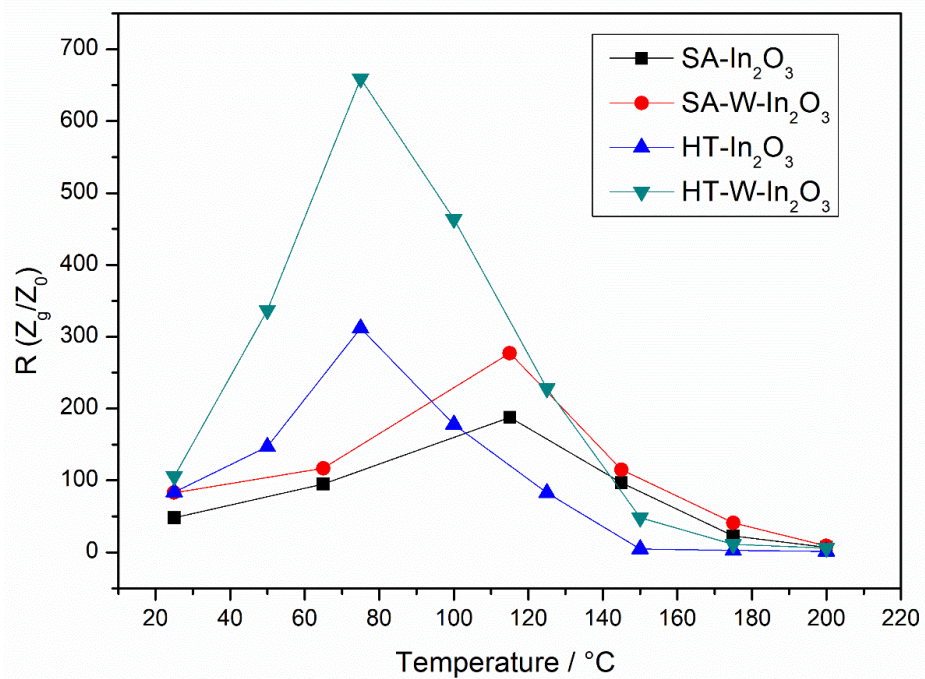
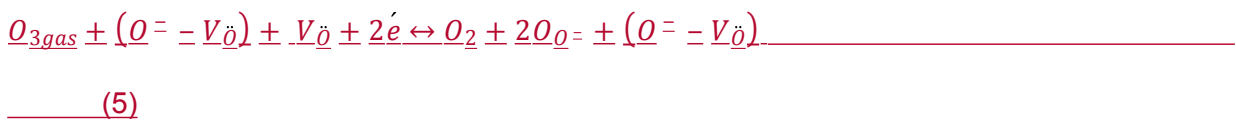


Fig. 11. Sensor film response at different operating temperatures (25-200°C) under 500 ppb O₃:

SA-In₂O₃, SA-W-In₂O₃, HT-In₂O₃ and HT-W-In₂O₃.

Generally, by doping with WO₃, both SA and HT In₂O₃ sensors showed an improvement of performances, because in the doped indium oxides more chemisorbed oxygen ions are present and available in the O₃ adsorption mechanism involving the filling of oxygen vacancies following the equation 5:



In accordance with Kröger–Vink Notation, O_o represent lattice oxygen, whereas V_{̇O} oxygen vacancy. From this reaction, O₃ has a great affinity for the reaction with oxygen vacancies (V_{̇O}) rather than with adsorbed oxygen species, O⁻ = V_{̇O}. Following this route, electrons of the conduction band of the material are consumed. After ozone interaction, the thickness of the depletion layer increases and the concentration of the charge carrier is dropped down, thus the impedance value of

the sensor increases. In the case of W-doped indium oxide, O_3 is dissociated quickly by spillover effect in O^- . This process is promoted by the presence of tungsten trioxide.

The sensor response is increased by 48% after doping for commercial indium oxide at 115°C with no effect on the optimum operating temperature and by 111% for synthesized indium oxide sensors at 75°C . In addition, in the case of HT-powders, optimum operating temperature was significantly decreased (i.e. equal to 75°C), which is consistently lower than the temperature determined for SA ones, which is around 115°C . By synthesizing via hydrothermal route indium oxide nanoparticles, it was possible to increase significantly the sensor response and to decrease at the same time the optimum operating temperature, due to the lower crystallite and agglomeration size together with a higher specific surface area obtained for the HT- In_2O_3 . Nevertheless, the response and recovery time at 75°C were quite longer for practical application (around 10-12 minutes), and for this reason the optimum operating temperature was chosen equal to 100°C . In this case, sensor response and recovery times were in the order of 2 minutes after exposure to 500 ppb of O_3 (Table 4).

Impedance variation of HT-W- In_2O_3 sensor (doped with 2.5 wt% WO_3 and fired at 600°C) at the selected optimized temperature, 100°C under different ozone concentrations in the range 200-500 ppb, is displayed in Fig. 12.

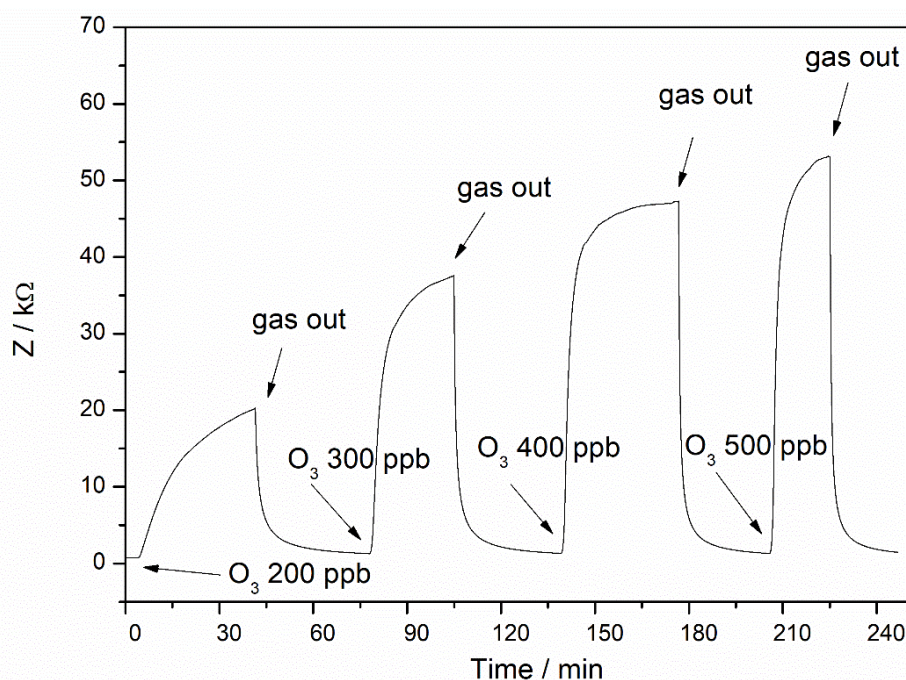


Fig. 12. Impedance variation of HT-W-In₂O₃ film (doped with 2.5 wt% WO₃ and fired at 600°C) towards different concentration of O₃ at 100°C [in the range 200-500 ppb](#).

It appears evident that sensor response and recovery times are both relatively short, in the order of few minutes for the diverse investigated O₃ concentrations, as tabulated in Table 4, and are faster for higher concentration of ozone [48]. Moreover, impedance's variation of two orders of magnitude were measured in the sub-ppm level of O₃ concentration.

Table 4. HT-W-In₂O₃ sensor response and recovery times (respectively the time needed for the sensor to reach 90% of the impedance variation under adsorption and desorption of ozone) at different ozone exposure in the range 200-500 ppb at 100°C.

Ozone concentration (ppb)	Response time (s)	Recovery time (s)
200	992	298
300	567	241
400	387	129
500	267	199

In Fig. 13 the calibration curve of HT-W-In₂O₃ sensor towards O₃ 200-500 ppb at 100°C is depicted, with a linear trend in the concentration range investigated, and a sensitivity equal to 0.879 ppb⁻¹, in accordance with IUPAC's definition.

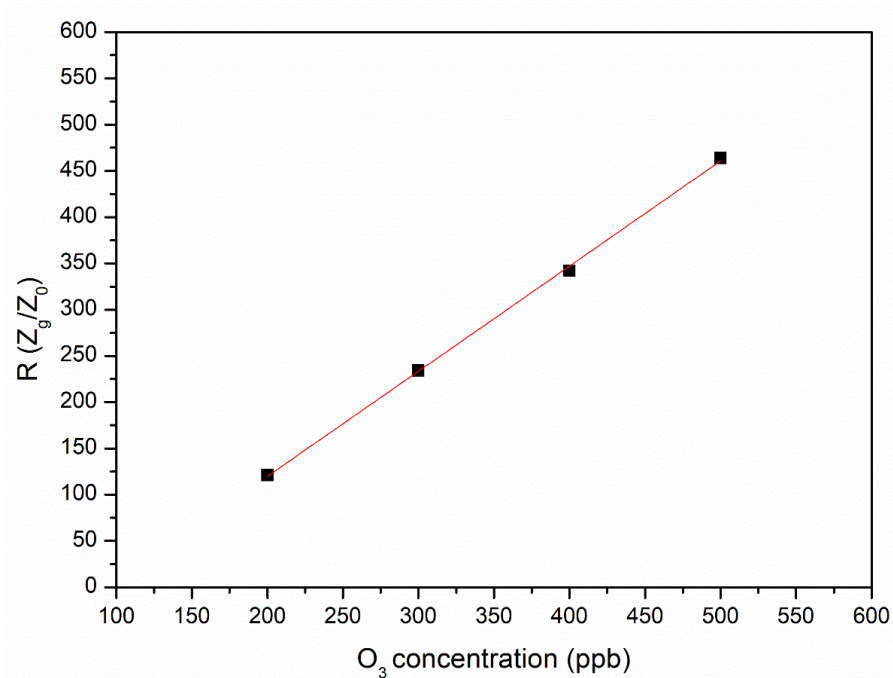
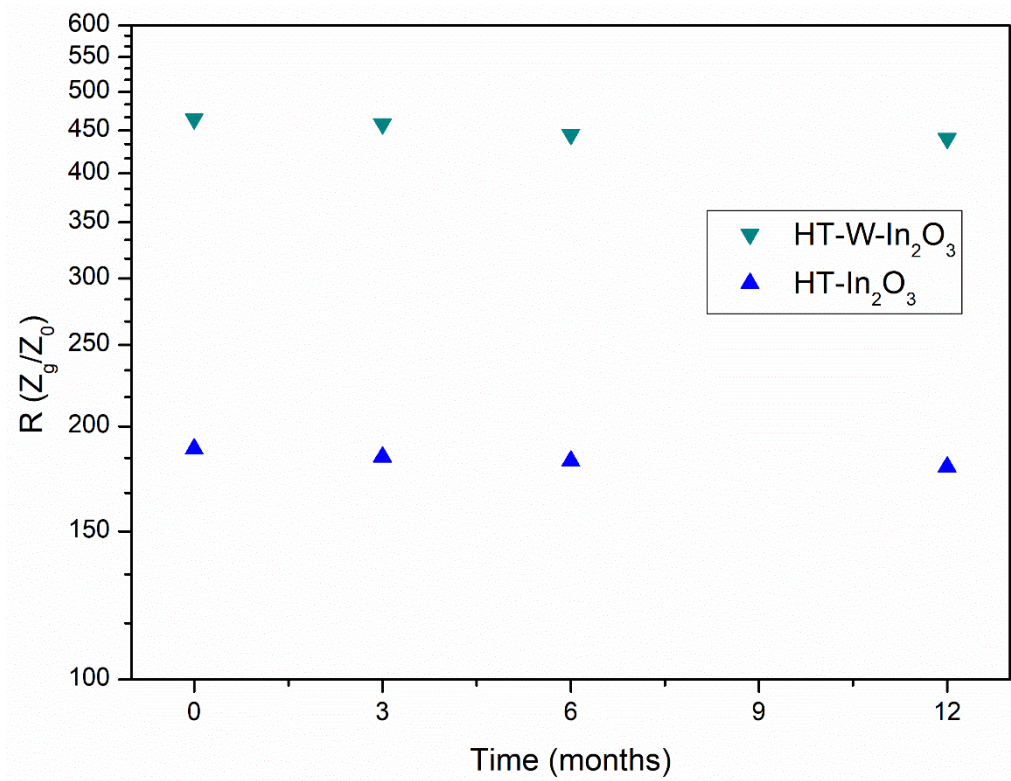


Fig. 13. Calibration curve of HT-W-In₂O₃ film (doped with 2.5 wt% WO₃ and fired at 600°C) towards different concentration of ozone at 100°C.

Long-term stability of HT-In₂O₃ and HT-W-In₂O₃ sensors were evaluated after 3, 6 and 12 months. Sensor responses at 100 °C under 500 ppb of O₃ are depicted in Fig 14. After 1 year of aging, sensor response is still equal to 95% of the fresh sensor response.



[Fig 14. Long-term stability of HT-In₂O₃ and HT-W-In₂O₃ sensors: fresh, after 3, 6 and 12 months under 500 ppb of O₃ at 100°C.](#)

Results of cross-sensitivity tests for all the investigated sensors are depicted in Fig. 154 towards NH₃ (50 ppm), CH₄ (50 ppm), humidity (50 RH%), CO₂ (500 ppm), N₂O (15 ppm), CO (10 ppm) and NO₂ (250 ppb).

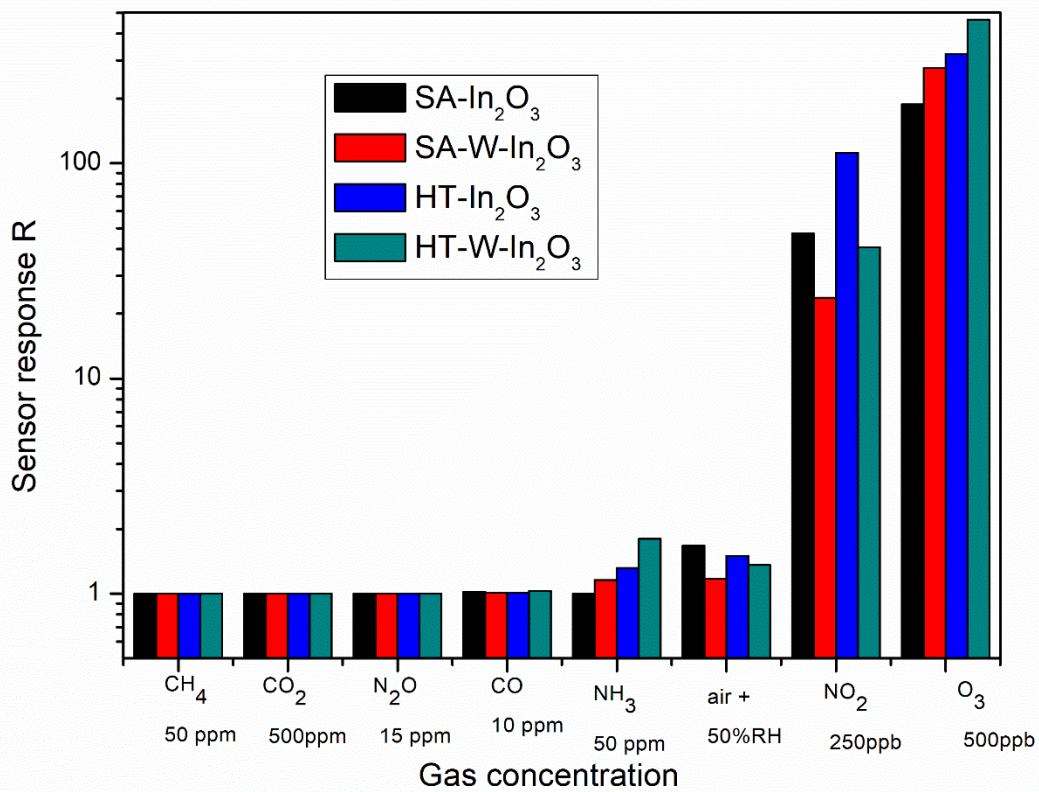
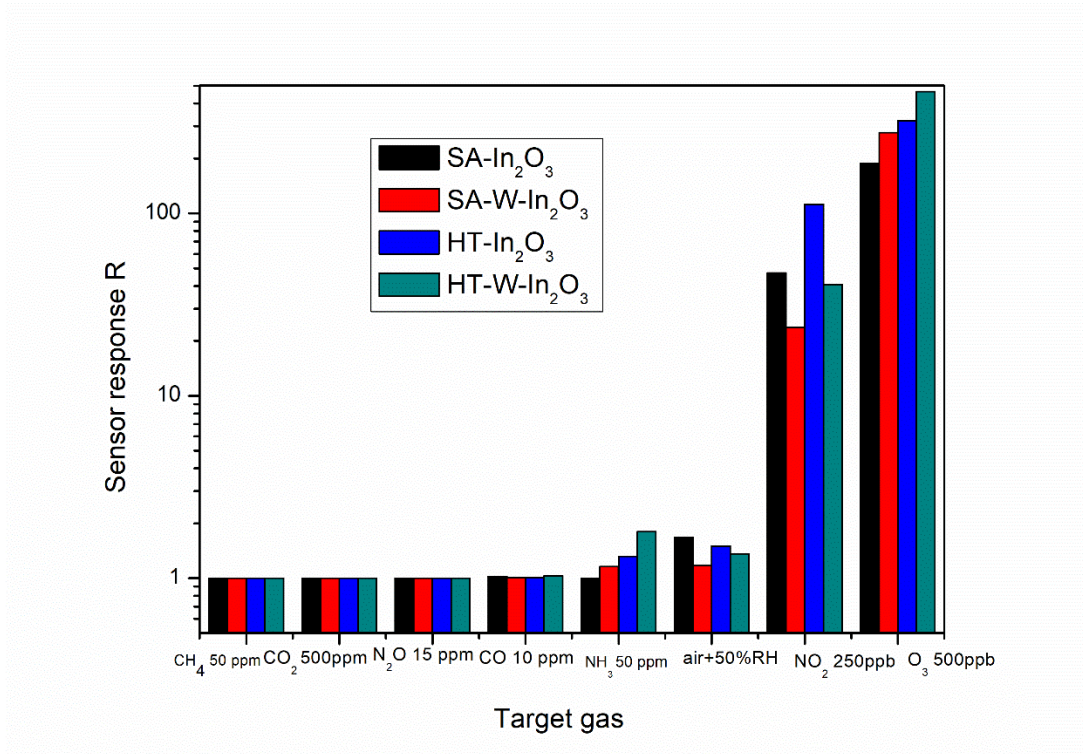


Fig. 154. Cross-sensitivity measurements for SA-In₂O₃, SA-W-In₂O₃, HT-In₂O₃ and HT-W-In₂O₃ sensor at 100°C.

A slight interference with humidity was observed for all the sensors, as well known from the literature [32] even if, in the case of $W\text{-In}_2\text{O}_3$ films, the response was decreased under exposure of water vapor respect to undoped materials. The effect of water molecules was also evaluated for all types of sensors by exposing them towards different values of RH (30%, 50% and 70%), and results are depicted in Fig. 165. The W -doped sensors exhibit a moderate response to humidity respect to the base line impedance of the undoped materials, both for commercial and synthesized indium oxide. Specifically, for $HT\text{-}W\text{-In}_2\text{O}_3$, no effect of humidity up to 30% was measured respect to a linear correlation between sensor response and humidity amount for the other types of sensors (Fig. 165). In accordance with XPS analysis where the presence of OH groups is decreased for W -doped materials.

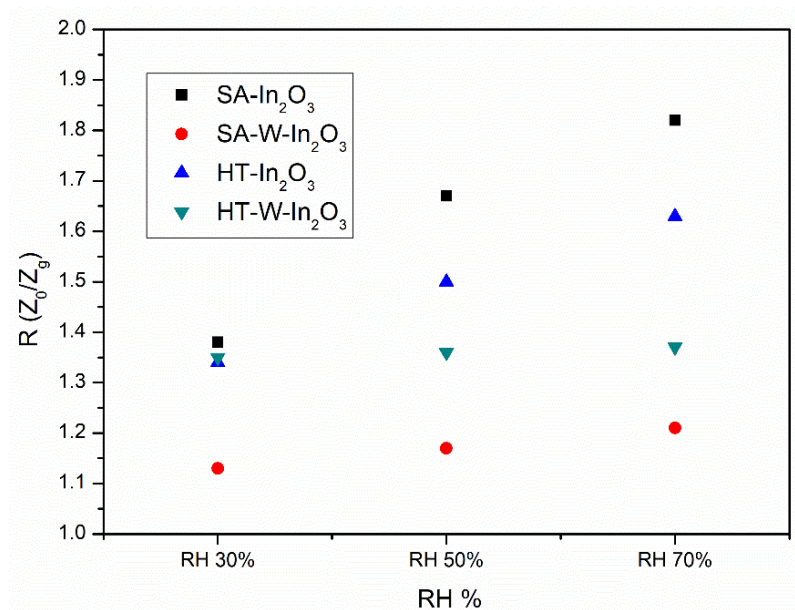


Fig. 156. Humidity effect at 30-50-70% of RH for $SA\text{-In}_2\text{O}_3$, $SA\text{-}W\text{-In}_2\text{O}_3$, $HT\text{-In}_2\text{O}_3$ and $HT\text{-}W\text{-In}_2\text{O}_3$ film at 100°C .

HT-based indium oxide sensors also exhibited a limited response towards ammonia 50 ppm.

Considering oxidizing gases, no cross-sensitivity with carbon dioxide was detected and an expected cross-sensitivity for NO_2 -since the interaction mechanism is comparable with respect to O_3 was

evidenced. This interference is decreasing in the case of the doped indium oxide, both SA and HT. In fact, when WO_3 is added to In_2O_3 , the selectivity for O_3 appears to be enhanced in terms of humidity and nitrogen dioxide and decreased in terms of ammonia detection. Generally, In_2O_3 sensors are much more sensitive towards oxidant gases respect to reducing ones, in accordance with the literature [31,34]. The difference between results towards O_3 and NO_2 can be described by the different oxidant power of the two gases. Probably, WO_3 can exploit an efficient spillover-effect under ozone exposure (i.e. dissociating it easily) but is not as effective under NO_2 exposure. Finally, in Table 5, results of the present work are compared with the state of art concerning indium oxide-based sensor for O_3 detection.

Table 5. Some features of In_2O_3 thick film heated ozone sensors. Elaboration from ref. [1].

Technological route	Film thickness	Crystallite size	Max sensor response R: (R_g/R_o)	Conditions of measurements	References
Thick film, drop coating	2 μm	12 nm	300	85°C, 250 ppb, dry	[49]
Thick film, drop coating	/	8 nm	1500	200°C, 100 ppb, dry	[50]
Thick film, screen printing	/	8 nm	100	235°C, 1 ppm	[51]
Thick film, screen printing	20 μm	20 nm	120	270°C, 1ppm	[52]
Thick film, screen printing	/	/	180	330°C, 100 ppb	[53]
Thick film, screen printing	21.4 μm	25.6 nm	464	100°C, 500 ppb, dry	This work

Comparing our results with those of other studies based on indium oxide thick-films, maximum response is ordinarily achieved in the 200°-350°C temperature range. Only Starke et al. [49] obtained the maximum response at 85°C, a comparable working temperature of this work (100°C). Although, the deposition technique was different (drop coating) together with film thickness (2 instead of 20 microns).

Grain size and film thickness are beyond the shadow of any doubt the main parameters responsible for sensor's performance. According to Gardon et al. [25], at lower temperature the gas penetration profile is higher for thick devices, allowing a sharply availability to inner grains for gas molecules. So, activation energy is lower for thick film-based metal oxide sensors because of heating of gas molecules upon diffusion through the metal oxide. For this reason, thick film-based gas sensors often exhibit an increased response at lower temperature in comparison with thin film technology.

The gas-sensing mechanism of In₂O₃-based sensors belongs mainly to the surface-controlled type at temperature lower than 100°C [54], and from [55] is known that in the temperature range 100-200°C, the sensing mechanism is governed both for surface and bulk effects.

~~When ozone is introduced on the indium oxide surface, it is dissociated following the equation-6:~~



~~Where e⁻ is an electron responsible for conduction in the oxide film, O⁻(s) are surface oxygen ions, and O₃(g) and O₂(g) are respectively the adsorbing ozone and desorbing oxygen molecules [1].~~

When indium oxide-based sensors are exposed to the ozone, the gas reacts with the oxygen vacancieschemisorbed oxygen species, that are more concentrated in the W-In₂O₃ materials compared to the reference indium oxide, as clarified in XPS investigation. Electrons are captured from the conduction band resulting in an increase in the film impedance and resistance. When the metal oxide is exposed to air again, sensors recover quickly to the initial electronic structure despite of the low operating temperature and the thickness of the film in the range of 20 μm.

The chemisorbed oxygen ions of the metal oxide enhance the ozone decomposition reaction on the sensor surface resulting in a higher sensor response towards ozone.

O_3 reacts with [oxygen vacancies in accordance with equation 5, increasing the oxygen adsorbates \(\$O^-\$, \$O^{2-}\$ and \$O_2^-\$ ions\), increasing the oxygen concentration, in accordance with equation 6. This process increases](#) the impedance of the In_2O_3 and $W-In_2O_3$ sensors, and continues up to a certain optimum temperature, beyond which the exothermic gas adsorption becomes more difficult and the gas molecules start to desorb in large amounts, leading to an important drop in the sensor response after $150^\circ C$ (Figure 11). The enhancement of O_3 -sensing performance of the doped indium oxide sensors can be attributed to the synergistic effect of the WO_3 and In_2O_3 nanoparticles. In addition, the configuration of WO_3 largely situated on the surface of In_2O_3 prevents the agglomeration of the WO_3 improving efficient paths for diffusion and adsorption of the target gas molecules. As a result, the hetero-junctions at the interface of WO_3 and In_2O_3 generate a special electron donor–acceptor system. Upon exposure to oxidant O_3 gas, the impedance of $W-In_2O_3$ increases, and more electrons migrate to accelerate the formation of electron depletion regions improving the gas-sensing performance. At the end, the synergistic effect of the In_2O_3 and WO_3 species with different dimensions are essential factors to improve the low-temperature gas sensing performance of the WO_3 -based materials.

Experimental results obtained in the present work indicate that the sensing properties depend on the chemical composition of the sensor, on the specific surface area and on the crystallite size of the semiconductor. Different tungsten trioxide concentrations were investigated, and in accordance with [56] with a WO_3 -doping of 3 at%, a concentration close to 5 wt% WO_3 investigated in this work, a minimum of resistivity together with a maximum carrier mobility is reached among a wide range of WO_3 doping concentration onto indium oxide film.

By increasing the amount of oxygen vacancies in metal oxide, more electrons are available for the material, increasing the n-type characteristics. This would shift the Fermi level closer to the conduction band shifting also the valence band upward. Furthermore, the electron affinity of the material will also increase because more electrons are added to In_2O_3 from WO_3 resulting in a higher electron affinity after the creation of oxygen vacancies.

The mechanism of O_3 adsorption involves both the crystallite and the agglomerates, and in the case of HT- In_2O_3 based sensors a decrease of both parameters was achieved improving noticeably the sensor response for O_3 detection [57].

4. Conclusions

This work has confirmed the exploitation of 2.5 wt% $WO_3-In_2O_3$ as sensitive material for ozone detection at sub-ppm level. W^{6+} ions create adsorption centers with higher affinity for oxygen adsorption, resulting in a higher sensitivity of indium oxide for a strong oxidant gas as ozone. Both response and recovery times of the sensor were reasonably fast (in the order of few minutes). The gas sensing behavior towards ozone of indium oxide nanoparticles synthesized by hydrothermal method with a capping agent (CTAB) with lower crystallite size and with a lower degree of agglomeration, together with an enhanced specific surface area, was improved respect to the commercial powder in terms of optimum operating temperature, sensor response and cross sensitivity. Moreover, impregnation of this as-prepared nano-powder with WO_3 at 2.5 wt% results in a partial solid solution formation with WO_3 laying also on the surface. Probably, WO_3 could promote the formation of Schottky junctions at microstructural level with In_2O_3 . This would lead to an electron transfer from WO_3 to In_2O_3 , decreasing the energy required for oxygen vacancies creation in the lattice. An efficient dissociative chemisorption of oxygen is promoted by WO_3 on the surface, followed by a spillover effect that is an effective path for refilling the oxygen vacancies. This leads to indium oxide-based sensors with higher sensitivity and faster response [58]. The baseline resistance and impedance of W-doped sensors is lower than the undoped ones, confirming the presence of additional electrons, which have to be introduced into the oxide lattice by oxygen vacancies formation or interstitial metal atoms ionization in order to maintain the overall neutrality of the cubic In_2O_3 crystal.

Comparing the sensor response of commercial and synthesized indium oxide, the sensor response of In_2O_3 -based thick film (20 μm) towards a strong oxidant like O_3 seems to be influenced by both the crystallite size and size of agglomerates. According to numerous studies in gas sensors based on strongly agglomerated materials, not only the grain size, but also the size and the gas penetrability

of agglomerates for detecting gas are fundamental parameters, controlling either the sensor response and its response kinetics [34, 59, 60]. Experiment proves that the film agglomeration, its thickness and gas penetrability often are essential parameters controlling operating characteristics of ozone sensors. Thus, a high degree of agglomeration favors the formation of “capsulated zones,” with closed porosity. As a result, properties of the sensing material in these zones do not depend on the surrounding gas concentration. Therefore, for agglomerated materials, in thick film type sensors, it is necessary to control primarily the size of agglomerates, and the results of laser granulometry confirm the improvement from SA- In_2O_3 to HT- In_2O_3 powders. XRD investigation assesses also that crystallite size is lower for HT- In_2O_3 compared to SA- In_2O_3 and that WO_3 slightly modifies the lattice parameter a of the cubic In_2O_3 structure.

Acknowledgements

The Authors are grateful to Mr. Mauro Raimondo for FESEM observations, Dr. Maria Carmen Valsania for TEM observations, Dr. Carlotta Pontremoli for N_2 adsorption measurements and Dr. Salvatore Guastella for XPS analysis.

Abbreviations

SA-In_2O_3	SA-W-In_2O_3	HT-In_2O_3	HT-W-In_2O_3
Indium oxide Sigma Aldrich	Indium oxide Sigma Aldrich doped with 2.5 wt.% of WO_3	Indium oxide hydrothermally synthesized	Indium oxide hydrothermally synthesized doped with 2.5 wt.% of WO_3

References

- [1] G. Korotcenkov, V. Brinzari, B. K. Cho, In₂O₃ - and SnO₂-based thin film ozone sensors: Fundamentals, Hindawi Publishing Corporation J. Sensors (2016) 1–31. <http://dx.doi.org/10.1155/2016/3816094>.
- [2] R. G. Rice, A. Netzer, Handbook of ozone technology and applications, Ann. Arbor. Science, Mich., USA, 1984.
- [3] P. Siesverda, A review of ozone applications in public aquaria, in Proceedings of the 9th Ozone World Congress (1989) 246–295, NY, USA.
- [4] V. Camel, A. Bermond, The use of ozone and associated oxidation processes in drinking water treatment, Water Res. 32 (1998) 3208–3222. [https://doi.org/10.1016/S0043-1354\(98\)00130-4](https://doi.org/10.1016/S0043-1354(98)00130-4).
- [5] <https://www.epa.gov/indoor-air-quality-iaq/ozone-generators-are-sold-air-cleaners>. Accessed 16 September 2019.
- [6] M. D. Rowe, K. M. Novak, P.D. Moskowitz, Health effects of oxidants, Environ. Int. 9 (1983) 515–528. [https://doi.org/10.1016/0160-4120\(83\)90008-9](https://doi.org/10.1016/0160-4120(83)90008-9).
- [7] J.A. Bernstein, N. Alexis, C. Barnes, I. L. Bernstein, A. Nel, D. Peden, D. Diaz-Sanchez, S. M. Tarlo, P. B. Williams, Health effects of air pollution, J. Allergy Clin. Immun. 114 (2004) 1116–1123. <https://doi.org/10.1016/j.jaci.2004.08.030>.
- [8] <https://www.epa.gov/ozone-pollution/2015-national-ambient-air-quality-standards-naaqs-ozone>. Accessed 16 September 2019.
- [9] M. Ando, C. Swart, E. Pringsheim, V. M. Mirsky, O. S. Wolfbeis, Optical ozone detection by use of polyaniline film, Solid State Ionics. 152 (2002) 819–822. [https://doi.org/10.1016/S0167-2738\(02\)00338-7](https://doi.org/10.1016/S0167-2738(02)00338-7).

- [10] R. A. Potyrailo, S. E. Hobbs, G. M. Hieftje, A simple, highly stable scintillator light source for ultraviolet absorption-based sensors, *Anal. Chim. Acta.* 367 (1998) 153–157. [https://doi.org/10.1016/S0003-2670\(98\)00148-2](https://doi.org/10.1016/S0003-2670(98)00148-2).
- [11] C. Eipel, P. Jeroschewski, I. Steinke, Determination of ozone in ambient air with a chemiluminescence reagent film detector, *Anal. Chim. Acta.* 491 (2003) 145–153. [https://doi.org/10.1016/S0003-2670\(03\)00797-9](https://doi.org/10.1016/S0003-2670(03)00797-9).
- [12] T. Takayanagi, P. K. Dasgupta, A chemiluminescence-based continuous flow aqueous ozone analyzer using photoactivated chromotropic acid, *Talanta* 66 (2005) 823–830. <https://doi.org/10.1016/j.talanta.2004.11.036>.
- [13] T. Doll, J. Lechner, I. Eisele, K.-D. Schierbaum, W. Göpel, Ozone detection in the ppb range with work function sensors operating at room temperature, *Sens. Actuators B. Chem.* 34 (1996) 506–510. [https://doi.org/10.1016/S0925-4005\(96\)01941-7](https://doi.org/10.1016/S0925-4005(96)01941-7).
- [14] D. V. Stergiou, T. Stergiopoulos, P. Falaras, M. I. Prodromidis, Solid redox polymer electrolyte-based amperometric sensors for the direct monitoring of ozone in gas phase, *Electrochem. Commun.* 11 (2009) 2113–2116. <https://doi.org/10.1016/j.elecom.2009.09.007>.
- [15] A. Bejaoui, J. Guerin, J.A. Zapien, K. Aguir, Theoretical and experimental study of the response of CuO gas sensor under ozone, *Sens. Actuators B. Chem.* 190 (2014) 8–15. <https://doi.org/10.1016/j.snb.2013.06.084>.
- [16] V. R. Mastelaro, S. C. Zilio, L. F. da Silva, P. I. Pelissari, M. I. B. Bernardi, J. Guerin, K. Aguir, Ozone gas sensor based on nanocrystalline SrTi_{1-x}FexO₃ thin films, *Sens. Actuators B. Chem.* 181 (2013) 919–924. <https://doi.org/10.1016/j.snb.2013.02.068>.
- [17] C. Wang, L. Yin, L. Zhang, D. Xiang, R. Gao, Metal oxide gas sensors- sensitivity and influencing factors, *Sensors.* 10 (2010) 2088-2106. <https://doi.org/10.3390/s100302088>.
- [18] N. Barsan, U. Weimar, Conduction model of metal oxide gas sensors, *J. Electroceram.* 7 (2001) 143–167. <https://doi.org/10.1023/A:1014405811371>.

- [19] G. F. Fine, L.M. Cavanagh, A. Afonja, R. Binions, Metal oxide semi-conductor gas sensors in environmental monitoring, *Sensors*. 10 (2010) 5469–5502. <https://doi.org/10.3390/s100605469>.
- [20] A. Berna, Metal oxide sensors for electronic noses and their application to food analysis, *Sensors*. 10 (2010) 3882–3910. <https://doi.org/10.3390/s100403882>.
- [21] K. Wetchakun, T. Samerjai, N. Tamaekong, C. Liewhiran, C. Siriwong, V. Kruefu, A. Wisitsoraat, A. Tuantranont, S. Phanichphant, Semiconducting metal oxides as sensors for environmentally hazardous gases, *Sens. Actuators B. Chem.* 160 (2011) 580–591. <https://doi.org/10.1016/j.snb.2011.08.032>.
- [22] G. Korotcenkov, Gas response control through structural and chemical modification of metal oxide films: state of the art and approaches, *Sens. Actuators B. Chem.* 107 (2005) 209–232. <https://doi.org/10.1016/j.snb.2004.10.006>.
- [23] G. Eranna, B. C. Joshi, D. P. Runthala, R. P. Gupta, Oxide materials for development of integrated gas sensors—a comprehensive review, *Crit. Rev. Solid State Mater. Sci.* 29 (2004) 111–188. <https://doi.org/10.1080/10408430490888977>.
- [24] G. Korotcenkov, B. K. Cho, Thin film SnO₂-based gas sensors: film thickness influence, *Sens. Actuators B. Chem.* 142 (2009) 321–330. <https://doi.org/10.1016/j.snb.2009.08.006>.
- [25] M. Gardon, J. M. Guilemany, A review on fabrication, sensing mechanism and performance of metal oxide gas sensors, *J. Mater. Sci-Mater. El.* 24 (2013) 1410-1421. <https://doi.org/10.1007/s10854-012-0974-4>.
- [26] M. Z. Atashbar, B. Gong, H. T. Sun, W. Wlodarski, R. Lamb, Investigation on ozone-sensitive In₂O₃ thin films, *Thin Solid Films*. 354 (1999) 222–226. [https://doi.org/10.1016/S0040-6090\(99\)00405-8](https://doi.org/10.1016/S0040-6090(99)00405-8).
- [27] X. Xu, X. Mei, P. Zhao, P. Sun, Y. Sun, X. Hu, G. Lu, One-step synthesis and gas sensing characteristics of urchin-like In₂O₃, *Sens. Actuators B. Chem.* 186 (2013) 61–66. <https://doi.org/10.1016/j.snb.2013.05.029>.

- [28] T. Wagner, J. Hennemann, C.-D. Kohl, M. Tiemann, Photocatalytic ozone sensor based on mesoporous indium oxide: influence of the relative humidity on the sensing performance, *Thin Solid Films*. 520 (2011) 918–921. <https://doi.org/10.1016/j.tsf.2011.04.181>.
- [29] G. Sberveglieri, C. Baratto, E. Comini, G. Faglia, M. Ferroni, A. Ponzoni, A. Vomiero, Synthesis and characterization of semiconducting nanowires for gas sensing, *Sens. Actuators B. Chem.* 121 (2007) 208–213. <https://doi.org/10.1016/j.snb.2006.09.049>.
- [30] T. K. H. Starke, G. S. V. Coles, High sensitivity ozone sensors for environmental monitoring produced using laser ablated nanocrystalline metal oxides, *IEEE Sens. J.* 2 (2002) 14–19. <https://doi.org/10.1109/7361.987056>.
- [31] M. Ivanovskaya, A. Gurlo, P. Bogdanov, Mechanism of O₃ and NO₂ detection and selectivity of In₂O₃ sensors, *Sens Actuators B. Chem.* 77 (2001) 264–267. [https://doi.org/10.1016/S0925-4005\(01\)00708-0](https://doi.org/10.1016/S0925-4005(01)00708-0).
- [32] G. Korotcenkov, Metal oxide composites in conductometric gas sensors: achievements and challenges, *Sens Actuators B. Chem.* 244 (2017) 182–210. <https://doi.org/10.1016/j.snb.2016.12.117>.
- [33] J. Ollitrault, N. Martin, J.Y. Rauch, J.B. Sanchez, F. Berger, Improvement of ozone detection with GLAD WO₃ films, *Mater. Lett.* 155 (2015) 1–3. <https://doi.org/10.1016/j.matlet.2015.04.099>.
- [34] G. Korotcenkov, V. Brinzari, B. K. Cho, In₂O₃ - and SnO₂- based ozone sensors: design and characterization, *Crit. Rev. Solid State Mater. Sci.* 43 (2018) 83–132. <https://doi.org/10.1080/10408436.2017.1287661>.
- [35] T. Yan, X. Wang, J. Long, P. Liu, X. Fu, G. Zhang, X. Fu, Urea-based hydrothermal growth, optical and photocatalytic properties of single-crystalline In(OH)₃ nanocubes, *J. Colloid Interface Sci.* 325 (2008) 425–431. <https://doi.org/10.1016/j.jcis.2008.05.065>.
- [36] D. V. Shinde, D. Y. Ahn, V. V. Jadhav, D. Y. Lee, N. K. Shrestha, J. K. Lee, Hwa Y. Lee, R. S. Maneb, S. H. Han, Coordination chemistry approach for shape-controlled synthesis of indium oxide

nanostructures and their photoelectrochemical properties, *J. Mater. Chem A.* 2 (2014) 5490–5498. <https://doi.org/10.1039/C3TA15407F>.

[37] https://www.sigmaaldrich.com/Graphics/COfAInfo/SigmaSAPQM/SPEC/63/632317/632317-BULK_____ALDRICH__.pdf. Accessed 16 September 2019.

[38] D. Ziegler, A. Marchisio, P. Palmero, J.-M. Tulliani, WO₃-doped indium oxide thick films for ozone detection at low temperature, *Proceedings.* 1 (2017) 428. <https://doi.org/10.3390/proceedings1040428>.

[39] W. H. Ho, S. K. Yen, Preparation and characterization of indium oxide film by electrochemical deposition, *Thin Solid Films.* 498 (2006) 80–84. <https://doi.org/10.1016/j.tsf.2005.07.072>.

[40] J.-L. Cao, Z.-L. Yan, Y. Wang, G. Sun, X.-D. Wang, H. Bala, Z.-Y. Zhang, CTAB-assisted synthesis of mesoporous CoFe₂O₄ with high carbon monoxide oxidation activity, *Mater. Lett.* 106 (2013) 322–325. <https://doi.org/10.1016/j.matlet.2013.05.054>.

[41] M. M. Bagheri-Mohagheghi, N. Shahtahmasebi, E. Mozafari, M. Shokooh-Saremi, Effect of the synthesis route on the structural properties and shape of the indium oxide (In₂O₃) nano-particles, *Physica E Low Dimens. Syst. Nanostruct.* 41 (2009) 1757–1762. <https://doi.org/10.1016/j.physe.2009.06.009>.

[42] <http://abulafia.mt.ic.ac.uk/shannon/radius>. Accessed 16 September 2019.

[43] R.D. Shannon, Revised effective ionic radii and systematic studies of interatomic distances in halides and chalcogenides, *Acta Cryst.* A32 (1976) 751–767. <https://doi.org/10.1107/S0567739476001551>.

[44] <https://xpssimplified.com/elements/indium.php>. Accessed 16 September 2019.

[45] Y.D. Zhang, G.C. Jiang, K.W. Wong, Z. Zhen, Green synthesis of indium oxide hollow spheres with specific sensing activities for flammable organic vapors, *Sensor Letters.* 8 (2010) 355–361. <https://doi.org/10.1166/sl.2010.1277>.

- [46] T. Zhang, F. Gu, D. Han, Z. Wang, G. Guo, Synthesis, characterization and alcohol-sensing properties of rare earth doped In_2O_3 hollow spheres, *Sens. Actuators B. Chem.* 177 (2013) 1180–1188. <https://doi.org/10.1016/j.snb.2012.12.024>.
- [47] <https://xpssimplified.com/elements/tungsten.php>. Accessed 16 September 2019.
- [48] Ch. Y. Wang, V. Cimalla, C.-C. Roehlig, A new type of highly sensitive portable ozone sensor operating at room temperature, in *Proceedings of the 5th IEEE Conference on Sensors*, 81–84, EXCO, Daegu, South Korea, 2006.
- [49] T. K. H. Starke, G. S. V. Coles, High sensitivity ozone sensors for environmental monitoring produced using laser ablated nanocrystalline metal oxides, *IEEE Sensors Journal*. 2 (2002) 14–19. <https://doi.org/10.1109/7361.987056>.
- [50] M. Epifani, E. Comini, J. Arbiol, R. Díaz, N. Sergent, T. Pagnier, P. Siciliano, G. Faglia, J. R. Morante, Chemical synthesis of In_2O_3 nanocrystals and their application in highly performing ozone-sensing devices, *Sens. Actuators B. Chem.* 130 (2008) 483–487. <https://doi.org/10.1016/j.snb.2007.09.025>.
- [51] T. Sahm, A. Gurlo, N. Barsan, U. Weimar, Properties of indium oxide semiconducting sensors deposited by different techniques, *Particul. Sci. Technol.* 24 (2006) 441–452. <https://doi.org/10.1080/02726350600934739>
- [52] A. Oprea, A. Gurlo, N. Bârsan, U. Weimar, Transport and gas sensing properties of In_2O_3 nanocrystalline thick films: a Hall effect based approach, *Sens. Actuators B. Chem.* 139 (2009) 322–328. <https://doi.org/10.1016/j.snb.2009.03.002>.
- [53] S. R. Kim, H. K. Hong, C. H. Kwon, D. H. Yun, K. Lee, Y. K. Sung, Ozone sensing properties of In_2O_3 -based semiconductor thick films, *Sens. Actuators B. Chem.* 66 (2000) 59–62. [https://doi.org/10.1016/S0925-4005\(99\)00468-2](https://doi.org/10.1016/S0925-4005(99)00468-2).
- [54] Y. D. Zhang, Z. Zheng, F.L. Yang, Highly sensitive and selective alcohol sensors based on Ag-doped In_2O_3 coating, *Ind. Eng. Chem. Res.* 49 (2010) 3539–3543. <https://doi.org/10.1021/ie100197b>.

- [55] G. Neri, A. Bonavita, G. Micali, G. Rizzo, N. Pinna, M. Niederberger, In₂O₃ and Pt-In₂O₃ nano-powders for low temperature oxygen sensors, *Sens. Actuators B. Chem.* 127 (2007) 455–462. <https://doi.org/10.1016/j.snb.2007.04.046>.
- [56] S. K. Vishwanath, T. An, W. Jin, J. Kang and J. Kim, The optoelectronic properties of tungsten-doped indium oxide thin films prepared by polymer-assisted solution processing for use in organic solar cells, *J. Mater. Chem. C* 5 (2017) 10295–10301. <https://doi.org/10.1039/C7TC03662K>.
- [57] G. Korotcenkov, V. Brinzari, A. Cerneavski, The influence of film structure on In₂O₃ gas response, *Thin Solid Films*. 460 (2004) 315–323. <https://doi.org/10.1016/j.tsf.2004.02.018>.
- [58] N. Yamazoe, Toward innovations of gas sensor technology, *Sens. Actuators B. Chem.* 108 (2005) 2–14. <https://doi.org/10.1016/j.snb.2004.12.075>.
- [59] G. Korotcenkov, The role of morphology and crystallographic structure of metal oxides in response of conductometric-type gas sensors, *Mater. Sci. Eng. R*. 61 (2008) 1–39. <https://doi.org/10.1016/j.mser.2008.02.001>.
- [60] J. F. Mc Aleer, P. T. Moseley, J. O. Norris, and D. E. Williams, Tin dioxide gas sensors. Part 1.—Aspects of the surface chemistry revealed by electrical conductance variations, *J. Chem. Soc. Faraday Trans. I* 83 (1987) 1323–1346. <https://doi.org/10.1039/F19878301323>.